Investigation of Rare-earth Elements Doped in Terbium Aluminum Garnet And Zinc Oxide for white light sources

Thesis Submitted to

LOVELY PROFESSIONAL UNIVERSITY

For the award of

DOCTOR OF PHILOSOPHY

IN

(Physics)

By
Suman Rani
Regd. No. 41100108

Supervised By
Dr. Bansi Lal

Co-Supervised by
Dr. Sumit Saxena

Lovely Faculty of Technology and Sciences
LOVELY PROFESSIONAL UNIVERSITY
PUNJAB
2017

Abstract

The development of the energy efficient white light sources used for artificial illumination is an active research field as almost 20% of the total energy produced world-over is consumed to fulfill the illumination needs of both the domestic as well as industrial consumers. The development of LEDs recently has been a big milestone because of their inherent high efficiency; theoretically, the energy efficiency of an LED can be >99% making it an ideal white light source. However, LED illumination inherently has poor color rendering properties; the true colors of the illuminated object are not reproduced faithfully. This color rendering property of a white light source is denoted by a dimensionless number called color rendering index (CRI). The CRI of sunlight at noon is assigned CRI=100 as its spectrum matches reasonably well with that of the response of the normal human eye. CRI of a filament lamp is about 98 while for LEDit is inherently low because the CRI is a function of spectral power distribution (SPD) of the output emission in visible region which is poor for LED's as these sources emit in relatively narrow regions. Also, best efficiency of LEDs is in blue region so the white light from it is blue-rich which may not be acceptable for long exposure illumination applications. Hence, there is a need for further development in this field. This thesis presents an attempt in this direction where results of an investigation about visible emission properties of rare-earth doped terbium aluminum garnet (TAG) and zinc oxide (ZnO) are presented.

TAG co-doped with Ce (cerium) and Eu (europium) was synthesized by sol-gel technique. The dopant concentrations investigated were 0.1, 0.5 and 1.0 mol%; nine samples were prepared by permuting the concentration level. The powder samples, thus, prepared were sintered in air at various temperatures (1100^{o}C maximum) using a home built temperature controlled (±1^{o}C) muffle furnace. On the other hand, ZnO single doped with Gd (gadolinium), Tb (terbium), Ce and Eu, co-doped(double doped) with Ce and Eu and triple doped with Ce, Eu and Tb were prepared by precipitation technique. The precipitation thus obtained was sintered in air at various temperatures (700^{o}C maximum)

All the sintered powder samples were characterized by (i) energy dispersive x-ray spectroscopy (EDX) to confirm the incorporation of dopants in the host, (ii) scanning electron microscope (SEM) / transmission electron microscope (TEM) to investigate the nanostructure nature of the samples, (iii) Fourier transform infrared spectroscopy (FTIR) and X-ray diffraction (XRD) to assess the changes, if any, in the host structure on doping, (iv)UV-VIS absorption spectroscopy

to measure the absorption levels in UV-VIS region, (v) Raman spectroscopy to measure the lattice distortion, if any, induced in the host by the dopants and (vi) photoluminescence studies to check the suitability of the prepared materials for the realization of white light sources. The visible emission was also analyzed using Commission Internationale de leclairage 1931(CIE) color space diagrams to assess its potential for the preparation of white light sources.

EDX confirmed the incorporation of Ce and Eu in TAG, that of (single) Gd, Tb, Ce and Eu in ZnO, co-doping (double) of Ce and Eu in ZnO along with the co-doping (triple) Ce, Eu and Tb in it.

SEM/TEM images confirmed the nanostructure of the doped samples both in case of TAG as well as in ZnO. Also it was observed that all the powders were mostly composed of spherical particles.

FTIR and XRD confirmed no change in the basic crystal structure of the host material (TAG and ZnO) on doping. All the powder XRD spectra of doped TAG could be indexed with JCPDS 17-035 which is the primary file for the crystal structure of TAG. Similarly, all doped samples of ZnO were indexed with the primary file No. JCPDC file No. 36-1451. However, the observed shift in the peak positions of the diffraction peaks, change in lattice constant and unit cell volume showed the distortion induced in lattice by doping. The diffraction peak with (hkl) (420) shifted by~ 0.22^{o} (towards the lower angle) whien TAG was co-doped by 0.5mol% of Ce and Eu. Similarly, the diffraction peak (101) by ~0.09^{o} (towards the higher angle) in case of ZnO doped with 0.5mol% Tb. However, this shift was both concentration as well as dopant nature dependent. This induced distortion was also reflected in the crystallite size calcaulated from the XRD data using well known Scherrer formula.

The distortion induced by doping was also investigated by Raman spectroscopy. The 439 cm^{-1} Raman line split into two lines (433 and 445cm^{-1}) in case of ZnO doped with 0.5mol% Tb, Also, shifting of peak position of the Raman lines by as much as 8cm^{-1} was observed in some cases. However, this splitting/shifting was found to depend on concentration as well as on the nature of the dopant.

UV-VIS absorption was, as mentioned earlier, to quantify the absorption of the samples in UV and VIS regions of the electromagnetic spectrum. This was particularly useful in ZnO where change in the absorption edge on doping could be measured. The maximum change in the

absorption edge was found to be about 10nm in ZnO doped with Tb. Similar results were found in other doped samples of ZnO.

The photoluminescence (PL) spectra were recorded using 280, 300, 345, 380 and 465 nm radiation from a Xe lamp. The broadband emission in the visible region both in doped TAG as well as in doped ZnO were observed when excited with 280 and 300nm radiation. The intensity as well as the full width at half maximum (FWHM) of this broad emission showed dopant concentration dependence. To assess the suitability of the observed emission, as mentioned earlier, chromaticity color space diagrams were used to calculate the co-ordinates x and y which are the indicators of the usefulness of the emitting materials in realization of the white light sources; x=0.33 and y=0.33 are the ideal values for white light emitter. The calculated value of the visible emission excited in TAG co-doped with 0.5mol% of Ce and Eu were: x=0.35 and y=0.35 which are reasonably close to those of an ideal white light source. The values for 0.5mol% Gd doped in ZnO x=0.31,y=0.32 were observed. Similarly the values for the broad band emission in the visible region from the ZnO co-doped with 0.5mol% Ce, Eu and Tb were: x=0.32 and y=0.32. This thesis discusses several such materials which may be used for the fabrication of the white light sources.

.

CHAPTER 1

INTRODUCTION

1.1 Introduction

The ever increasing energy demand has necessitated a continuous research activity world over to develop energy efficient devices; one such intense research activity is the development of the energy efficient white light sources (emitting in 400-700nm region) used for artificial illumination as almost 20% of the electrical energy produced internationally is used for this application[1]. In addition to efficiency, a light source used for illumination should have good color rendering properties so as to reproduce the colors of the illuminated object faithfully. The parameter used to characterize the color rendering properties of a light source is called CRI (color rendering index); it is a dimensionless number [2]. Sunlight at noon being the best natural light source is the bench mark with assigned CRI=100. The best man-made light source with CRI~100 is filament lamp which utilizes electrical power to heat its filament for white light emission. However, its efficiency is inherently limited because it emits predominantly in IR (>700nm) region which is not useful for illumination application. On the other hand, the efficiency of a fluorescent lamp, another man-made light source, is limited by the conversion efficiency of the UV radiation into visible by the materials used presently. Also, CRI of a typical fluorescent lamp is ~ 40 which means poor color rendering properties. These limiting factors being fundamental in nature are almost insurmountable and it seems that the road to further increase in the efficiency of the incandescent and the fluorescent light sources has reached to a dead–end; new approach and concepts are needed. Recent advances in the material development and fabrication technologies of light emitting diodes (LED) have resulted in several LED based promising strategies to create white light with the use of inorganic/ organic materials. The efficiency of these “all solid state” light sources is not limited by any fundamental factors as is the case with conventional light sources. Also, various parameters like spectral, temporal, spatial and polarization features of the output can be well-controlled for these light sources. Two schemes used for producing white light sources are:

i. Multi-color LED: The out-puts from various LEDs emitting in different portions of the visible spectrum are combined properly to produce desired output: R-G-B being the most popular scheme where red, green and blue radiation from three different LED's is combined in proper proportion to produce the white light.
ii. LED based phosphor: In this case a blue LED is used to excite green and red phosphors such that unused portion of blue (from LED) combines with green and red emission (from phosphor) to produce the white light.

Scheme (i) looks more promising because of the tremendous advances in the fabrication technology of the LED's. However, this scheme has its limitations as tailoring of LED bandgaps is relatively more difficult compared to that of emission radiation from the phosphors materials used in scheme (ii).

For the purpose of the development of highly energy-efficient light sources, there is need to design highly efficient green, red and yellow phosphors, which are able to absorb excitation energy and generate emissions. The energy could be transferred from one luminescent activator to the other one using double/triple activation, resulting in more efficient device operation. Also, this co-activator scheme could be used to change the spectral energy distribution (SPD) of the emitted light for better CRI.

Rare-earths [3] are interesting materials as their 4f outer shell electrons, to a great extent, are shielded by the core electrons so that when doped in a crystal, the observed spectroscopic properties are almost the same as those of the free-ions. These ions when doped in a crystalline host do emit in various regions of the visible spectrum making these materials potential candidates for the white light sources. These rare-earths dopants enter the lattice sites mostly as trivalent ions (Re^{3+}) with emission that is almost independent of the host material. However, interesting energy transfers in certain hosts on doping with the rare-earths make those hosts very interesting.

A host should be physically and chemically stable compound with no inherent absorption at the absorption wavelengths of the rare-earth element doped in it. Also, it should provide non-centro symmetric environment at the rare-earth ion site so that the parity forbidden transitions in Re^{3+}-ions are allowed. In this work, terbium aluminum garnet and

zinc oxide are the two hosts which were investigated for the development of the white light source on doping/co-doping with, Ce, Eu, Tb and Gd elements.

1.2 Terbium aluminum garnet (TAG)

The general chemical formula for a typical garnet is $X_3Y_5O_{12}$. It cryatalizes in dodecahedral shape with cubic symmetry where all the three axis (equal in length) are perpendicular to each other. Among various garnets, YAG (ytterbium aluminum garnet, $Y_3Al_5O_{12}$), TGG (terbium gallnium garnet, $Tb_3Ga_5O_{12}$), GGG (gadolinium gallium garnet, $Gd_3Ga_5O_{12}$) and TAG (terbium aluminum garnet, $Tb_3Al_5O_{12}$) are being investigated recently for their applications in the realization of photonic devices [4]. Nd :YAG is well known CW laser material while Ce: YAG is presently used for the commercial fabrication of white light emitting LEDs [5]. On the other hand, TGG and GGG are used for the fabrication of Faraday rotators and optical isolators [6]. The suitability of any material for Faraday rotator is indicated by the magnitude of its wavelength dependent Verdet constant. Its value for TGG is equal to -134 rad/Tm (room temperature, 632 nm) while for TAG [7] its value is ~180rad/Tm (room temperature, 632nm) which makes this material superior to TGG; also TAG has broad transmission ranging from 350 to 1500 nm. However, because of the inherent incongruent melting of TAG [8], intense activitives of growing its crystals of any significatnt size have not yielded any result till date and researchers are concentrating on its applications in powder form. Conventionally, TAG was prepared by high temperature solid state reaction; its nanostructured powders can be prepared by low temperature sol gel technique [6] followed by sintering; the crystalline phase starts developing around 900^{o}C while ~1100^{o}C, the material is almost completely crystalline. Sintering in air results in translucent powder while vacuum sintering can yield transparent powder samples. Rare-earth elements when single doped in TAG are known to have characteristic emission of the dopant [9] while co-doping with two or rare-earth elements are expected to have broad emission in visible emission because of the characteristic energy exchange between the bvarious rare-earth dopants [10]

1.3 Zinc oxide (ZnO)

ZnO has been investigated because it (i) is cheap and easily available, (ii) has high chemical stability, (iii) shows a broad absorption range and (iv) has tunable band gap [8, 9 & 10].It is an n-type semiconductor with a wide band gap of ~3.36 eV. ZnO nano-particles with band gap tunability, large oscillator strength, and low production cost, are promising wide band gap semi-conducting materials for much needed ultra violet (UV) and optoelectronic devices such as white light emitting diodes (LEDs) and laser diodes [11,12 & 13]. As a blue emitter, it is a potential material for white light LED when doped with fluorescent materials like rare earths in proper proportion.

1.3.1 Physical properties of ZnO

The physical properties of the hexagonal wurtzite structured ZnO are listed in the Table.

Table1.1: Main properties of the Wurtzite ZnO structure

Properties	Values	References
Lattice constant	a=0.32495 nm & c=0.52069 nm u=0.3817–0.3856 & c/a=1.593–1.6035	[14,15 &16]
Density(kg/m^3)	5.605 x 10^3	[15]
Melting point(^{o}C)	1975	[15]
Relative dielectric constant	8.5	[15]
Energy band gap(eV)	3.36	[14,11 &17]
Exciton binding energy(meV)	60	[10,11 & 19]
Electron mobility(m^2/V.s)	2 x 10^{-2}	[15]
Electronic effective mass(m/m$_o$)	0.24	[15]
Hole effective mass((m/m$_o$)	0.59	[15]
Hole mobility (m^2/V.s)	5x10^{-4}	[15]
Type of band gap	Direct	[14 & 20]
Refractive index	2.00	[15]
Molecular mass(kg/mol)	81.379 x 10^{-3}	[15]

1.3.2 Crystal structure of ZnO

ZnO crytalizes exist in three crystalline phases namely (a) hexagonal Wurtzite and (b) zinc blend and (c) cubic rock salt as shown in the Fig 1.1. Among these three phases the most common phase observed usually is the hexagonal wurtzite [8] .The space group associated with this phase is $P6_3mc$; two interconnecting sub lattices of $Zn^{+2}$and O^{-2} constitute its lattice such that each O ion is surrounded by a tetrahedral of Zn ions, and vice-versa.

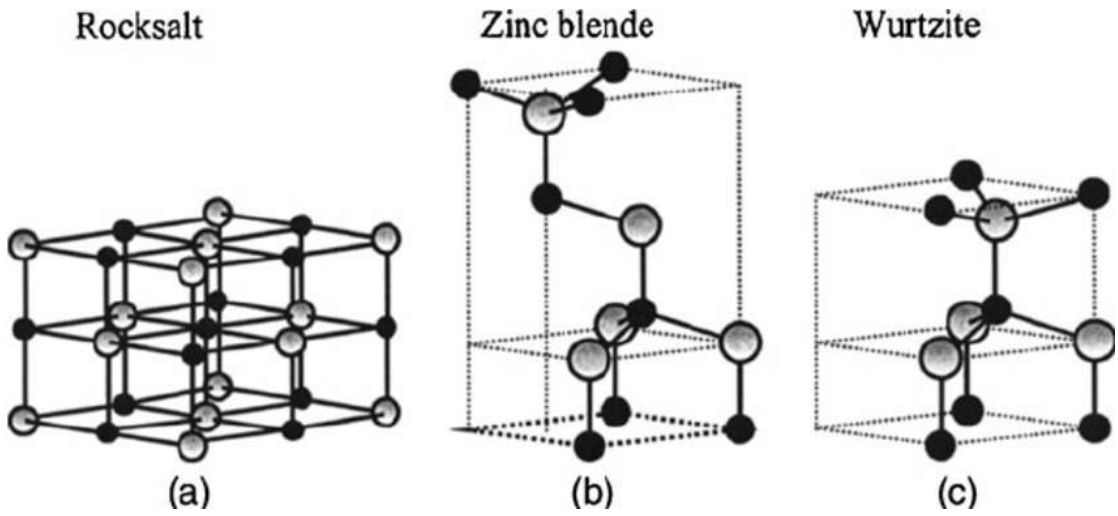

Fig. 1.1: ZnO crystal structures: cubic rock salt (a), cubic zinc blende (b) and hexagonal wurtzite (c). The shaded gray and black spheres represent zinc and oxygen atoms. [20]

The crystal structure is investigated by XRD (x-ray diffraction) which is based on well-known Bragg's law presented in Eq 1.1

$$n\lambda=2d\sin\theta \qquad (1.1)$$

Where n is the order of the diffraction (usually n = 1), λ is the wavelength of the X-ray radiation and d is the spacing between the planes of given Miller indices h, k and l. In the ZnO hexagonal structure, the plane spacing 'd' is related to the lattice constants, 'c' and the Miller indices (hkl) by the following relation Eq 1.2 [21].

$$\frac{1}{d^2}=\frac{4}{3}\left(\frac{h^2+hk+k^2}{a^2}\right)+\frac{l^2}{c^2} \qquad (1.2)$$

For n=1 the Eq 1.2 can be expressed as Eq 1.3 under small angle approximation.

$$sin^2\theta = \frac{\lambda}{4a^2}^2 \left[\frac{4}{3}(h^2 + k^2 + hk) + \left(\frac{a}{c}\right)^2 l^2\right] \quad (1.3)$$

For (100) plane Eq 1.3 reduces to:

$$a = \frac{\lambda}{\sqrt{3}sin\theta} \quad (1.4)$$

Similarly for plane (200) Eq 1.3 reduces to:

$$c = \frac{\lambda}{sin\theta} \quad (1.5)$$

Eq 1.5 can be used to estimate the lattice constant "c"

The Zn-O bond length can be caluated from Eq 1.6 [21]

$$L = \sqrt{\left(\frac{a^2}{3} + \left(\frac{1}{2} - u\right)^2 c^2\right)} \quad (1.6)$$

Where u called the positional parameter in wurtzite structure, measures the amount of displacement of each atom along c-axis.

$$u = \frac{a^2}{3c^2} + 0.25 \quad (1.7)$$

The average crystallite size 'S' can be calculated using Scherrer Eq 1.8 [22]

$$S = \frac{K\lambda}{\beta cos\,\theta} \quad (1.8)$$

Where 'λ' is wavelength diffracted from the atom within target material located at an angle 2θ and β is the peak width at half maxima of the diffraction peak; *K* is a constant related to crystallite shape, normally taken as 0.94.

1.3.3 Electronic Band of ZnO

A typical semicondutor has populated states called “valence bands” and unpopulated states termed as “conduction bands”; the energy differeence between valence bands and conduction bands is defined as “band gap” which is an important property of a semiconductor; lowest energy point in the valence band is called band edge. As shown in Fig 1.2, there are two types of “band gaps’ namely “direct band gap” and “indirect band gap’; in case of direct band gap, the minimum energy point in the conduction band has same “k value’ (crystal momentum) as that of the maximum energy point in the valence band while this is not case for indirect band gap semiconductor as explained in Fig 1.2

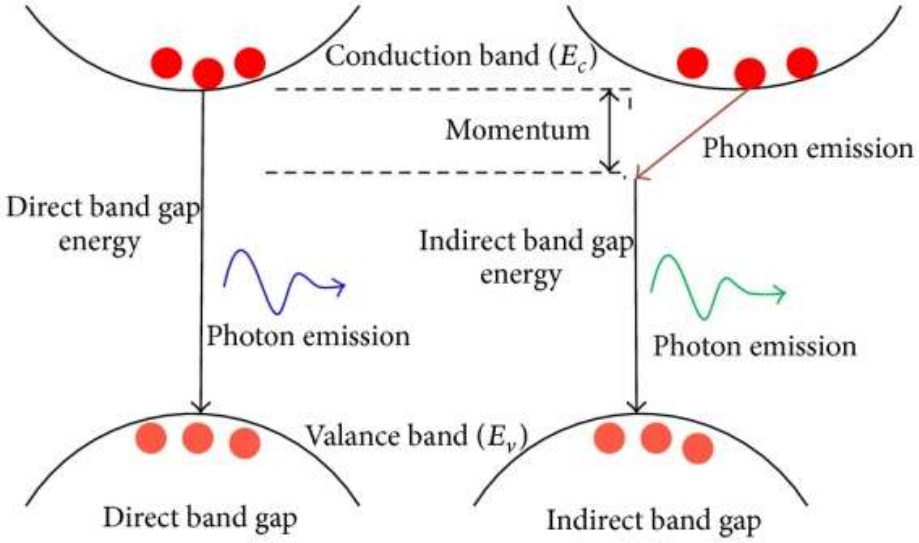

Fig.1.2: Direct and Indirect band gap in semiconductor [22]

Excitation/de-excitation process in a direct band gap are a “single step “process while it is “a two-step process” involving phonons in case of indirect band gap semiconductors. Spectroscopic techniques are used to determine the band gap experimentally; it is straight forward for a direct band gap semiconductor while in indirect band gap semiconductor, one has to perform additional experiments like temperature variation to estimate the band gap.

ZnO is a direct band gap semiconductor with energy band gap of about 3.4 eV [14,18 & 20]. It is an n-type semiconductor where excess zinc is always present due to its wurtzite crystal structure making it a non-stoichiometric compound; interstitials Zn_i and the oxygen vacancy V_o are known contributors to the lattice defects found in undoped ZnO.

1.3.4 Optical properties of ZnO

The mechanism responsible for optical properties of a typical semiconductor is attributed to both intrinsic and extrinsic effects. Transitions associated with the emission of photons do occur between the electrons in the conduction band and holes in the valence band. These transitions include the exciton effects arising due to the Coulomb interaction; the group velocity of the electron should be equal to that of the hole. Any particular, exciton could be "free" or "bound" depending on the nature of the interaction responsible for its formation. In certain cases like high quality samples with low impurity concentrations, the free exciton can also have excited states. On the other hand, the extrinsic effects which are due to the defects induced by the dopants and/or structural imperfections result in the formation of discrete electronic states in the band gap. These discrete states significantly change the optical absorption and emission processes.

A number of experimental techniques such as absorption, transmission, reflection, photoluminescence, cathode-luminescence etc are employed to investigate the optical transitions in ZnO. [19& 22]. Photoluminescence (PL) spectra at room temperature usually contains a near UV-emission band around 375 nm, a green emission band around 510 nm and a yellow-orange band around 610 nm.. The near UV-band is a measure of excitonic nature of material [19 & 25]. The observation of luminescence from exciton is usually difficult even at low temperatures while a large part of the radiative emission comes from bound-exciton complexes and defect centers.

There is no consensus about the exact mechanism of the origin of defect-related visible emissions despite hectic research activities world-over. Several mechanism, as pictured in Fig 1.3, have been suggested.

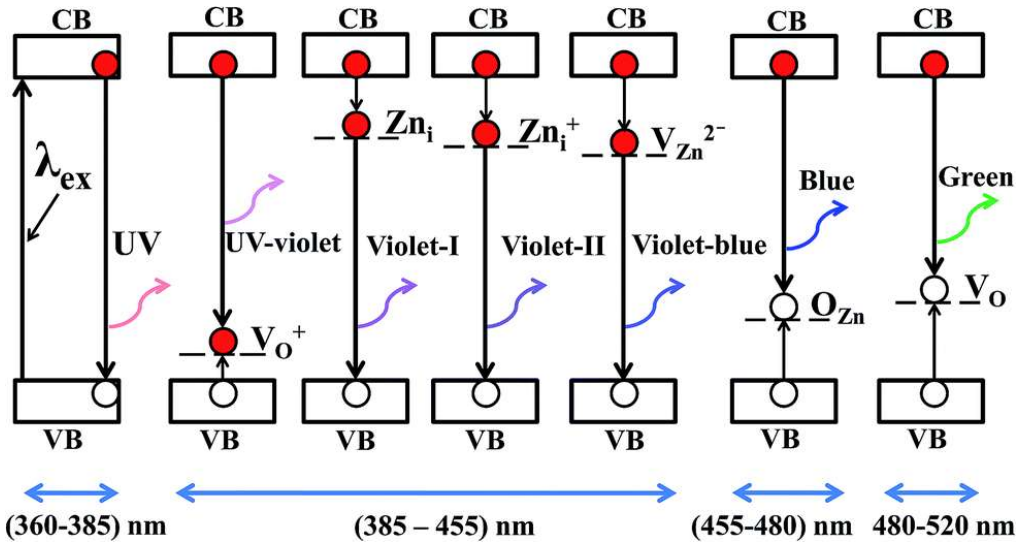

Fig.1.3: The origins of different visible photoluminescence components classified in the UV-violet, violet, violet-blue, blue and green regions.[23]

As seen in Fig 1.3, the absorption and emission in UV region are due to the transitions between the conduction bands(CB) and the valence bands (VB) while the emission in the region 385-455nm involves the energy levels due to interstitial defects induced by Zn_i and V_o . On the other hand, the emission in 455-480nm region is due to transition between the CB and Zn_i while transition from CB to the levels due to V_o are responsible for so called green emission observed in 480-520nm region.

This picture is only indicative in nature because the exact reproducibility of the defect levels is not possible resulting in the variations in observed emission.

1.4 Rare-earth dopants

In the present investigation, as mentioned earlier, rare-earths like Gd, Ce, Eu and Tb were single/double/triple doped/co-doped in TAG and ZnO nano phosphors. The rare-earths are known to enter any lattice normally as (+3) state, energy level diagram of these free ions are shown in Fig 1.4; energy level diagram of ZnO has been shown for comparison in this fig.1.4 [27]. As seen in this figure, the energy levels of dopants coincide with conduction band of ZnO implying the possibility of energy transfer between the ZnO and the dopants. Investigation of double and triple co-doping is more interesting both from the fundamental as well as from application angles.

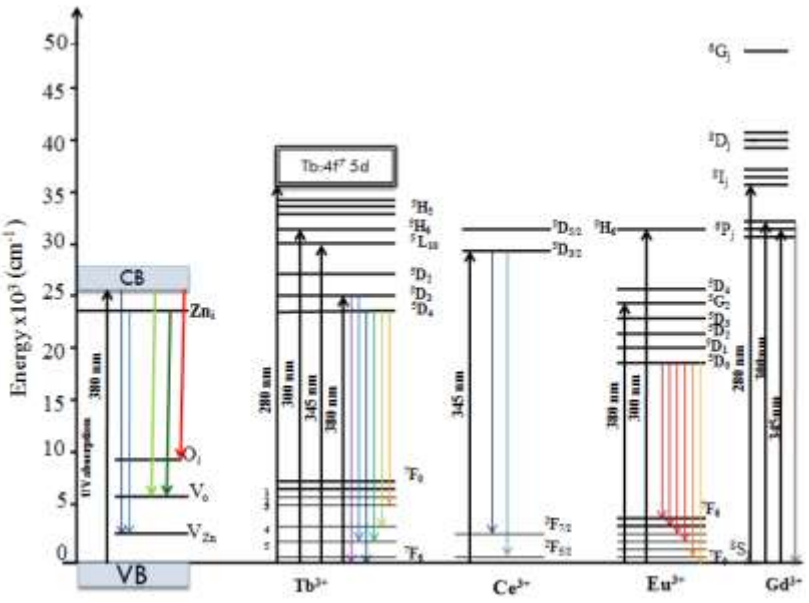

Fig. 1.4: Energy level diagram of ZnO with defect states, Tb, Ce and Eu and Gd (3+) ions [27]

1.5 Color space Conversion

Since a healthy human eye is fitted with three types of "cone cells" [28] to detect the color of light scattered by an illuminated object; the three cones are sensitive to red, green and blue colors. This tri-chromatic theory of color is based on the basic principal that any 'hue" in visible region (400-700nm) can be produced by mixing red, green and blue colors in proper proportion. Hence, three parameters corresponding to the stimulus levels of the three cones of a human eye are used to characterize the color perceived by it when receiving the scattered light from an illuminated object. *Commission Internationale de l'Eclairage* (International Commission on Illumination) has standardized these parameters [X, Y and Z] in 1931in terms of the color space diagrams which characterize the emission from a light source. A color space diagram links the emission wavelength with color perceived a normal human eye. In this technique, the spectral power distribution (Fig 1.5) is used to calculate the values of X,Y and Z [28] using equations 1.9,1.10 and 1.11. The calculated values of X,Y and Z thus obtained are used to calculate the chromaticity color coordinates x,y and z using equations 1.12 to 1.15. Typical color space diagram where the chromaticity coordinates are mapped to the "color" on a two-

dimensions is shown in Fig 1.6 [29]. The values of the coordinates x and y should be 0.33 for an ideal white light source [28 & 29].

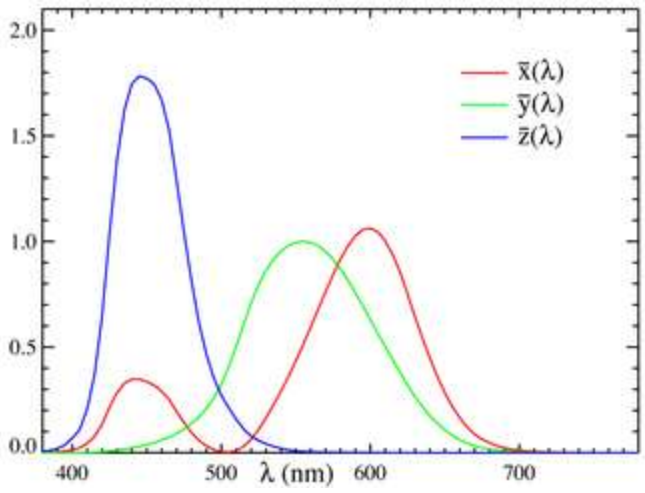

Fig.1.5: The CIE standard observer color matching functions [30]

$$X = \int_0^\infty I\,(\lambda)\overline{X}(\lambda)d\lambda \quad (1.9)$$

$$Y = \int_0^\infty I\,(\lambda)\bar{Y}\lambda)d\lambda \quad (1.10)$$

$$Z = \int_0^\infty I\,(\lambda)\overline{Z}(\lambda)d\lambda \quad (1.11)$$

$$x = \frac{X}{X+Y+Z} \quad (1.12)$$

$$y = \frac{Y}{X+Y+Z} \quad (1.13)$$

$$z = \frac{Z}{X+Y+Z} \quad (1.14)$$

$$x+y+z=1 \quad (1.15)$$

In Equations 1.12, 1.13 and 1.14 I (λ) is the spectral power distribution of light source.

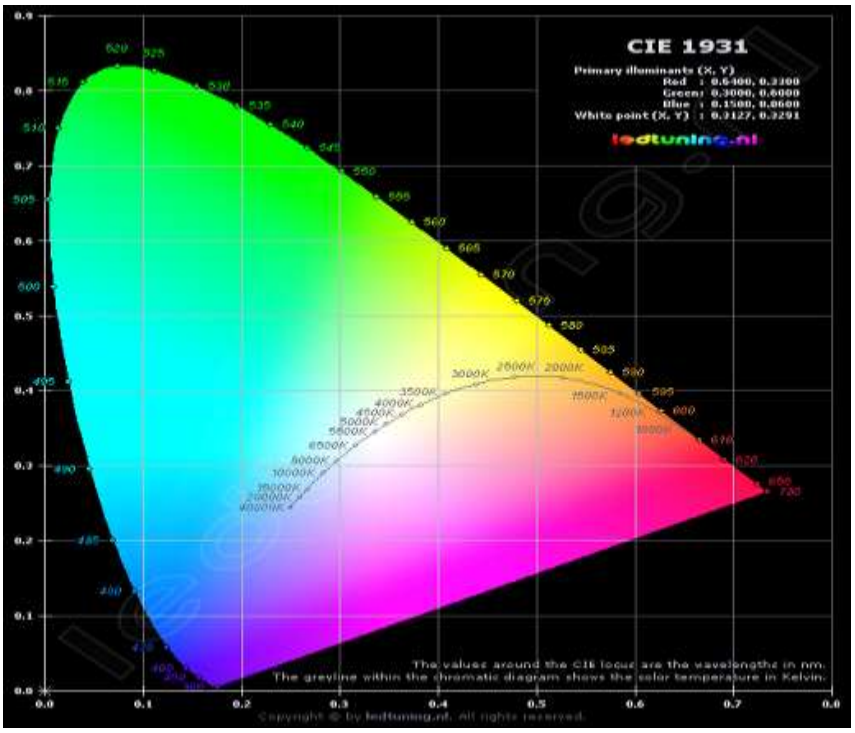

Fig.1.6 Typical CIE 1931 color space [30]

1.6 Color correlated temperature

White color is termed “cool” if it contained dominant blue component or “warm” in case the dominant component is yellow. This aspect of a white light source is characterized by “correlated color temperature (CCT) which relates the appearance of a light source to the appearance of a theoretical black body heated to high temperatures as shown in Fig1.6 [32]. As a black body gets hotter, it turns red, orange, yellow, white, and finally blue. The CCT of a light source, given in Kelvin (K), is the temperature at which the heated black body most closely matches the color of the light source in question. It characterizes the color of the emitted light, not the color of illuminated objects [33].For the CCT calculation following equation is used [32 & 34]

$$CCT(x, y) = -449n^3 + 3525n^2 - 6823.3n + 5520.33 \qquad (1.16)$$

Where n = (x - xe)/(y - ye) is the inverse slope line, and (xe = 0.3320, ye = 0.1858) is the “epicenter"; quite close to the intersection point mentioned by Kelly [32].

REFERENCES

[1] E F Schubert and J K Kim (2007) *Energy-efficient control of solid-state lighting 308*: 1274-1278.

[2] Burgt P V and Kemenade J (2010) *COLOR research and application 35*:85-93

[3] Ronda C R, Justel T and Nikol H (1998) *J. Alloys Compound* 275:669-676

[4] White W B and Keramids V G (1972) *Spectrochim. Acta Part A.* 28:501-509.

[5] Geller S (1967) Z*eitschrift fur Kristallographie Bd .Bd* 125: 1-47.

[6] Shabir H , Lal B and Rafat M (2009) *Int. Journal of Nano and Biomaterials* 2:416-424.

[7] Das J, Das K and Parida K M (2005) *Moldavian journal of physical Sciences* 4:347-356.

[8] Shin et al. (2004) *Journal of the Korean Physical So- ciety* 45: 1288-1291.

[9] Zhao et al. (2005) *Journal of Crystal Growth* 276:507-512. doi:10. 1016/j.jcrysgro.2004.11.407

[10] Pearton et al (2005) *Progress in Material sciene* 50:293-340

[11] Xu et al. (2000) *Actuat.B-Chem* 66: 277-9.

[12] Majumder S B et al. (2003) *Mat. Sci. Eng. B* 103: 16-25.

[13] Byeong K C et al. (2006) *J. Mater. Sci.: Mater. Electron.* 17: 1011-5.

[14] Mateika D, Volkel E and Hisma J. (1990) *J. crystal Growth* 102: 994-1013

[15] Norton et al. (2004) *Materials Today* 7: 34-40. doi:10.1016/S1369-7021(04) 00287-1

[16] Kim N H and Kim H W (2004) *Materials Letters* 58: 938-943. doi :10.1016/ j.matlet.2003.07.040

[17] Mang A, Reimann K and Rubenacke S (1995) *Solid State Communications* 94: 251-254 doi :10.1016/0038-1098(95)00054-2

[18] Bao D, Gu H and Kuang A (1998) *Thin Solid Films* 312: 37-39.

[19] Mohammad M T, Hashim A A and Maamory M H (2006) *Mater. Chem. Phys.* 99: 382-387.

[20] Espitia et al.(2012) Food Bioprocess Technol 5:1447–1464

[21] Bindu P and Thomas S (2014) *J TheorAppl Phys* 8:123–134 doi:10.1007/s40094-014-141-149

[22] Singh et al(2015) *Journal of material* 2015:1-6 http://dx.doi.org/ 10.1155/ 2015/840 718)

[23] Das D and Mondal P (2014), *RSC Adv.* 4: 35735–35743.

[24] Zemen S T and Emre Gu r, (2007) *Optical Materials* 30:292–310.

[25] Lin Y et al. (1999) *Adv. Mater.Opt. Electron* 9:20

[26] Kong et al. (2001) *Appl. Phys. Lett.* 78:407-409.

[27] Liu et al. (2015) *Dalton Trans.*44: 6645.doi: 10.1039/C5DT00581G

[28] http://www.techmind.org/colour

[29] Gsiea et al. (2014) *Physical, Electrical and Computer Engineering* 81.

[30] https://www.ledtuning.nl/en/cie-convertor

[31] Kelly and Kenneth L (1963), *JOSA.* 53: 999–1002. doi:10.1364/JOSA.53.00 0999.

[32] Andres H, Lee J and Romero R L (1999) *Applied Optics.*38: 5703–5709. doi :10.1364/AO.38.005703.

[33] McCamy and Calvin S (1992) *Color Research & Application* 17:142–144. doi:10.1002/col.5080170211.plus erratum doi:10.1002/col.5080180222

CHAPTER 2

REVIEW OF THE LITERATURE

2.1 Introduction

The aim of this thesis, as mentioned earlier, was to investigate the suitability of the rare-earth doped TAG (terbium aluminum garnet) and ZnO (zinc oxide) nano-powders for the realization of the white light sources and light sources which could be energy efficient with high color rendering properties. The relevant literature in the chosen research field is reviewed in the following sections.

2.2 Terbium aluminum garnet

Boyer et al. (2004) prepared the Yb doped $Ga_3Ga_5O_{12}$: Ho^{+3} nano material in which up conversion luminescence phenomena was observed. Emission spectra consist of strong emission from near infra red to green luminescence when material was excited with 978 nm .Strong blue red and near infra red emission were observed when material was excited with the wavelength greater than 978nm**.**

Mazur et al. (2005) prepared terbium-doped yttrium aluminum garnet nano-material. Decomposition of precursor and formation of nano material were studied by using Thermo-gravimetric and differential thermal analysis techniques. It was found that with the increase of annealing temperature, crystallite size also increased from 20 to 40 nm which was further confirmed by XRD technique. It was also concluded that there was no effect of annealing temperature and crystalline size on the intensity and the decay times of both $^5D_3$ and $^5D_4$ emission from the material.

Potdevin et al. (2005) synthesized YAG: $Eu^{3+}$and YAG: Tb^{3+} luminescent films by using spray and dip coating techniques and nano-particles were prepared by sol gel technique. At 900^{o}C, polycrystalline yttrium aluminum garnet powder was obtained. Luminescence decay of Tb^{3+} and Eu^{3+} ions were recorded using laser and it was concluded that decay times varied as exponential, as shorter than 5 ms for both Eu^{3+} and Tb^{3+} activators.

Nazarov et al. (2006) prepared Ce doped YAG (YAG: Ce), Tb doped TAG (TAG: Ce), Eu, Ce co-doped YAG and TAG powders using solid state reaction. YAG: Ce and TAG: Ce and Ce, Eu co-doped YAG showed luminescence mainly from Ce ion due to d–f transitions whereas luminescence from TAG co-doped with Ce and Eu was from both Ce and Eu. It was concluded that the Ce can be used as a sensitizer in the TAG lattice that transferred its energy by the Tb sub lattice to the activator Eu.

Jung et al. (2006) prepared Tb doped YAG and Ce, Tb co-doped YAG using spray pyrolysis Ce and Tb co-doped in YAG showed luminescence due to the d–f transition of Ce ions. It was found that effective energy transfer occurred from Tb to Ce in YAG lattice.

Chiang et al. (2007) synthesized a stable GAG pure-phase powder by substituting small cations (Tb^{3+}, Y^{3+} or Lu^{3+}) at the dodecahedral sites or the substituting the large cation (Ga^{3+}) for the Al^{3+} sites of the garnet structure. Pure garnet-phase GAG powder was formed by sintering at 1500°C for 2 h. It was found that increasing of the Lu^{3+} content in the Gd^{3+} lattice site of the dodecahedral or increasing of the Ga^{3+} content in the Al^{3+} site induced a blue shift in the emission wavelength. The color temperature of the pure GAG: Ce (YAG:Ce) phosphor powder (2900 K) formed was lower than that of yttrium aluminum garnet and terbium aluminum garnet (TAG: Ce) phosphors.

Liu et al. (2007) **s**ynthesized pure TAG powder by a modified solid-state reaction method. Particle size of terbium oxide was reduced by decreasing the value of the pH . Adjusting the mixed slurry at pH , the morphology of Tb_4O_7 can be changed to form an agglomerate of small particles. TAG: Ce phosphor powder with higher luminescence property was obtained when the mixing slurry was adjusted to pH 1. Thus produced TAG powder showed a maximum emission peak at 553 nm when excited at 470 nm.

Nazarov et al. (2007) studied the emission properties of doubly activated TAG with Ce and Eu. In the lattice energy transfer process took place from Ce to Tb lattice to Eu. It was concluded that by proper choosing the concentration of Eu and Ce in TAG, CRI of the material can be improved and material can be used to fabricate the light emitting devices.

Vasil et al. (2007) prepared the single phase film of Tb doped gadolinium gallium garnet, in which two absorption bands were absorbed at 260nm and 280nm.Intnesity of band at 260nm increased and 280nm decreased with the increase of Tb component in garnet. A broad and intense emission peak is observed at 544nm in emission spectra.

Zorenko et al. (2007) studied the existence of characteristic bands 4f and 4f–5d of Tb ions corresponding to the $^7F_j \rightarrow {}^7E$ and $^7F_j \rightarrow {}^7E$ transitions in the excitation spectrum of Ce and existence of components with the lifetimes 0.56-0.6 μs and 3.5-4.9 μs in the luminescence decay of Ce ions. Based upon these studies, it was concluded that there was effective energy transfer from Tb ions to Ce in single crystalline films (SCF) of Ce doped TAG.

Fadlalla et al. (2008) prepared undoped and Ce doped Yttrium aluminum garnet(Ce: YAG) by sol gel method. Crystalline phase of prepared material were developed at 1000^0 C. Average grain size of Ce doped YAG(20 to 23 nm) was smaller than that of undoped YAG(28 to 34nm).PL spectra show the peak in the range of 480 to 535 nm and near to 520 nm. 5d-4f transition of Ce increased with the increased of the annealing temperature .Also with the increase of Ce concentration peak shift towards the red region.

Zorenko et al. (2008) prepared the single crystal films of Ce, Eu co-doped TbAG luminescent material for LED and studied the process of energy transfer from Tb to Ce and Eu ions. It was concluded that this energy transfer took place due to dipole–dipole interaction between Ce and Eu ions and through the sub lattice of Tb.

Mhin et al. (2009) synthesized cerium-doped terbium aluminum garnet (TAG: Ce) nano-material by pulsed laser ablation (PLA) using de-ionized water and lauryl dimethylaminoacetic acid betain (LDA) aqueous solution for luminescent bio-labeling application. It was found that crystallite size was reduced. There was a narrower size distribution and emission properties were improved when TAG doped Ce by using LDA. TAG: Ce showed the blue-shifted in its emission spectra. They studied the 5d energy level of Ce with respect to the decreased in crystal size and built the relationship between bond distances with 5d energy level of Ce.

Psuja et al. (2009) fabricated the Tb doped YAG transparent, conductive and green light emitting luminescent layer using the modified Pechini method. It was found that with the increase of number of coating, there was a decrease in optical transmission and resistivity of the layer .

Shabir et al. (2009) synthesized the terbium aluminum garnet phosphor using sol-gel technique and the sintering in the temperature range from 800 to 1600°C. The grain size was found to be in the range of 50 to 60 nm. It was found that better phase was developed at higher sintering temperature. A Photo-luminescence spectrum consists of six peaks 440, 490, 549.9, 586.9, 624 and 691 nm. The emission intensity of the peak at 691 nm increased with the increase in sintering temperature from 1000 to 1400°C whereas the intensity decreased in rest of the cases in the same temperature range.

Shabir et al. (2010) prepared Eu (0.1, 0.5 and 1.0 mol%) doped TAG using sol–gel technique, and sintered in air at 1100^{o}. XRD analysis showed that Eu ions entered in the TAG lattice and replaced the Tb ion. It was concluded that there was better crystalline phase development at higher of sintering temperature. It was clear from the SEM and TEM images that prepared particle morphology was spherical and size was in the range of 5 to 20 nm. The PL spectra of Eu doped TAG excited with 380nm had strong red emission. Emission intensity increased with the increase in Eu dopent concentration from 0.1 to 0.5 mol% and suppressed with further increase in Eu concentration in TAG. This intensity variation with dopants concentration were due to ‘‘concentration quenching’’. The same material when excited with blue light (480nm) using Xe lamp, high intensity red emission due to Eu was observed and concluded that prepared material could be realized of white light LED.

Shabir et al. (2010) compared the structural and optical properties of TAG powder sintered at 1100^{o} C in air using furnace and in vacuum with continuous wave pulsed CO_2 laser . Structural properties of TAG were remain same when prepared material were sintered in air(furnace) and in vacuum using laser except that the pure TAG .The absorption and emission intensity of TAG sample sintered in air and sintered in vacuum using laser were compared and found higher absorption and emission intensity when sample sintered in vacuum using laser.

Zorenko et al. (2010) synthesized the single crystal films (SCF) of undoped TbAG, Mn doped TbAG and Mn, and Ce co-doped TbAG using liquid-phase epitaxy (LPE) method. The effective energy transfer was observed from TAG lattice to Mn ion from the d–f and f–f states of Tb^{3+} ions via the radiative transition $^5D_3$ and $^5D_4$ levels in UV (375nm) and visible (487 nm) ranges. Also, broad emission was obtained around 595 nm with life time of 0.64ms. In co-doped TAG with Mn and Ce(TAG: Mn: Ce), the simultaneous energy transfer from Tb to Ce ions and Mn ions was realized. TAG: Mn, Ce phosphor luminescence was compared with YAG :Ce and TAG: Ce phosphors and relatively higher luminescence in the orange-red spectral range was observed when TAG co-doped with Mn and Ce and this was due to the existence of the Mn emission,.

Shaat et al.(2012) prepared the Eu and Tb doped $Ca_xSr_{1-x}Al_2O_4$ by combustion method. The prepared material was excited by 227 nm and showed the broad visible emission in which green and blue lines were due to Tb and red lines were due to Eu.CIE coordinates were calculated (x=0.343,y=0.325) which were close to ideal white light coordinates. Therefore, it was concluded that prepared material can be realized as white light source.

Berezovskaya et al. (2013) synthesized Ce^{3+} doped terbium aluminum garnet (TAG) phosphors by using the oxides of nano-structured of aluminum and rare earths. Aluminum oxide nano-particles were obtained by gaseous-disperse synthesis. It was observed that the Ce^{3+} doped TAG exhibited the intense broad band emission with a maximum at about 563 nm.

Dotsenko et al. (2013) prepared Ce doped terbium yttrium aluminum garnets(TYAG) using solid state reaction. The PL properties of prepared material were analyzed by excitation in the 2–20 eV regions. The doping of terbium ions for yttrium ions in the garnet structure broadened the emission spectra and also move maximum towards the longer wavelengths.

Park et al. (2013) synthesized Ce doped $Ln_3Ga_2Al_3O_{12}$, $Ln_3Al_2Al_3O_{12}$ and $Ln_3(LnAl)Al_3O_{12}$ crystalline powders by solvothermal reaction method in which L =Y, Tb, Gd, Eu, and Sm. It was concluded that emission wavelength of Ce ion of these samples was broaden as compared to Ce doped YAG. It was concluded that the $Ln_3Ga_2Al_3O_{12}$ and

$Ln_3Al_2Al_3O_{12}$ crystalline powders had 3-dimensional star-like morphology, size was in micron and better crystalline phase as compared to $Ln_3(LnAl)Al_3O_{12}$ garnet .

Podhorodecki et al. (2013) prepared the terbium (Tb 2.11 wt%)) doped $YAlO_3$ composites by co-precipitation method in which porous anodic alumina films was grown on silicon substrate. XRD and FTIR analysis confirmed the cubic phase of $YAlO_3$. Broad emission spectra were observed within the range of 350–640 nm which was due to f - f transitions of Tb ion. Due to defect states, abroad and fast decaying PL band in the blue range had been observed. The main excitation bands of Tb ions were due to 4f - 5d transitions and were observed at 235, 270 and 320 nm .

Wang et al. (2013) synthesized Ce and Eu doped YVO_4 crystals by Czochralski technique. It was observed that there was no effect on the crystalline phase due to doping. YVO4: Ce^{3+} and YVO_4: Ce^{3+},Eu^{3+} material was excited with 397 nm resulting in visible light emission. The values of chromaticity color coordinates were calcanted which were very close to that of an ideal white light source and concluded that prepared material could be realized for white light source.

Cheng et al. (2015) prepared Ce^{3+}-doped YAG nano crystalline material having grain size ranging from ∼19–30 nm using co-precipitation method followed by sintering at 1100^0C for 3 hrs. Aluminum nitrates, yttrium nitrates, and cerium nitrates were used as starting materials while ammonium sulfate was used as dispersant. Ammonium bicarbonate and ammonia were used as precipitating agents. Purity, particle size, and photoluminescence(PL) properties of Ce doped YAG nano-particles had been influenced by precipitation temperature, pH value of precipitant solutions, aging period, calcinations conditions and Ce-doping level. High-purity YAG nano-particles were synthesized at pH=10.50–11.00 and calcinations temperatures of 850–1100°C with a calcinations time of 3 hours. In the emission spectra of Ce doped YAG was shifted from 529 nm to 544 nm with increasing Ce concentration from 0.67 to 3.4 wt %. The high intensity PL peak was observed at Ce concentration at 1.3 wt.%.

Kharebe et al. (2015) prepared Ce and Eu $SrBPO_5$ and $CaBPO_5$ phosphors by solid state reaction. The excitation spectra of Eu doped $SrBPO_5$ phosphor showed the strong broad

emission peak at ~354 nm (monitored at 422 nm). The emission at 589 and 591 nm could be due to $^5D_0$–$^7F_1$ transition of Eu^{3+} while Ce^{3+}doped $SrBPO_5$ and $CaBPO_5$ showed a broad band emission at 375 nm.

Wang et al.(2015) synthesized Ce doped terbium-lutetium aluminum garnet .The emission spectra shifted toward the longer wavelength (37 nm) on doping. By adjusting the concentration if Tb and Lu ions in the garnet , the emission spectra can be tuned from green to Orange emission which is useful to improve the quality of white light from LED.

Hao et al.(2017) prepared the $Tb_3Al_{2.5}Ga_{2.5}O_{12}$ and compared its characteristics with TAG and TGG(Tb_3 Ga_5O_{12}). $Tb_3Al_{2.5}Ga_{2.5}O_{12}$ showed higher transmission (~ 80%) and high value of verdet constant (-150.6 rad/Tm) as compared to TGG and TAG

Dousti et al. (2017) prepared transparent zinc-alumino silicate glass ceramics containing cerium and europium ions which controlled the thermal heating of parent glasses. Addition of CeO_2 resulted in the improved transparency of the glasses in the visible spectral region. XRD patterns of the glass-ceramics indicated the formation of the crystalline gahnite phase. Characteristic of Ce^{3+} emission corresponding to the allowed f-d transitions was observed along with an anomalous emission in the red-infrared region. Color tunability from red to blue spectral region was observed.

Zhu et al. (2017) used melt quenching technique to prepare a series of Ce, Dy , and Eu doped oxyfluoride alumino borosilicate glasses. The red shift was found in the emission bands of Ce ions with the increase of excitation wavelengths and the molar ratio of B_2O_3/SiO_2, Al_2O_3/SiO_2, and B_2O_3/Al_2O_3 in the compositions of glass. This shift was also found on precipitation of CaF_2 crystals in glass.

2.3 Zinc Oxide

Perira et al. (2006) reported the Tb doped ZnO synthesis technique of colloidal nano-crystalline powder. Substitution of the Tb^{3+} ion in ZnO hosts result in photo-luminescent system in which emission spectra dependent upon excitation wavelength. It was also concluded that Tb ions were entered in the ZnO core.

Teng et al. (2006) prepared the Tb doped ZnO thin films using silicon substrate by magnetron co sputtering. The effect of annealing was studied on the morphological, structural and optical properties of Tb doped ZnO. Tetra-pod and screw like nano rod were obtained at annealing temperature of 950°C. PL Tb doped ZnO thin films with the tetra-pod structure and the screw like nano rods had two UV emission peaks and one strong green emission band due to surface defects. It was also concluded that PL intensity was increased with increase of annealing temperature.

Xiao et al. (2007) prepared the nano-sized Zinc Oxide thin films on quartz substrate using sol-gel process. Homogenous and dense surface ZnO thin films of grain size 30 nm were obtained and sol were remain stable for spin coating for seven day duration. ZnO thin film with Zn concentration of 0.8 mol/L showed 94% of transmittance in visible range when it annealed at 500^{o}C for 1 hour. Optical band gaps of ZnO thin films at different annealing temperatures were from 3.265 eV to 3.293 eV. Emission spectra showed a violet emission band located at 438 nm.

Ilican et al. (2008) deposited thin film of ZnO on glass substrates using the sol-gel spin coating. Absorbance and transmittance were recorded in the range from 190-900 nm using a double beam spectrophotometer. From the optical absorption, it was concluded that ZnO had direct band gap. From I-V plots of ZnO thin films carried out in dark and under UV-illumination it was concluded that ZnO thin films could be used as a photovoltaic material.

Suwanboon (2008) synthesized ZnO nano powder using zinc acetate dihydrate and poly vinyl pyrrolidone (PVP). XRD study confirmed the hexagonal wurtzite structure with crystallite size of 45 nm. TEM images showed the grain size of about 100 nm with diameter of about $3x10^{-4}$ M PVP. Studied the effect of PVP concentration on morphology of ZnO powders and it was concluded that shape changed from platelet-like to rod. ZnO powders had direct optical band gap of about 3.222-3.237 eV. Emission spectra showed the UV peak at 390 nm with slightly blue shift because of smaller grain size at higher concentration of PVP.

Awang et al. (2008) prepared Eu doped zinc oxide and Tb doped zinc oxide thin films on glass substrate using sol-gel dip-coating. Doping concentration of Tb and Eu was set in the range from 5 to 15 mol% in ZnO. The ZnO thin film had been characterized by XRD, FESEM and emission spectrometer. The Crystalline ZnO thin films were obtained at annealing temperature from 300 to 500^{o}C for 2 hours. Eu doped ZnO and Tb doped ZnO thin films were transparent in near UV and visible region. The grain size of thin films increased with the increase of annealing temperature from 300 to 500^{o}C. The XRD study confirmed the hexagonal wurtzite structure of ZnO and PL analysis concluded that the energy transfers took place from ZnO host to the dopent ions Eu and Tb .

Devi et al. (2009) prepared the ***z***inc oxide nano-particle of size of 20–30 nm under hydrothermal conditions. The average crystal size of the prepared ZnO nano powder was determined by XRD and was compared with TEM analysis and results were in good agreement .The absorption at wavelength less than 370 nm indicating that ZnO had smaller size nano-particles. PL spectra showed strong emission peak around 397nm.The quality and purity of ZnO nano-material crystalline samples was confirmed by photoluminescence spectra.

Soosen et al. (2009) synthesized ZnO nano-particles. Structure and morphology of the prepared samples were investigated by XRD and SEM, respectively. XRD confirmed the formation of wurtzite structure. Lattice contraction and average particle size were calculated using the XRD for ZnO. SEM images showed the spherical micrographs of ZnO nano particles. The UV absorption spectra showed blue shift in wavelength compared to bulk ZnO. Optical band gap of ZnO nano-particles were determined by using UV reflectance and it confirmed quantum confinement.

Dhar et al. (2011) prepared the Tb doped ZnO nano-particles and studied the structural and optical properties. Average diameter of ZnO nano-particle was 5 nm .Doping of Tb in the ZnO resulted in increase in optical band gap of ZnO. PL spectra of Tb doped ZnO showed the strong dependence of Tb concentration in ZnO and the ambient conditions. PL spectra showed the green peak in the emission spectra of Tb doped ZnO whose intensity strongly dependent upon atmospheric condition Tb concentration in ZnO. Under

vacuum condition, the GL intensity decreased and almost suppressed with the increase of Tb concentration up to mole fraction ≈ 0.02.

Murmu et al. (2011) implanted the 30 KeV Gd in ZnO and studied the structural and PL properties of ZnO single crystals. At low implantation, Gd atoms were to be in sites and aligned with the ZnO lattice whereas, at higher implantation, Gd atoms disordered the ZnO lattice. The Raman spectra of the Gd implanted in ZnO samples showed defect-induced modes In annealed sample lattice is almost free from the defect induced by Gd in ZnO lattice. Low temperature PL spectra showed a red shift in the defect emission.

Sharma et al. (2012) prepared the Tb doped ZnO and studied the structural and optical properties of Tb doped ZnO nano-particles with average diameter of 4 nm. XRD analysis showed a contraction in ZnO lattice with the increase of Tb Concentration(x) for $x \leq 0.02$(mole fraction) and an expansion beyond x=0.02. The PL spectra had near band edge Ultra violet luminescence (UVL) and green luminescence (GL) band. PL intensity of GL band increased, with the increase of Tb concentration in ZnO under atmospheric conditions over the entire doping range, whereas, under the vacuum condition, GL intensity decreased with the increase of Tb concentration in ZnO up to 0.02 but further increase of Tb concentration led to a slowly increase in GL emission. Study suggested that for Tb concentration in ZnO is less than or equal to 0.02, it was concluded that Tb incorporated mostly on the surface of the nano-particles which affected the UVL to GL intensity ratio, However, when Tb concentration in ZnO was greater than 0.02, GL originated both from the GL-groups as well as from point defects also which were generated due to the Tb doping in ZnO

Bedyal et al. (2012) synthesized Europium (Eu) and Cerium (Ce) doped ZnO powders by sol-gel method from zinc acetate, sodium hydroxide and ethanol used as starting material. The concentrations of both Eu and Ce doped in ZnO were 0.1, 0.5 and 1 mol. FTIR and XRD studies showed that the crystal structure of ZnO remained unchanged on doping. The Photoluminescence measurements showed characteristic blue (~400 nm) emission due to ZnO, yellow (550 nm) emission of Ce and red (630 nm) emission of Eu implying the potential use of (Eu, Ce):ZnO as white light source.

Xiying et al. (2012) prepared the Gd doped ZnO nano-particle by using thermal evaporation vapor phase deposition technique and analysed the light emission properties from Ultra-Violet to blue emission. Gd concentration varied from 0% (pure ZnO) to 15% at 500°C. ZnO nano-crystals emission spectra consist of strong 375 nm UV peak. ZnO nano-crystals had two peaks at 432 and 397 nm for the sample doped with 5% Gd. Incorporation of Gd in ZnO generated the defect states in band gap responsible for board emission. It was concluded that the optical properties of ZnO could be controlled with level of doping concentration of Gd in ZnO.

Mithal et al. (2013) prepared Gd doped ZnO nano-particle using sol-gel method. It was found that doping of Gd in the ZnO modified the PL spectra of undoped ZnO and broad emission was observed from UV to visible range.

Nadia et al. (2013) synthesized Ce-doped ZnO nano-particles by the co-precipitation method. XRD confirmed the formation of wurtzite and no additional phase was observed in Ce doped ZnO. The average grain size of Ce doped ZnO and was found to be in the range of 13 to 16 nm. UV absorption measurements indicated a red shift due to doping in ZnO after doping that had reflection spectra in the visible region from 300 and 800 nm. In addition to that, the formation of oxygen vacancy and an electron trapped at cerium site in Ce doped ZnO were studied using electron spin resonance.

Bindu et al. (2014) prepared nano-particles ZnO powder using precipitation method. It had Hexagonal wurtzite structure. Crystalline nature of ZnO nano-particles were studied by X-ray peak profile analysis. The peak broadening crystallite size and lattice stain were analyzed by using Williamson–Hall analysis. The crystallite size was calculated by using Scherrer's formula, Williamson–Hall plots and size–strain plot was compared with the particle size obtained from TEM and showed very less deviation.

Koao et al.(2014) prepared Eu (0.2 to 5 mol%) doped ZnO nanostructure by the chemical bath deposition (CBD) method. XRD results of undoped and low concentration Eu doped ZnO corresponded to the various planes of a single hexagonal ZnO phase. The estimated crystalline grain size was calculated using the XRD spectra and was found to be in the order of 47±5 nm and independent on the Eu ion concentration up to 4 mol%. SEM

micrograph showed that the introduction of Eu affected the morphology of the samples. In the UV absorption study, the highest band gap energy was obtained for the undoped ZnO. The effective band gap of ZnO decayed exponentially and generated the impurities due to doping of Eu up to 4 mol%. Poor luminescence was observed for excitation greater than band gap at 300 nm, the highest emission was obtained by exciting the Eu ions directly through the $^7F_0 \rightarrow {}^5L_6$ absorption band at 395 nm without any noticeable ZnO defect emissions. The maximum luminescence intensity for this excitation was obtained for ZnO:3 mol% Eu^{3+} ions and luminescent quenching was observed for higher Eu concentrations.

Rani et al. (2015) prepared the thin films of Gd doped ZnO and studied the structural and optical properties by using XRD, SEM, PL and UV-Vis spectrophotometer. The FWHM of XRD peaks increased with increase of Gd concentration and this implied decrease in the crystalline quality of the films. These results were confirmed with SEM results. PL peak in the UV region had a strong shift towards higher wavelength with increasing concentration of Gd. The optical band gap was determined from UV visible transmission spectrum. The optical band g ap was found to be 3.29 eV for pure ZnO film and it decreased with the increase of Gd concentration.

Singh (2015) prepared the Eu^{+3} doped ZnO by wet chemical method at low temperature and concluded that Eu^{+3} might occupy either Zn^{+2} lattice site or on surface of ZnO. X- ray diffraction results showed the significant phase segregation on the annealing the sample and compared them with lower heated samples. This phase segregation resulted in decrease in luminescence intensity of annealed ZnO doped Eu nano-particles as compared to low temperature heated ZnO doped Eu nano-particles. Nano-particles of ZnO, ZnO doped Eu (2 wt.%) and ZnO doped Eu covered with yttrium matrix were synthesized . Improvement in luminescence emissions was observed when ZnO doped Eu nano-particles were covered with yttrium matrix.

Chouchene et al. (2016) prepared the Ce doped ZnO by solvothermal method and studied the optical and electrical properties of the prepared samples by using XRD, SEM, TEM, XPS, DRS and Raman spectroscopy characterization techniques. ZnO: Ce 0.5 % rod had an average length of 130nm and diameter of 23 nm and showed the highest

photcatalytic activity for the degradation of orange II dye under the solar irradiation. Ce-doping not only increased the surface area of photo catalysts but also induced a red-shift in the absorption and improved the solar and visible light capacities

Layek et al (2016) prepared the rare earth(Eu and Tb) ions doped ZnO nano rods. Prepared material had hexagonal wurtzite structure.Rare earth doped ZnO had broad visible range spectra due to the intrinsic and extrinsic defects in the host lattice ZnO. Energy transfer take place from defects center in host to dopent site.

Zhu et al. (2016) demonstrated a quantum yield of ~70% in the visible region of the emission from ZnO/polyacrelic acid (PAAH) nanocomposite. This quantum yield was observed to be stable over several months indicating its potential in the realization of the light sources.

Ding et al. (2017) investigated the effect of Al capping on the photoluminescence (PL) of ZnO. They not only observed enhancement in the intensity of the PL emission but also observed negative thermal quenching temperature dependence. The observed phenomenon was explained in terms of the coupling between ZnO exciton and the surface Plasmon's of Al.

Liu et al. (2017) demonstrated a one-pot synthesis technique for the commercial production of ZnO nanoparticles; ~ 34 g of yield was obtained on synthesis cycle. Yellowish LEDs with luminous efficiency of ~ 64 lm/W were fabricated from the synthesized ZnO powder. Very little degradation of the output emission was observed up to 100^0C.

2.4 Motivation for the present investigation

The literature reviewed indicated the following gaps in the chosen research field which provided the motivation for the present investigation.

(a) Ce: YAG is commercially used for the fabrication of LEDs. However, these LEDs lack the red part of the visible spectrum which is present both in "sunlight" as well as in "filament lamp" emission. It is known that the emission from Ce doped TAG has more

red component when compared with Ce: YAG. Also Eu has strong emission in red region. There are a few investigations where both Ce and Eu co-doped in TAG but a detailed investigation was required for providing a motivation to investigate Ce and Eu co-doped in TAG for its potential in the realization of white light sources.

ZnO is known to have emission in visible region which is attributed to the defect states in the ZnO lattice. This visible emission can be tailored by doping providing an impetus to undertake an investigation in this direction. Since rare-earth elements have emission in visible region, besides, other unique properties were chosen as dopants for investigation. Single doped Gd was not reported, Tb needed revisit for more detailed investigation while chromaticity color co-ordinates needed to be calculated from the visible emission in Ce and Eu single doped ZnO. There was one investigation on ZnO co-doped with Ce and Eu which lacked details about the visible emission. Also, no investigation was reported on ZnO co-doped with Ce, Eu and Tb. All these gaps were filled, to the best of our ability, in this investigation.

REFERENCES

[1] Boyer J C,Vetrone F, and Capobianco J A (2004) *Chemical Physics Letter* 390 : 403–407

[2] Mazur et al. (2005) *Material Science-Poland* 23: 261-268

[3] Potdevin et al. (2005) *Journal of Physics D: Applied Physics* 38: 361-368

[4] Nazarov M , Sohn J and Yoon C (2006) *Moldavian Journal of the Physical Sciences* 5: 3-4

[5] Jung K Y and Lee H W (2006) *Journal of Luminescence* 126: 469–474

[6] Chiang C C, Sai M S T and Hon M H (2007) *Journal of The Electrochemica Society* 154 : J326-J329

[7] Liu et al.(2007) *Journal of The Electrochemical Society*, 154: J11-J14 doi : 10.1149/1.2382670

[8] Nazarov et al. (2007) *J. Solid State Chem.*180:2493–2499

[9] Vasil et al.(2007) *Physics of The Solid State* 49: 478-483

[10] Zorenko et al. (2007) *Radiation Measurements* 42: 648–651 doi: 10.1016/j. radmeas.2007.01.059

[11] Fadlalla et al. (2008) *Mater. Res. Bull* 43: 3457–3462

[12] Zorenko et al. (2008) *Journal of Luminescence* 128: 652–660 doi :10 .1016/ j.jlumin.2007.11.069

[13] Mhin et al.(2009) *Nanoscale Res Lett* 4:888–895

[14] Psuja et al.(2009) *Journal of Rare Earths* 27: 574-578

[15] Shabir H , Lal B and Rafat M (2009) *Journal of Nano and Biomaterials* 2: 416-424

[16] Shabir H, Lal B and Rafat M (2010) *Journal of Sol-Gel Science Technology*, 53:399–404

[17] Shabir H, Lal B and Rafat M (2010) *Journal of ceramic international* 36:365-369

[18] Zorenko et al. (2010) *Journal of Luminescence*, 130: 380–386 doi: 10.1016 /j.jlumin. 2009.09.024

[19] Shaat et al. (2012) *Optical Materials Express* 2 :962-968

[20] Berezovskaya et al. (2013) *J. NANO- ELECTRON. PHYS.* 5:1-3

[21] Dotsenko et al. (2013) *Journal of alloys and compounds* 550: 150-163

[22] Park et al. (2013) *Current Applied Physics 13*: 441-447

[23] Podhorodecki et al. (2013) *J. Phys. D: Appl. Phys.*46:1-12 doi:10.1088/0022-3727/46/35/355302

[24] Wang et al. (2013) *Journal of Alloys and Compounds* 551: 262-266

[25] Cheng et al. (2015) *Journal of Rare Earths* 33: 591- 598

[26] Kharebe et al. (2015) *Optik - International Journal for Light and Electron Optics* 126: 4544-4547

[27] Wang et al. (2015) *Int. J. Electrochem. Sci* 10:2554 - 2563

[28] Hao et al.(2017) *Int J Appl Ceram Technol* 14:399-403 doi: 10.1111/ijac.12660

[29] Zhu et al. (2017) *Journal of Luminescence* 183: 32-38

[30] Dousti et al. (2017) *Optical Materials* 69:372-377

[31] Pereira et al.(2006) *Journal of Nanotechnology* 17: 834-839 https://doi.org/ 10.1088/0957-4484 /17/3/037

[32] Teng et al. (2006) *Journal of applied physics* 100:1-5

[33] Xiao et al. (2007) *Trans. Nonferrous Met. Soc. China* 17:814-817

[34] Ilican S, Caglar Y and Caglar M (2008) *Journal of Optoelectronics and advanced materials* 10:2578 – 2583

[35] Suwanboon (2008) *Science Asia* 34:031-034

[36] Awang et al. (2008) *Solid State Science and Technology* 16: 45- 54

[37] Sridevi D and Rajendran K V(2009) Bull. Mater. Sci. 32: 165–168

[38] Soosen S M, Lekshmi B and George K.C. (2009) *Academic Review* V XVI: 57-65

[39] Dhar S, Singh B P and Kunda T (2011) *International Conference Pub* 17:1-5

[40] Murmu et al. (2011) *J. Appl. Phys.* 110:1-6 doi:10.1063/1.3619852

[41] Sharma et al. (2012) *Journal of Nano part Res* 14: 1-12

[42] Bedyal et al. (2012) *BVS Conferences* 90

[43] Xiying Ma and Zui Wang (2012) *Materials Science in Semiconductor Processing* 15:227-231, https://doi. org/10.1016/j.mssp. 2011.05.013

[44] Mithal et al. (2013) *Asian J Chem* 25:S12-S16

[45] Nadia Febiana Djaja and Rosari Saleh et al (2013) *Materials Sciences and Aplications*, 4:145-152 http://dx.doi.org/10.4236/msa.2013.42017

[46] Bindu P and Thomas S (2014) *Theor Appl Phys* 8:123–134 DOI 10.1007/s40094-014-0141-9

[47] Koao et al (2014) *Journal of Luminescence* 147: 85-89

[48] Deepa Rani T and Tamilarasan K (2015) *Int.J. ChemTech Res* 8: 2227-2233

[49] Singh (2015) *Materials Sciences and Applications* 6: 269-278. http://dx.doi.org/10.4236/msa.2015.64032

[50] Chouchene et al. (2016) *Beilstein J. Nanotechnol* 7:1338-1349. doi:10.3762/bjnano.7.125

[51] Layek et al. (2016) *RSC Adv.* 6: 35892-35900

[52] Zhu et al. (2016) *Scientific Reports* 6:23557

[53] Ding el al. (2017) *Opt Mater Express* 6:1898-1905

[54] Liu et al. (2017) *Opt Mater Express* 7: 2686-2690

CHAPTER 3

EXPERIMENTAL DETAILS

3.1 Introduction

ZnO (zinc oxide) and TAG (terbium aluminum garnet) nano powders doped with rare-earths, as mentioned earlier, were investigated in the present investigation. The doped ZnO samples were prepared by the co-precipitation technique while the sol gel synthesis was employed for the preparation of the doped TAG. ZnO was singly doped with Gd (gadolinium), Tb (terbium), Ce (cerium) and Eu (europium), doubly co-doped with Eu and Ce and triply co-doped with Ce, Eu and Tb. On the other hand, TAG was singly as well as doubly co-doped with Ce and Eu. An in-house facility for the synthesis of the nano powder samples both by the precipitation as well as by the sol gel techniques were developed at Physics Department of Lovely Professional University, Phagwara while the prepared samples were characterized by XRD, FTIR, SEM, TEM and optical spectroscopic techniques at the Department of Metallurgical Engineering and Material Science , IIT, Bombay and School of Chemical Sciences Engineering and Physical Sciences ,Lovely Professional University, Phagwara.

3.2 Synthesis of ZnO and doped ZnO

Co-precipitation method which is a low temperature, simple, rapid preparation, good homogeneity, low cost, high purity of the synthesized material, easy control of both the particle size as well as that of composition, required only a few organic solvents, was used for the synthesis of the doped ZnO; the samples, thus, prepared were sintered in air (700^{o}C maximum) using a home built muffle furnace fitted with a temperature controller which could control the sintering temperature within $\pm 1^{o}$C.The starting materials (Table 3.1) for the preparation of ZnO were zinc acetate and oxalic acid while europium oxide (Eu_2O_3), terbium oxide (Tb_4O_7), gadolinium nitrate ($Gd(NO_3)_3.6H_2O$) and cerium nitrate ($Ce(NO_3)_3.6H_2O$) were used for doping. All these chemicals were used as purchased without any further purification.

Table 3.1: List of chemical used in the preparation of undoped and rare earth doped ZnO

S.No.	Chemical Name	Molecular Weight (g $mol^{-1)}$	Purity	Manufacturer
1.	Zinc acetate $(CH3COO)_2.2H_2O)$	219.50	AR(99.9%)	LOBA Chemical
2.	Oxalic acid $(C_2H_2O_4)$	126.07	LR (99%)	LOBA Chemical
3.	Cerium nitrate $(Ce\ (NO_3)_3.6H_2O)$	434.23	AR(99.9%)	LOBA Chemical
4.	Europium Oxide (Eu_2O_3)	351.92	LR (99.9%)	LOBA Chemical
5.	Gadolinium nitrate $(Gd\ (NO_3)_3.6H_2O)$	451.36	AR(99.9%)	CDH chemicals
6..	Terbium oxide (Tb_4O_7)	747.69	LR (99.9%)	CDH chemicals

0.1M solutions of zinc acetate and oxalic acid prepared in distilled water were mixed and the mixture, thus, formed was stirred for 12 hours resulting in the formation of a milky solution. To this milky solution, dopant solutions prepared in distilled water by dissolving the appropriate amounts of rare-earths were added and the whole mixture was stirred for 12 hours while maintaining the solution temperature at 90^oC. The precipitate, thus, obtained was filtered and dried at 120°C for 6 hours after washing with acetone and distilled water. The solid samples, thus, obtained were hand crushed into fine powder and sintered at 700^oC using a home-built temperature controlled ($\pm1^oC$) muffle furnace. The dopant concentrations used in the present investigation were 0.1, 0.5 and 1.0 mol. %.

$$Zn\ (CH_3COO)_2{\cdot}2H_2O + H_2C_2O_4{\cdot}2H_2O \rightarrow ZnC_2O_4.XH_2O + CH_3COOH + 2H_2O \quad (3.1)$$

$$ZnC_2O_4{\cdot}XH_2O \rightarrow ZnO + CO + CO_2 + XH_2O \quad (3.2)$$

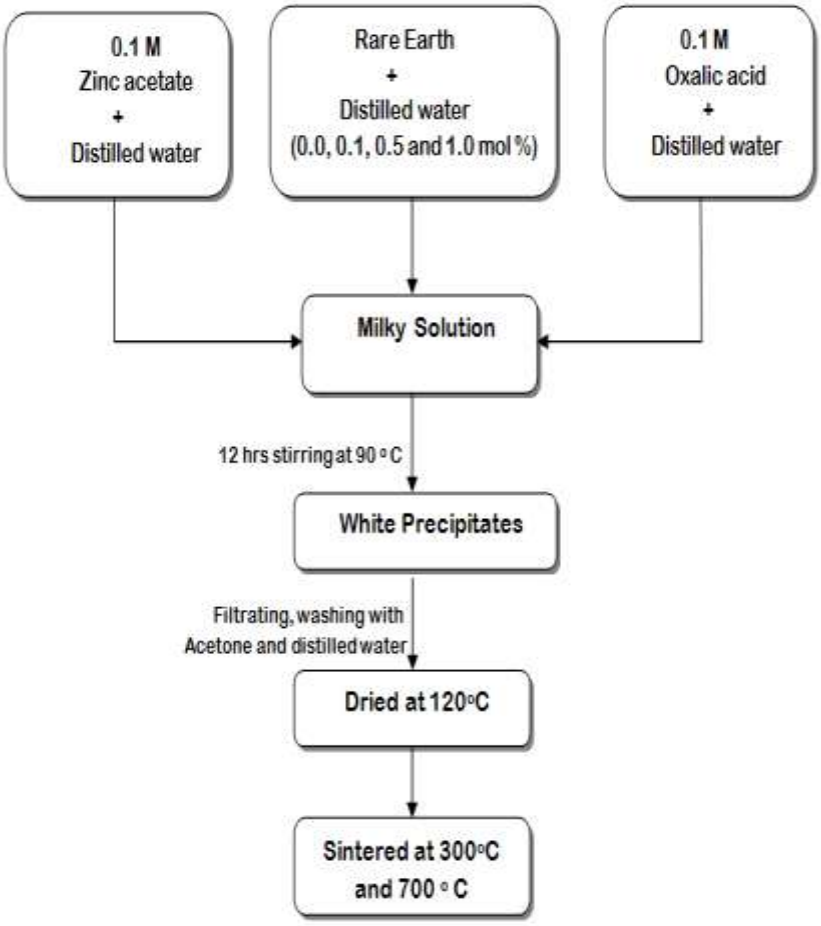

Fig.3.1: Flow chart of co-precipitation synthesis of undoped ZnO and doped ZnO

The list of the powder samples prepared is summarized in Table 3.2. As seen in this table, eight single doped, 19 double doped and nineteen triple doped powder samples were prepared by permuting of concentrations investigated in the present work.

3.3 Sol gel synthesis

The sol-gel technique is a versatile process used in making various colloidal dispersions of metal oxides at low temperature. From such colloidal dispersions, powders, fibers and thin films can be readily prepared. Although the fabrication of different forms of final products requires some specific consideration, the fundamentals and general approaches in the synthesis of colloidal dispersions are the same. In a typical sol-gel process, a colloidal suspension or a sol is formed from hydrolysis and polymerization reactions of

Table: 3.2: List of the synthesized doped ZnO powder sample

Dopant	Dopant conc. (mol%)	No. of samples prepared
Single doping Eu_2O_3, Tb_4O_7, Gd $(NO_3)_3.6H_2O$ and Ce $(NO_3)_3.6H_2O$.	0.1, 0.5 and 1.0	8
Double doping Eu_2O_3 and Ce $(NO_3)_3.6H_2O$.	0.1, 0.5 and 1.0	9
Triple doping Eu_2O_3, Tb_4O_7 and Ce $(NO_3)_3.6H_2O$.	0.1, 0.5 and 1.0	19

precursors. Complete polymerization and loss of solvent leads to transition from the liquid sol into gel phase. Thin films can be produced on a piece of substrate by spin coating or dip coating. A wet gel will form when sol is cast into mould and wet gel is converted into a dense ceramic with further drying and heat treatment. A highly porous and extremely low density material called an areogel is obtained if the solvent in wet gel is removed under a supercritical condition. Thus, sol-gel involves the evolution of networks through the formation of colloidal suspension (sol) and gelatin to form a network in continuous liquid phase (gel).

Sol gel technique has many advantages including low processing temperature and molecular level homogeneity. Sol gel processing is particularly useful in making complex metal oxides, thermodynamically unfavorable and metastable materials.

Sol gel involves the formation of concentrated suspension of a metallic oxide or hydroxide (sol), which is subsequently dehydrated by evaporation or solvent extraction,

resulting in a semi-rigid mass (gel). A wide range of mixed oxides can be produced on controlled heating of this gellated material. The process gives a good control over composition and particle size and substantial reduction in the formation temperature.

3.3.1 Synthesis of Ce and Eu doped TAG Powder.

The starting material used for the preparation of TAG is listed below in Table 3.3. TAG /rare earth doped TAG were prepared by sol–gel technique through nitrate-citrate route followed by sintering in air (1100 °C maximum temperature)

Table 3.3: List of chemical used in the preparation of undoped and rare earth doped ZnO

S.No.	Chemical Name	Molecular Weight (g $mol^{-1)}$	Purity	Manufacturer
1.	Terbium oxide (Tb_4O_7)	219.50	LR (99.9%)	Alfa Aesar
2.	Aluminum Nitrate ($Al(NO_3)_3.9H_2O$)	375.13	AR (98.5%)	LOBA Chemical
3.	Cerium nitrate (Ce $(NO_3)_3.6H_2O$)	434.23	AR(99.9%)	LOBA Chemical
4.	Europium Oxide (Eu_2O_3)	351.92	LR (99.9%)	LOBA Chemical
5.	Citric acid ($C_6H_8O_7.H_2O$)	210.14	AR(99.5%)	LOBA Chemical

The steps involved in sol gel synthesis of Ce and Eu doped TAG are as follows:

Step1: Weighing and mixing of reactants

Appropriate amounts of the metal salts of terbium, aluminum, Ce and Eu were weighed (using Model APS-0 Atco Palm Scale with 0.01g least count) carefully and dissolved in de-ionized water so that the stoichiometric ratio of terbium and aluminum was 3:5. The respective solutions of these metal salts were mixed together while stirring continuously using magnetic stirrer. The solution, thus, obtained was heated simultaneously on a silicone oil bath.

Step 2: Chelation:

The chelating agent (like citric acid) was added to the heated mixture which was continuously stirred keeping the temperature at 65oC till a homogenous mixture was obtained.

Step 3: Sol formation:
After 10 hours of stirring, the resultant mixture was kept for concentrating on the oil bath for a few hours on an increased temperature of about 75^{o}C.

Step 4: Gelation:
After few hours, an interconnected, rigid network with pores of sub micrometer dimensions, called gel was obtained.

Step 5: Drying
The gel, thus, obtained was dried in an oven at about 120^{o}C. The fluffy amorphous substance as shown in Fig.3.4 (b,c), thus, obtained was hand ground with pestle in a mortar. The powders were calcined in alumina crucible at 200^{0}C for a few hours before subjecting it to thermal treatments at various higher temperatures. All the steps are summarized in Fig 3.2

3.4 Experimental facility (in-house)

An in-house facility was developed at the Physics Department of Lovely Professional University, Phagwara to prepare the samples both by co-precipitation as well as sol gel techniques. The main parts of this facility are as shown in Fig 3.3 .

1. A home- made muffle furnace having Kanthal-A1 wire as heating element was used. A chromel alumel thermocouple was used to monitor the temperature. The temperature of the furnace is controlled by commercial temperature controller which can control the required temperature within $\pm 1^{o}$C. The furnace is designed to produce ~ 1400^{o}C at the center of the alumina tube over which the heating element is wound- the tube is well insulated thermally to be housed in an aluminum jacket. The furnace can be used in ambient conditions. Electric power (220V AC) to the furnace is fed through an auto-transformer so that furnace can be set to any desired temperature in the range 50-1400^{o}C.

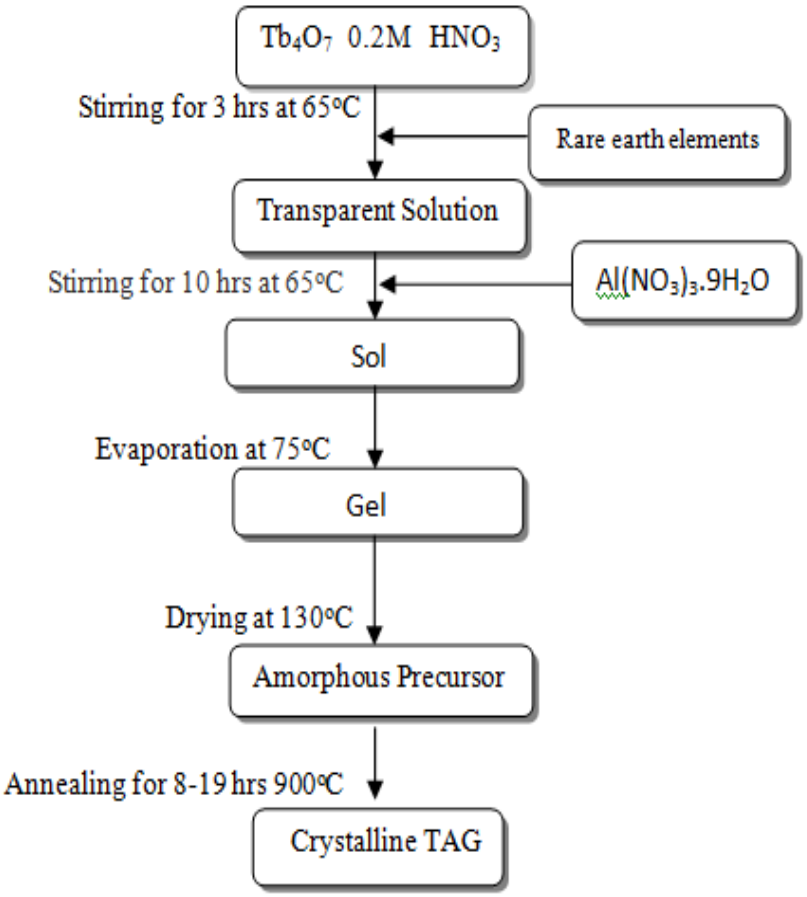

Fig.3.2: Flow chart of sol gel synthesis used to prepare Ce and Eu doped TAG.

2. A commercial electronic sonicator for homogenization of the solutions
3. Commercial oil and water baths fitted with magnetic stirrers; silicone oil was used for the water bath.

Fig. 3.3: In- house facility for the preparation of sample powders by sol-gel technique and co-precipitation technique setup in the Physics Labs of LPU.

A typical synthesis cycle for the preparation of TAG is shown in Fig 3.4

(a) (b) (c)

Fig.3.4: (a)Sample on magnetic stirrer (b & c) TAG Precusor after drying at 130^{o}C

3.5 Characterization Techniques

The samples were prepared at LPU and characterized both at IIT, Bombay and LPU, Phagwara. Samples were characterized, as mentioned earlier, by XRD, SEM.TEM, EDX, UV-VIS absorption spectroscopy, Raman scattering, FTIR and photoluminescence techniques. The instruments used for the characterization are discussed in the following sections.

3.5.1. X ray Powder Diffraction (XRD)

XRD spectra of the powder samples were recorded using Model Philips X perts XRD system Fig.3.5(a). In this system, XRD spectra was excited by K-alpah1 and K-alpha2 of wavelengths 1.540598Å and 1.544426 Å. The X- ray scanning was done in the range of 10 to 80 degree in the step of 0.001. Typical XRD pattern is shown in Fig 3.5(b)

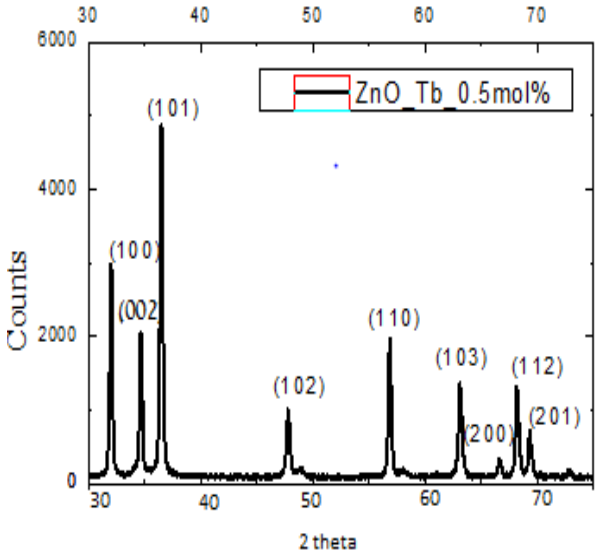

(a) (b)

Fig.3.5: (a) Photograph of the Model Philips X perts XRD system (b) Typical XRD Pattern

XRD data were analyzed to (i) check the change in the crystal structure of the host material (TAG and ZnO) on doping with various rare-earths and (ii) change, if any, in the lattice constants, cell volume and crystallite size to assess the lattice distortions induced in the host lattice by the dopants.

3.5.2. Scanning Electron Microscope (SEM)

Model Jeol JSM-7600F (Fig 3.6a) was used to record SEM images. Typical SEM image is shown in Fig 3.6b

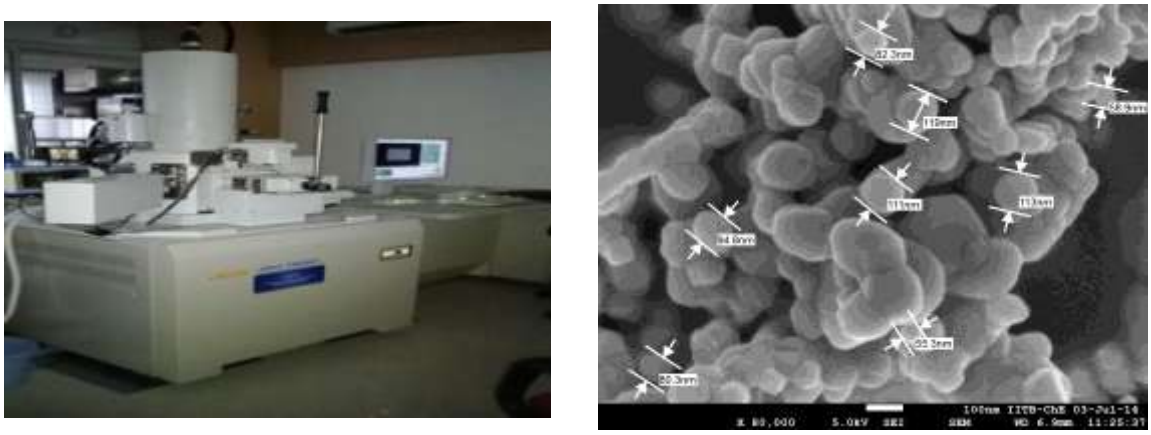

(a) (b)

Fig 3.6: (a) Photograph of the Model Jeol JSM-7600F SEM (b) Typical SEM image

Since the electrons in a SEM scan the surface of the sample image recored by it provides the information about the surface morphology (shape and size of the particles constituing the surface of the sample) of the sample. Any deviation from the expected shape of the particles can give information about the strain developed in the host material because of the lattice distortions induced by dopants.

Same instrument can be used to investigate the composition of the sample by technique known as energy-dispersive X-ray spectroscopy (EDX). A typical EDX spectra is shown in Fig 3.7

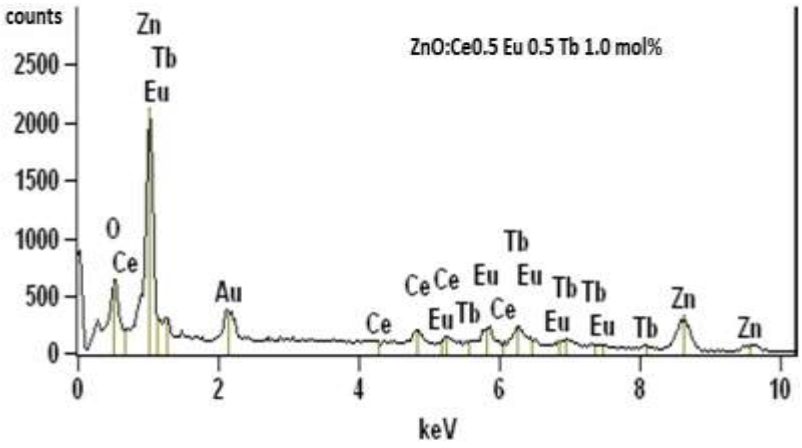

Fig 3.7: Typical EDX spectrum

As seen in Fig 3.7 peaks, (on energy scale) of the dopants along with those of host are prominently seen in the spectrum. The intensity of the EDX spectrum can give information about the amount of a particular element present in the sample. The Au peak in Fig 3.8 is due to gold sample holder used to record the SEM image.

3.5.3 Transmission Electron Microscope (TEM)

Mode JEM 2100F(Fig 3.8a)TEM was used to record the TEM images of the samples

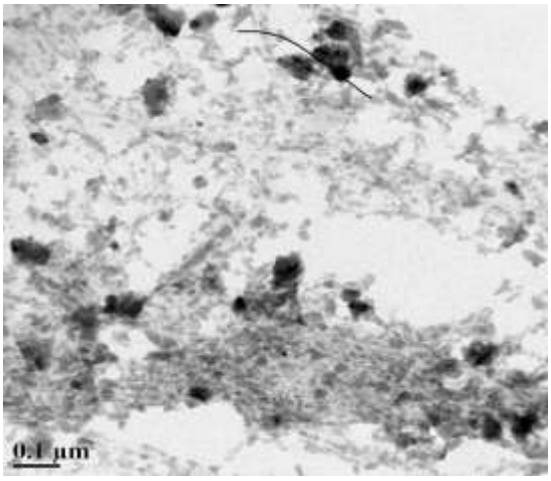

(a) (b)

Fig 3.8: (a) Photograph of the Mode JEM 2100F TEM (b) Typical TEM image

The electrons in a TEM are transmitted through a thin slice of the sample to investigate the internal structure of the sample. A typical; TEM image is shown in Fig 3.8b**.** The electrons in a TEM can be directed towards a single particle so as to get electron diffraction pattern to assess the extent of the spherical symmetry of that particle.

3.5.4 Fourier Transform Infrared Spectroscopy (FTIR)

Model Shimadzu FTIR 8000 Series spectrometer (Fig 3.9a) was used to record the FTIR spectra using standard KBr pellet technique- a mixture of the sample and KBr was pressed into a pellet to record the spectrum in 400-4000cm^{-1} in air(Fig.3.9b).

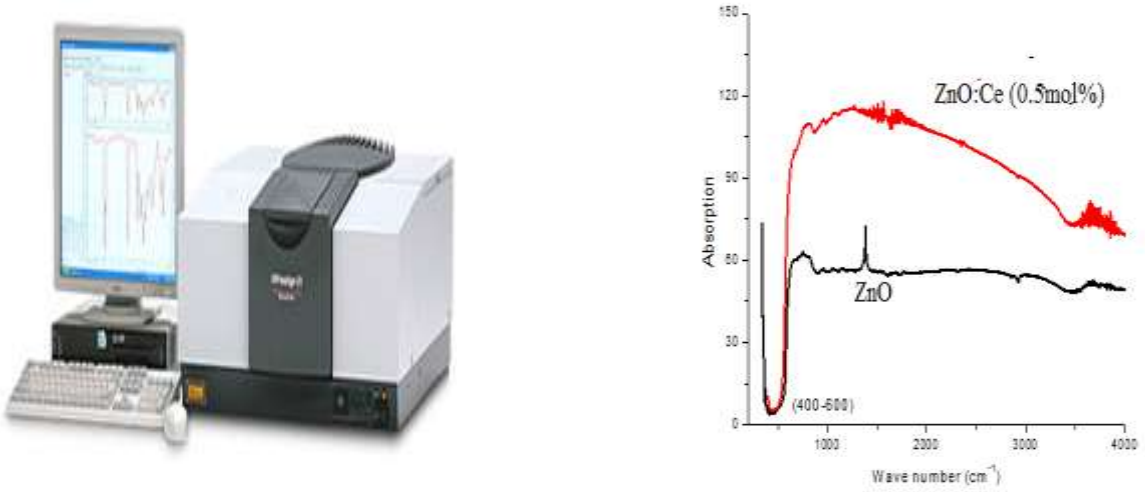

(a) (b)

Fig 3.9: (a) Photograph of the Model Shimadzu FTIR 8000 Series spectrometer (b) Typical FTIR spectra

Relatively strong absorption in 400-600 cm^{-1} was due to Zn-O and Ce-O bonds and relatively weak absorption around 3500cm^{-1} was due to water present in air. More often absorption due to C-O bonds and due to other chemicals present in air were seen in FTIR spectrum so one has to be careful while analyzing FTIR spectrum.

3.5.5 Ultra Violet and Visible (UV-VIS) Absorption Spectroscopy

Shimadzu Model UV-VIS Absorption 1800 spectrometer (Fig 3.10a) was used to record absorption spectrum in 200-700nm region. This spectrometer is fitted with deuterium-discharge lamp for UV measurements and a tungsten halogen lamp for visible and NIR spectral regions.. The instrument automatically swaps lamps when scanning between the UV and visible regions.

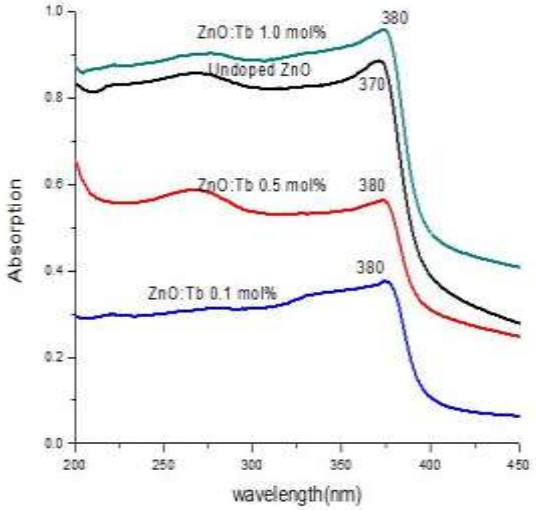

(a) (b)

Fig 3.10: (a) Photograph of the Shimadzu Model UV-VIS Absorption 1800 spectrophotometer (b) Typical UV-VIS spectrum

Typical UV-VIS absorption spectra are shown in Fig 3.10b. The spectra provides useful information about the change in absorption on doping along with the absorption edge which is very important parameter if one is looking for a material to develop a device for a particular electromagnetic region.

3.5.6 Fluorescence Spectrometer

The emission from the samples when excited with the radiation absorbed by it was recorded using the Varian Model Carry 8000 Spectrophotometer (Fig 3.11a). Radiation

from a Xe lamp was selected to excite the emission and the emission spectrum in 200-700nm was recorded-the focus of the present study, as mentioned earlier, was emission in 400-700nm region.

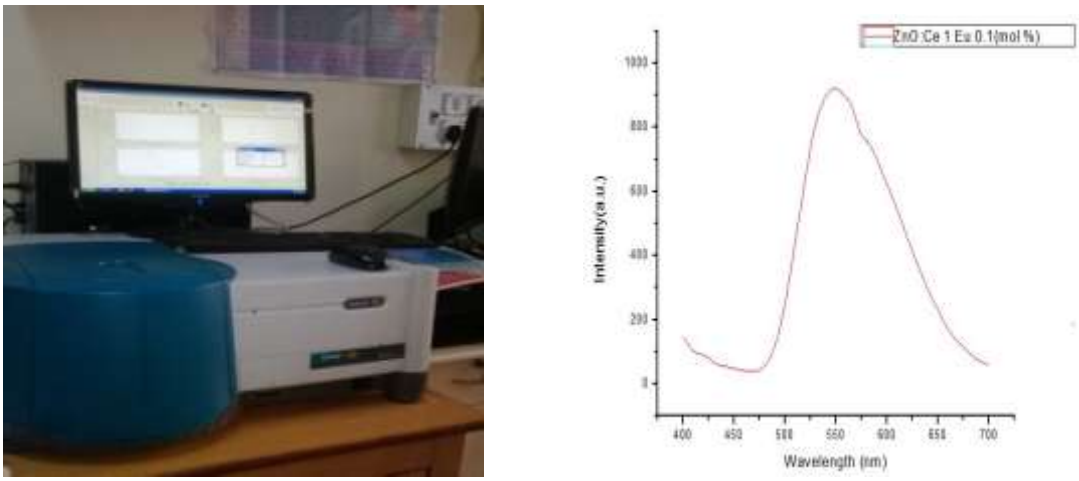

(a) (b)

Fig. 3.11 : (a)Phtograph of the Varian Model Carry 8000 Spectrophotometer
(b) Typical 280nm radiation (from Xe lamp) excited emission spectrum

Typical emission spectrum excited with 280nm radiation from a Xe lamp and recorded on this instrument is shown in Fig 3.11b.

3.5.7 Raman Spectrometer

Model Morrison, Microscope Olympus Bx 41 Raman spectrophotometer (Fig 3.12a) was used to record the Raman emission excited by 514.5nm radiation from an Ar-ion laser. Raman spectra in the present investigation were used to assess the extent of lattice distortions induced in the host by the dopants as Raman scattering is very sensitive to lattice strain resulting from lattice distortion.

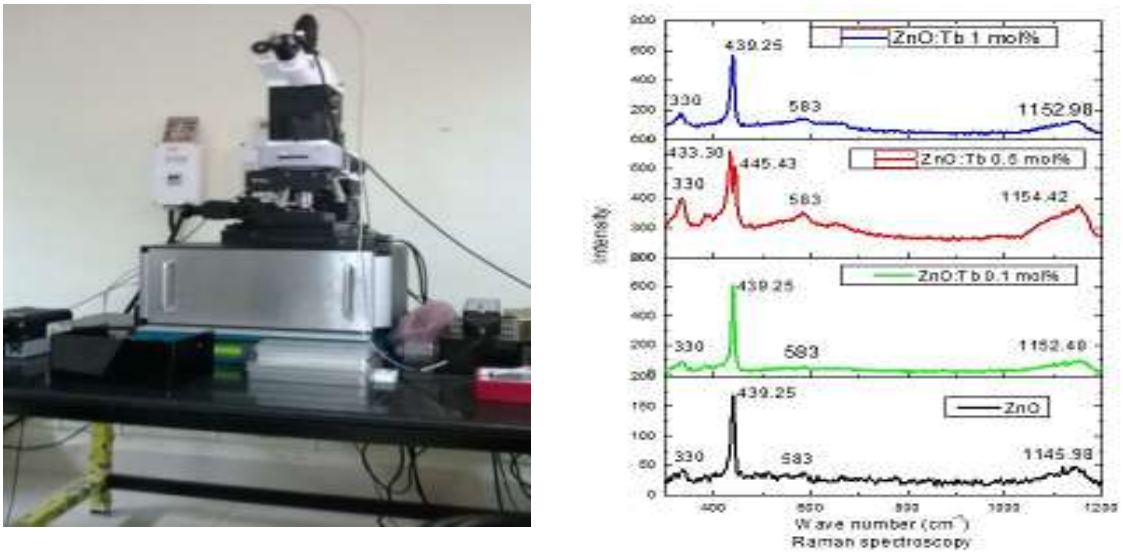

(a) (b)

Fig.3.12: (a) Photograph of the Morrison, Microscope Olympus Bx 41 Raman spectrophotometer (b) Typical Raman spectra obtained by using instrument describe in part 'a'.

CHAPTER 4
TERBIUM ALUMINUM GARNET (TAG) NANO PHOSPHOR CO-DOPED WITH Ce AND Eu

4.1 Introduction

TAG crystal of any significant size, as mentioned in Chapter 1, is not possible with the present day techniques because of its inherent incongruent melting properties [1], hence its application in powder form is being investigated recently. Conventionally, TAG powder was prepared by solid state reaction yet recently [2] nanostructured powder was prepared successfully. Also, the variation of its nanostructured properties by sintering the sol gel prepared samples by laser has been reported[3]. Characteristic redemission was observed when TAG was doped with Eu [4]. Similarly, characteristic yellow emission from Ce was observed in Ce doped YAG [5,6]. Batentschuk et al.[7] found energy transfer from Ce to Eu via Tb in YAG co-doped with Ce and Eu. However, they did not investigate the emission details with various excitations which is reported in the present study where un-doped and co doped (with Ce and Eu) terbium aluminum garnet (TAG, $Tb_3Al_5O_{12}$) powders, as discussed in Chapter 3, were prepared by sol gel technique followed by sintering in air at various temperatures (1100^oC maximum) using a temperature controlled ($\pm1^oC$) home-made muffle furnace (Chapter 3).The doping concentrations investigated were 0.1, 0.5 and 1.0 mol%.; six powder samples were prepared by permuting of theses concentrations. The samples thus prepared were characterized by XRD, SEM and TEM), EDX, FTIR, Raman spectroscopy and photoluminescence (PL) techniques.

4.2 Results and discussion

4.2.1 EDX

Typical EDX spectrum of TAG co-doped with (sintered at 110^oC) 0.5 mol% of Ce and Eu is shown in Fig 4.1. As seen in Fig 4.1, peaks due to Eu and Ce are prominently observed along with those of Tb and Al confirming the incorporation of the dopants in

TAG lattice. The peak due to Au is because of the gold sample holder used for recording the EDX spectrum. Similar spectra were recorded for the other dopant combinations.

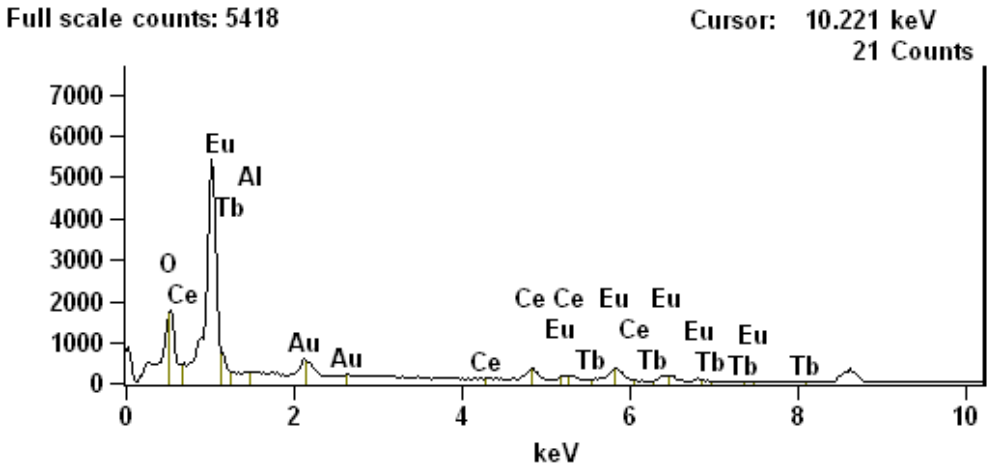

Fig 4.1: EDX spectra of TAG co-doped with 0.5 mol% of Ce and Eu

4.2.2 SEM/TEM images

The nanostructure nature of the synthesized powder samples was investigated by SEM and TEM techniques. Typical SEM image is shown in Fig 4.2a while Fig 4.2b shows a typical TEM image.

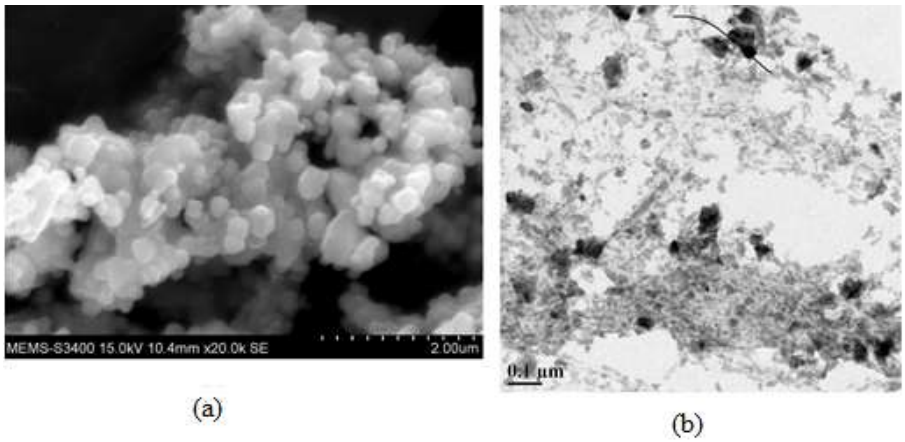

Fig 4.2: (a) Typical SEM image (b) typical TEM image of TAG powder sample co-doped with 0.5mol% Ce and Eu sintered at 1100^{o}C

Nanostructure nature of the powder samples of TAG co-doped with 0.5mol% Ce and Eu is clearly seen in the SEM and TEM images. Also, from the SEM image (Fig 4.2a), it can

be concluded that the synthesized powder sample was composed of spherically-shaped particles along with some non-spherical large sized grains which could be due to agglomeration and/or strain induced by Ce and Eu doping. The spherical nature of the particles of the synthesized powder is further supported from the TEM images where spherical particles are clearly visible. Similar images were observed with other dopant combinations.

4.2.3 FTIR

Typical FTIR spectra of TAG co-doped with Ce (0.1, 0.5 and 1.0mol%, variable) and Eu (0.1mol%, constant) are shown in Fig 4.3.; FTIR spectra of TAG are shown in this figure for comparison. All the samples were sintered at 1100^{o}C. As discussed in Chapter 3, the FTIR spectra were recorded in air using a KBr pallet. The observed absorption at 437, 680, 728 and 785 cm^{-1} could be due to Tb-O, Ce-O and Eu-O bonds while relatively broad absorption at 3450cm^{-1} which is typical of O-H functional group could be due to water present in air. Similarly, 1380 and 1640 cm^{-1} absorption which is typical of C-O functional group, could be attributed to CO_2 present in air. The main spectral features of all the spectra shown in Fig 4.3 are almost identical implying that the basic structure of TAG did not changing on Co-doping with Ce and Eu.

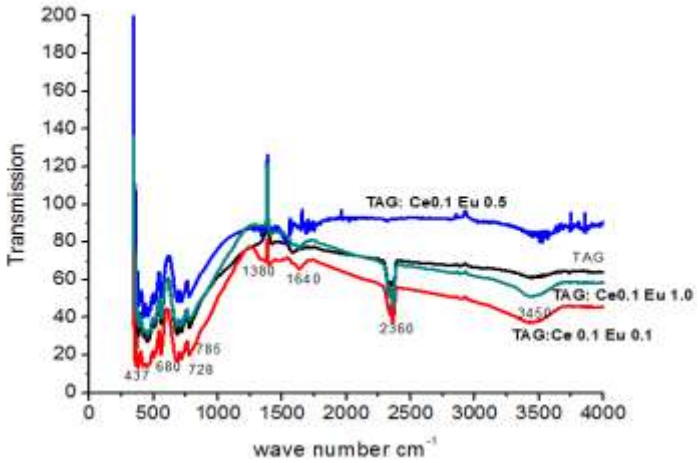

Fig 4.3: FTIR spectra of TAG co-doped with Ce (0.1, 0.5 and 1.0mol% , variable) and Eu (0.1mol%, constant).

Spectral features similar to Fig 4.3 were observed for TAGco-doped with Eu (0.1, 0.5 and 1.0mol%, variable) and Ce (0.1mol%, constant) as well as for TAG co-doped with 0.5mol% Ce and Eu.

4.2.4 XRD

Typical powder XRD spectra as a function of sintering temperature is shown in Fig 4.4 which displays the XRD spectra of TAG co-doped with 0.1mol%Ce and 0.5mol%Eu sintered at 150, 300,900 and 1100^{o}C; XRD spectrum of TAG sintered at 1100^{o}C is shown for comparison.

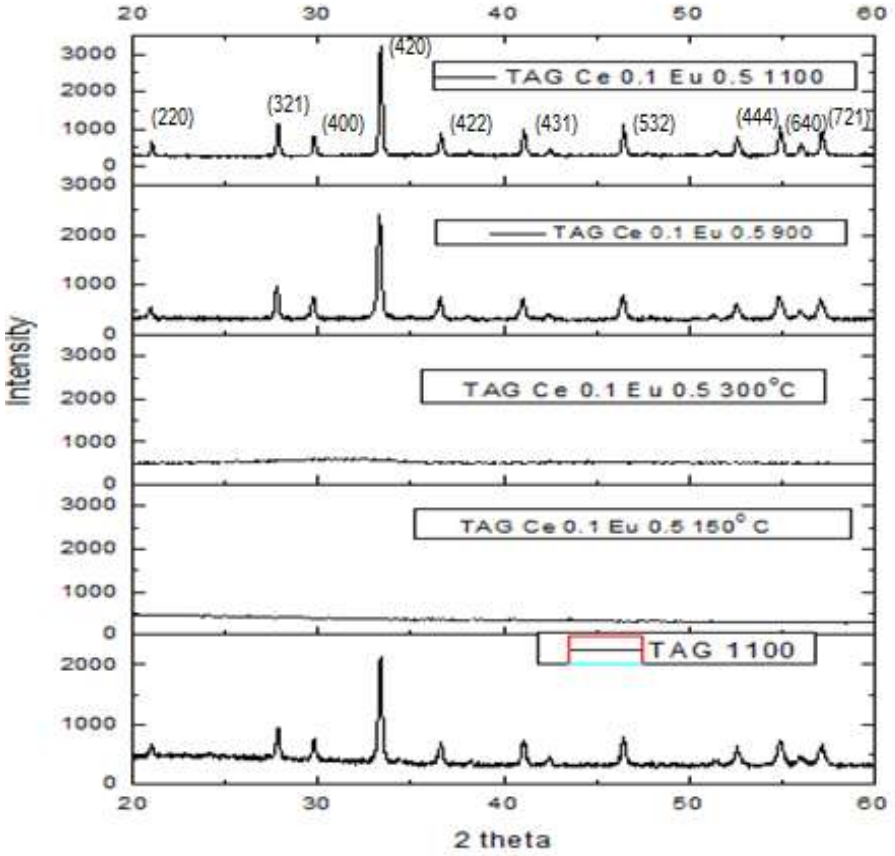

Fig 4.4: Typical powder XRD spectra of TAG co-doped with 0.1mol%Ce and 0.5mol% Eu sintered at 150, 300, 900, 1100^{o}C; XRD spectra of TAG sintered at 1100^{o}C is shown for comparison

As seen in this figure, the prepared material was amorphous in nature at 150^{o}C, developed some crystallinities at 300^{o}C which further improved at higher sintering temperatures. The narrowing of diffraction peaks with the increase in sintering temperature is summarized in Table 4.1. As seen in this table, full width at half maximum (FWHM) of the diffraction peak with (hkl) values (420) of TAG powder (co-doped with Ce 0.1mol% and Eu 0.5mol%) sintered at 900^{o}C almost doubles when the sintering temperature was increased to 1100^{o}C. This is well known phenomena (Chapter 3) observed in solids mainly due to agglomeration. The crystallite size calculated using the Scherrer formula (Eq. 4.1) also reflects the phenomena of the increase of FWHM of the diffraction peaks with increase in sintering temperature.

Table 4.1: Average crystallite size of the TAG co-doped with 0.1 mol% Ce and 0.5 mol% as a function of sintering temperature,

S.No.	Sample (mol%)	2 theta (degrees) (420)	FWHM (degrees)	Crystallite size (nm)
1.	TAG :Ce 0.1 Eu 0.5 sintered at 900^{0}C	33.3	0.25	35
2.	TAG : Ce 0.1 Eu 0.5 sintered at 1100^{0}C	33.3	0.13	67

The Scherrer formula is shown as follows:

$$D = k\lambda/B\cos\theta \qquad (4.1)$$

Where D is mean crystalline size in nm, k is a dimensionless constant usually taken as 0.9, λ is the wavelength (nm) of the X-ray radiation used to record the diffraction pattern, B is full width at half maximum (rad) of any peak in XRD pattern and θ is the angle (in degrees) between the incident and diffracted beams.

The powder XRD spectra of ZnO co-doped with 0.1mol% constant) of Ce and 0.1, 0.5 and 1.0mol% (variable) of Eu along with that of TAG are shown in Fig 4.5; all the samples were sintered at 1100^{o}C. All the peaks of the spectra shown in this figure were

indexed by JCPDS 17-035 implying that the co-doping levels used in the present study did not change the basic structure of the host. Also, the XRD data did not show any independent phase of Ce or Eu indicating the doping of the both in TAG. Similar results were observed for ZnO co-doped with Ce (0.1, 0.5 and 1.0mol%, variable) and Eu (0.1mol%, constant) as well as for ZnO co-doped with 0.5mol% Ce and Eu.

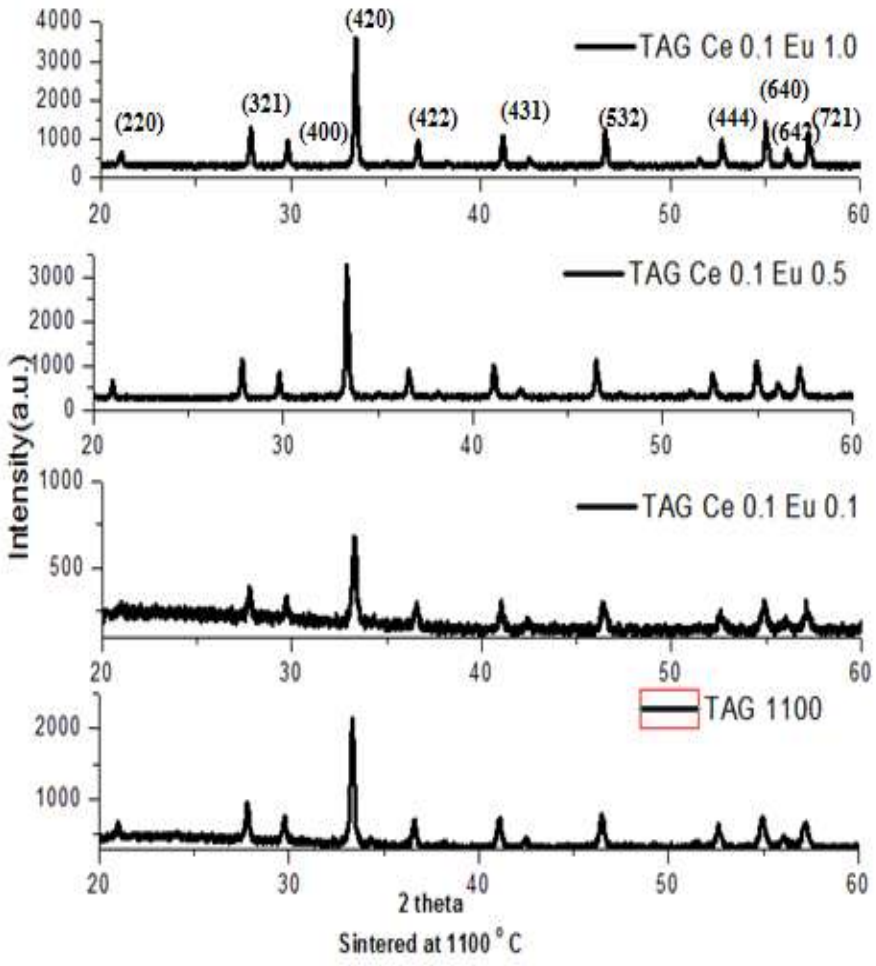

Fig 4.5: Powder XRD spectra of TAG co-doped with 0.1mol% constant) of Ce and 0.1, 0.5 and 1.0mol% (variable) of Eu

Dopants on entering any lattice introduce distortions resulting in development of lattice strain which can be calculated from XRD data (Chapter 1). This induced lattice strain is reflected in the change in the line width and the peak position of the diffraction peaks,

crystallite size, lattice constants and unit cell volume. Table 4.2 summarizes the changes in the peak position and line width of the diffraction peak (420) as a function of the dopant concentration; line width changes are also reflected in the variation of crystallite as evident from Scherrer formula (Eq. 4.1).

Table 4.2 : Dopant concentration dependence of FWHM, crystallite size and lattice strain of ZnO co-doped with Ce and Eu for the diffraction peak (420)

Sample sintered at 1100^{o}C	2 theta (degree)	FWHM (nm)	Crystallite size (nm)	Lattice strain
TAG	33.33	0.22	39.	0.0032
TAG : Ce 0.1 Eu 0.1	33.31	0.37	23	0.0054
TAG : Ce 0.1 Eu 0.5	33.35	0.13	67	0.0019
TAG : Ce 0.1 Eu 1.0	33.38	0.19	45	0.0028
TAG : Ce 0.5 Eu 0.5	33.11	0.44	20	0.0065
TAG : Ce 1.0 Eu 0.1	33.36	0.21	41	0.0031

As seen in Table 4.2, TAG co-doped with 0.5 mol% Ce and Eu experienced maximum shift (~0.22^{o}) compared to that of TAG where the diffraction peak (420) was observed at 33.33^{o}. This shift is almost zero for ZnO co-doped with 0.1mol% Ce while keeping the Eu concentration constant at 0.5mol%. On increasing the Ce concentration to 1.0mol% while keeping Eu concentration as 0.1mol%, the shift is still almost zero implying that 0.5mol% Ce and Eu when co-doped in TAG induces a maximum distortion resulting in maximum lattice strain as seen in the last column of Table 4.2. Broadening of the diffraction peaks resulting in the decrease in the crystallite size also reflects the amount of distortion induced in a lattice by dopants. The line width of (420) diffraction peak is maximum (0.44nm) for 0.5mol% doped TAG while it is 0.37nm for 0.1mol% Ce and Eu co-dopants. This line width is minimum (0.13nm) for TAG: Ce 0.1, Eu 0.5 while for TAG and TAG: Ce 1.0 Eu 0.1, it is almost the same (~22nm). Consequently, the calculated crystallite size (Scherrer formula) is minimum for TAG: Ce 0.5, Eu 0.5 and maximum for TAG: Ce 0.1,Eu 0.5. Fig 4.6 compares the XRD spectra of TAG single

doped with 0.5mol% of Ce and Eu with that of TAG co-doped with 0.5mol% of Ce and Eu. The parameters like peak position, FWHM, crystallite size and estimated strain for the diffraction peak (420) calculated from the analysis of the spectra shown in Fig 4.6 are summarized in Table 4.2

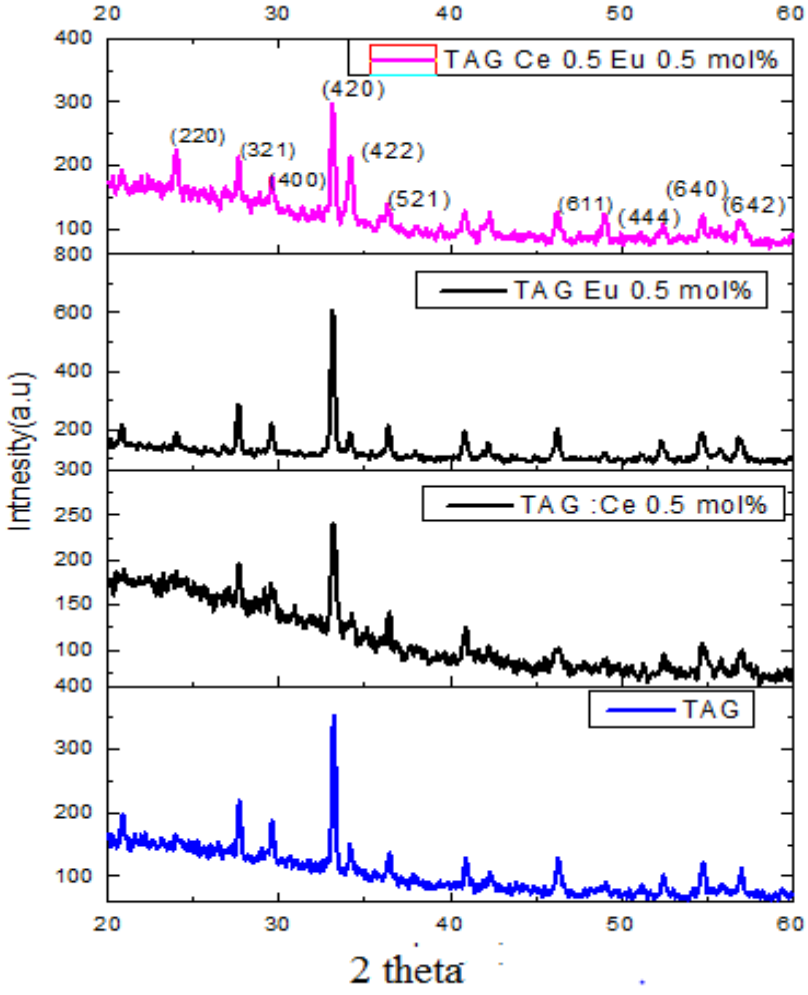

Fig 4.6: Comparison of the XRD spectra of TAG single doped with 0.5 mol% of Ce and Eu with that of TAG co-doped with 0.5 mol% of Ce and Eu.

All the XRD spectra shown in Fig 4.6 were indexed with the help of JCPDS 17-035, the primary XRD data file for TAG implying that basic structure, as concluded earlier, did not change on doping concentrations used in the present study. However, parameters like the peak position of the diffraction peaks as well as their line width changes with nature of the dopant. As mentioned in Table 4.3, peak position of the most prominent diffraction peak (420) is ~33.33^{o} for TAG while it is the almost same (33.36^{o}) for TAG: Ce

(0.5mol%) indicating that Ce doping which likely could be substituted at Tb site in TAG did not induce any significant amount of distortion in TAG lattice; this is further supported by the calculated lattice strain induced in TAG lattice on Ce doping (Table 4.2)

Table 4.3: Comparison of the peak position, FWHM, crystallite size and lattice strain of the diffraction peak (420) of TAG single doped with 0.5mol% Ce and Eu with that of TAG co-doped with 0.5mol% of Ce and Eu.

Sample sintered at 1100^{o}C (mol%)	2 theta degree	FWHM (nm)	Crystallite size (nm)
TAG	33.33	0.22	40
TAG : Ce 0.5	33.36	0.92	9
TAG : Eu 0.5	33.13	0.28	31
TAG : Ce 0.5 Eu 0.5	33.11	0.44	20

On the other hand, in TAG:Eu (0.5mol%) the peak position of (420) diffraction peak shifted value by ~0.20^{o} towards lower angle implying the significant induction of lattice distortion by 0.5mol% doping of Eu in TAG. The observed shift for TAG: Ce (0.5mol%), Eu (0.5mol%) increase marginally compared to TAG: Eu (0.5mol%) implying that major distortion in TAG is induced on Eu doping.

The variation of the line width of the diffraction peak with dopant nature and its concentration, as seen in Table 4.3 is interesting. The observed FWHM for TAG was about 0.22 nm where it increased to ~97nm when 0.5mol% Ce was doped in it. This could not be attributed to the lattice distortion induced by Ce doping as no shift, as mentioned earlier, in diffraction peak position (Table 4.3) was observed. Only possible mechanism of this increase in line width on Ce doping could be due to decrease in crystallinity of TAG on Ce doping.

Hence, it could be concluded that Ce doping resulted in decrease in the degree of crystallinity of the host TAG while Eu doping induced significant amount of distortion in its (TAG) lattice. On co-doping with Ce and Eu, the TAG lattice experienced almost the same distortion as that of single doped Eu yet the degree of crystallinity improved

significantly compared to that of single doped Ce. This could prove useful for realization of white light source.

The ionic radius of Ce^{3+} is 101*pm* while it is 93*pm* and 97*pm* for Tb^{3+} and Eu^{3+} respectively. Since the ionic radius of Tb is very close to that of Eu while it is smaller in comparison of that of Ce. It will be expected that Ce doping could introduce more lattice distortion compared to Eu while XRD analysis show the opposite; lattice distortion induced by Eu is more than that of Ce which resulted in lesser degree of crystallinity in doped TAG powder sample.

4.2.5 Raman scattering

Typical Raman spectra of TAG and TAG: Ce (0.1mol%), Eu (0.5mol%) is shown in Fig 4.7

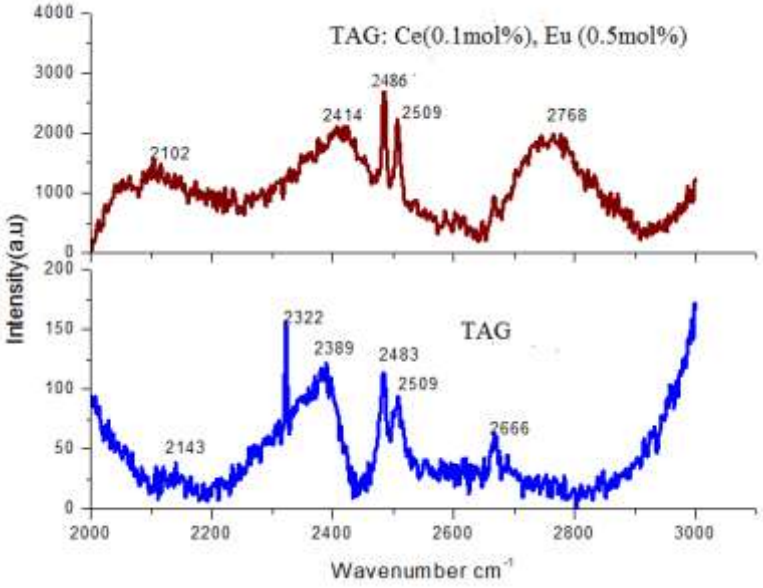

Fig 4.7: Typical room temperature Raman spectra of TAG and TAG: Ce 0.1 mol%, Eu 0.5 mol%

As seen in Fig 4.7, Raman shifts at 2143, 2322,2389,2483,2509 and 2666 cm^{-1}were observed in TAG when excited with 514.5nm radiation from an Ar-ion laser. On doping with 0.1mol% of Ce and 0.5mol% of Eu, the peak position of the Raman shift at 2509cm^{-}

[1] did not change while it changed by ~3cm^{-1} in case of 2483 cm^{-1} shift. On the other hand, the shifts observed in TAG at 2143, 2322, 2389 and 2666cm^{-1} were not observed in TAG: Ce 0.1mol%, Eu 0.5mol%; new shifts at 2102, 2414 and 2768 cm^{-1} were observed. In TAG, Raman shifts are attributed to the electron Raman of the Tb^{+3} while in doped TAG, there could be contribution from Ce and Eu. However, with present data, the assignment is not possible; it needs more detailed investigation which is beyond the scope of this investigation. In the present study, characterization of the samples by Raman scattering was taken up to assess the extent of induced lattice distortion on co-doping of Ce and Eu in TAG, Fig 4.8 shows the shift in the peak position of the Raman shift at 2483cm-1 which is found both in TAG as well as co-doped samples.

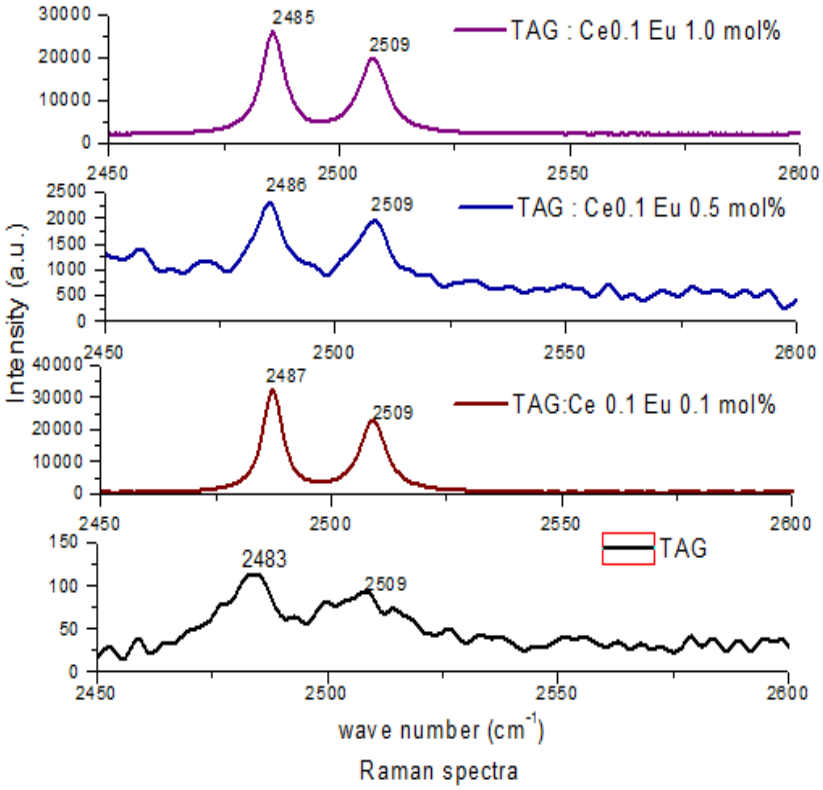

Fig 4.8: Raman shift in the peak position of 2483 cm^{-1} in Raman spectra as a function of dopant concentration.

As seen in Fig 4.8, the peak position of the Raman shift at 2509cm^{-1} did not change with the change in the dopant concentration while the other shift at 2483 cm^{-1} changed by

~4cm^{-1} when TAG was co-doped with 0.1mol% of Ce and Eu. However, this shift was almost constant with the increase in the Eu concentration keeping the Ce concentration constant at 0.1mol%. However, the intensity showed interesting variation (Fig 4.9) where integrated intensity area (arbitrary units) of the Raman shift at 2483 cm^{-1} has been plotted as a function of varying ((0.1,0.5 and 1.0mol%)Eu concentration while keeping the Ce concentration constant at 0.1 mol %. As seen in this figure, the intensity of this Raman shift changed almost by two orders of magnitude when TAG was co-doped with 0.1mol% of Ce and Eu. However, the intensity reduced almost by one order of magnitude when Eu concentration was increased to 0,5mol% keeping Ce concentration at 0.1mol% while the intensity again changed by one order of magnitude when Eu concentration was increased to 1.0mol% without changing the concentration of Ce which was kept constant at 0.1mol%. The change in the intensity with 0.1mol% co-doping of Ce and Eu shows the distortion induced in the TAG lattice due to doping as Raman scattering is very sensitive to lattice distortion; this distortion is also reflected in the shifting of the peak position of 2483 cm^{-1} Raman shift (Fig 4.8). The subsequent variation in intensity could be due to surface migration of the Eu with increase in its concentration.

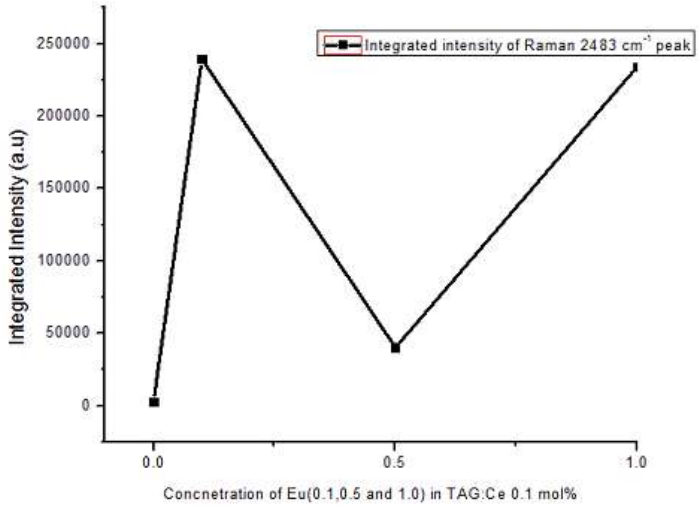

Fig 4.9: Intensity variation of the 2483 cm^{-1} Raman shift as a function of Eu concentration; the concentration of Ce was constant at 0.1mol%

Similar type of behavior was observed with TAG doped with Ce (0.1,0.5 and 1.0mol%, variable) keeping Eu concentration constant at 0.1mol%

4.2.6 UV-VIS absorption

UV-VIS absorption spectra of TAG co-doped with Ce (0.1, 0.5 and 1.0 mol%, variable) and Eu (0.1mol%, constant) are shown in Fig 4.10.

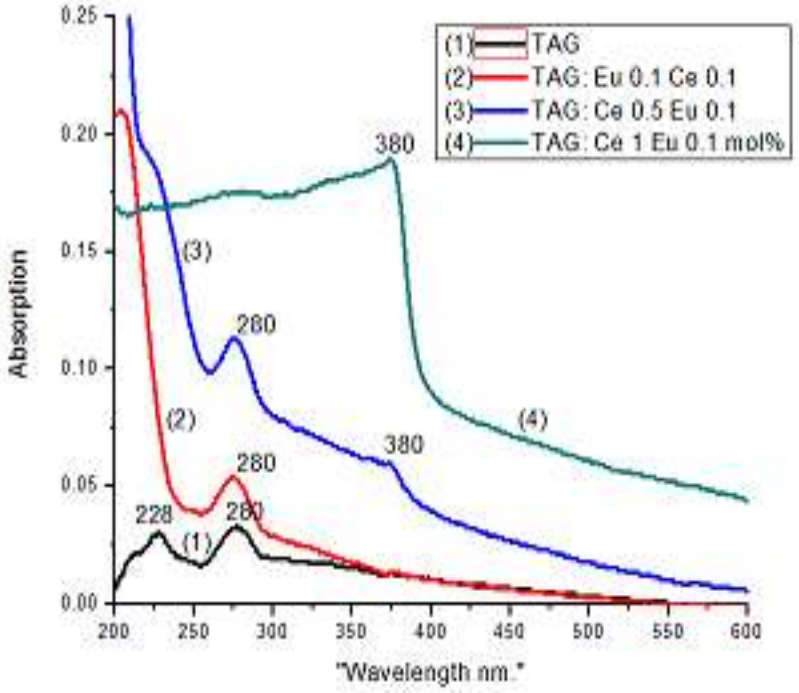

Fig 4.10: UV-VIS absorption spectra of TAG co-doped with Ce (0.1, 0.5 and 1.0 mol%, variable) and Eu (0.1mol%, constant)

TAG, as seen in Fig 4.10, has two absorption peaks: one at 228 and other at 280nm; 280nm could be due to Tb^{3+}. It has almost zero absorption at 550nm. On co-doping with 0.1 mol% Ce and Eu its (TAG) absorption in UV region (200-250nm) increased by a factor of ~5; also the intensity of the absorption peak at 280nm increased marginally while showing almost zero absorption at 550nm. On the other hand, when Ce concentration was further increased to 0.5mol% keeping the concentration of Eu constant at 0.1mol% very significant increase in absorption in 200-350nm region was observed;

also additional absorption peak at 380nm was observed. This 380nm absorption peak could be due to 4f-5d transition of Ce. In case of the TAG co-doped with Ce 1.0mol% and Eu 0.1mol%, as seen in Fig. 4.10, the absorption was almost uniform in the spectral region 200-350nm, peaks ~380 after which it decreased sharply till ~400nm and then decreased slowly; the absorption was significant even at 600nm. This observed absorption could be due to 4f-5d transitions of Ce.

Fig 4.11 shows the UV-VIS absorption spectra of TAG co-doped with Eu (0.1, 0.5 and 1.0 mol%, variable) and Ce (0.1mol%, constant)

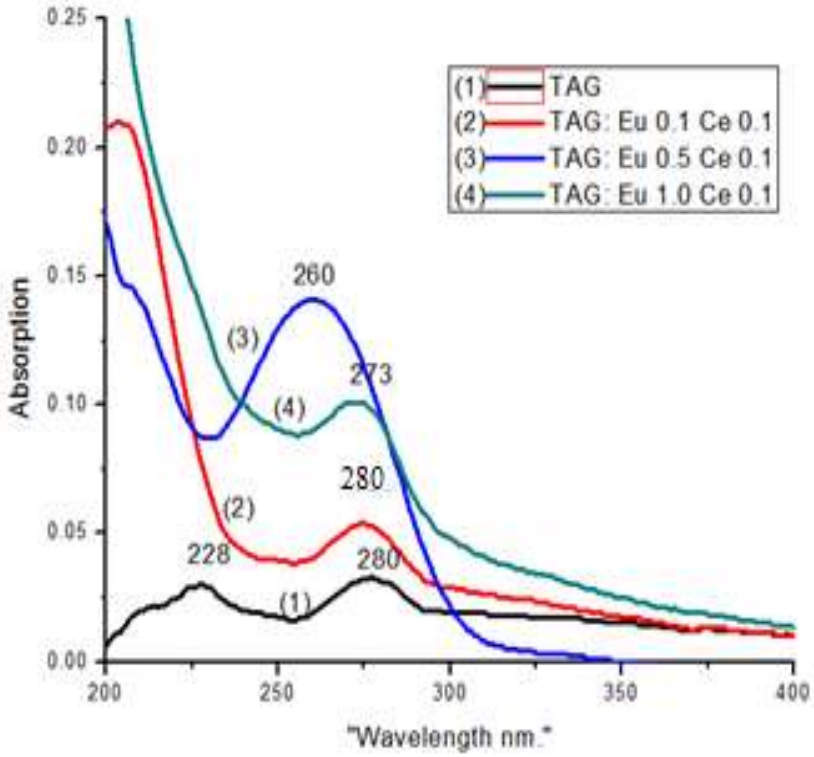

Fig 4.11: UV-VIS absorption spectra of TAG co-doped with Eu (0.1, 0.5 and 1.0 mol%, variable) and Ce (0.1mol%, constant)

TAG when doped with Ce 0.1mol% and Eu 0.5mol%, as seen in Fig 4.11 showed broad absorption in 225-300nm range with peak at 260nm; this is characteristic Eu absorption. However, a decrease in absorption in 225-300nm region where the peak shifted to 273nm

when Eu concentration was increased to 1.0mol% implying the migration of Eu to surface at higher concentration as concluded from Raman studies discussed in earlier section.

4.2.7 Photoluminescence (PL)

Fig 4.12 shows 280nm excited PL spectra of TAG co-doped with Ce and Eu; the spectra of single doped Ce and Eu and that of undoped TAG has been shown for comparison.

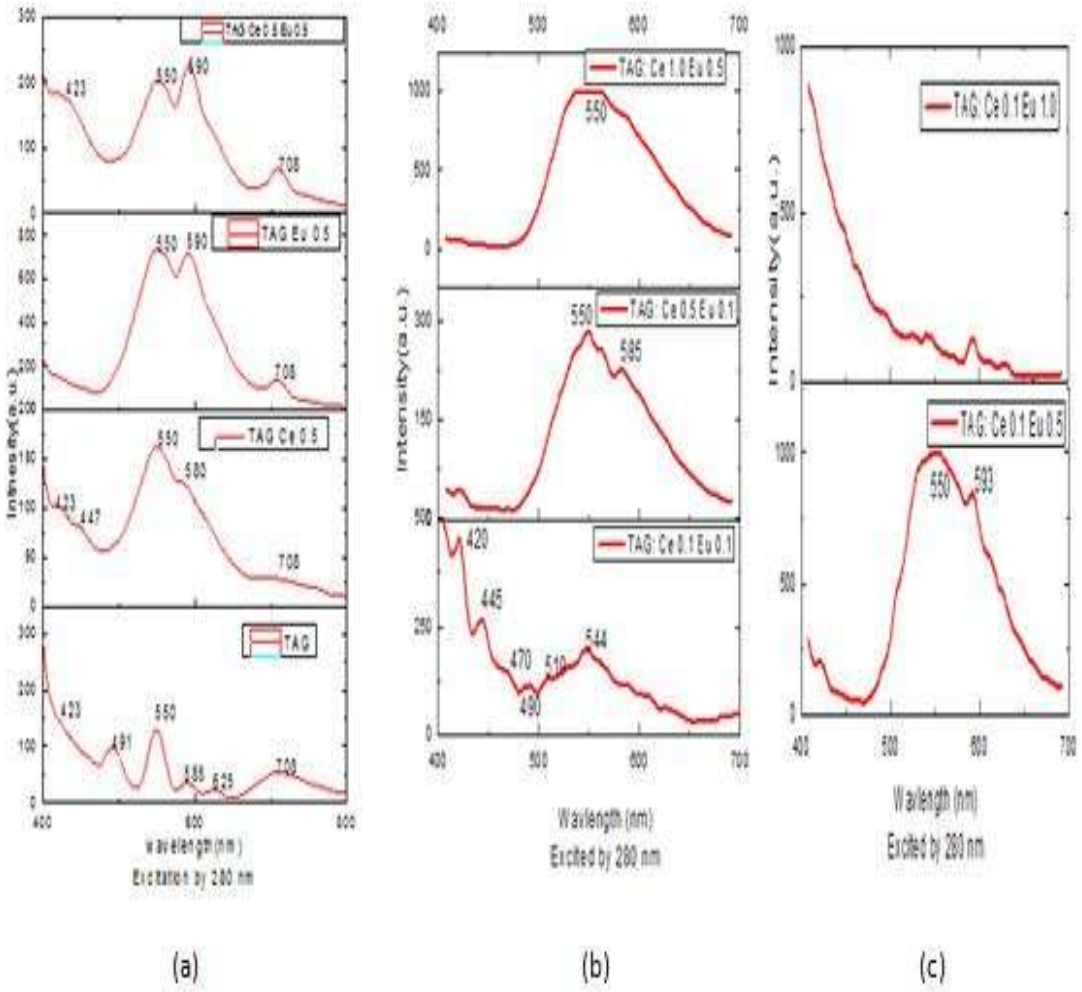

Fig 4.12: 280nm excited PL for Ce and Eu co-doped in TAG; spectra of single doped Ce and Eu TAG and that of un-doped TAG is shown for comparison.

The PL of un-doped TAG, as seen in Fig 4.12, consists of well-defined peaks in the visible regions which could be due to Tb^{3+}.Relatively broad emission superimposed with a few peaks was observed when TAG was doped with 0.5mol% Ce. This broad emission could be due to 5d-4f emission of Ce while the superimposed peaks could be due to Tb present in TAG. Similar broad emission was observed with TAG;Eu (0.5 mol%) as well as in TAG co doped with 0.5 mol% of both Ce and Eu. Emission lines from Tb are dominating in almost all the spectra except that of TAG co-doped with 0.1mol% Ce and 1.0mol% Eu where intensity falls sharply in 400-500nm region while Tb can be seen in 500-700nm region. This could be due to concentration quenching by Eu and has strong absorption in 400-500nm region. The variation in the intensity of the observed emission is shown in Fig 4.13a and Fig 4.13b where integrated area (arbitrary units; au) of the emission spectrum have been plotted as a function of the dopant concentration.

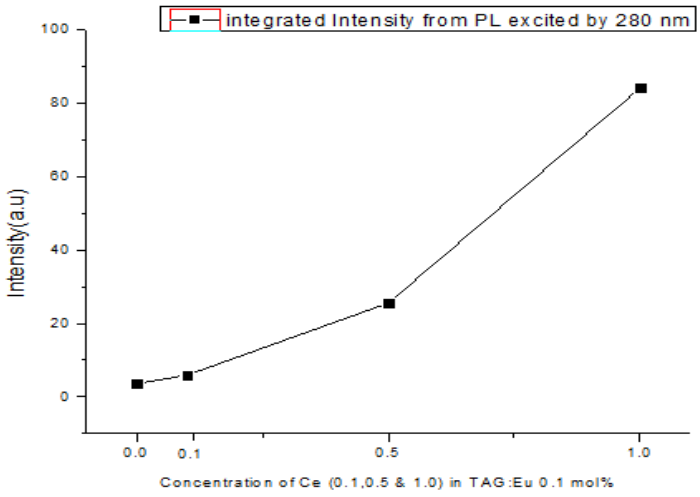

Fig 4.13a: Integrated area (arbitrary units, au) of the emission spectrum of the TAG co-doped with Ce (0.1, 0.5 and 1.0 mol%, variable) and Eu (0.1mol%, constant).

The intensity of the emission in the visible region, as seen in Fig. 4.13a, increases significantly with the increase in the concentration of Ce keeping Eu concentration constant at 0.1mol%. On the other hand, in case of the TAG co-doped Eu (0.1, 0.5 and 1.0 mol%, variable) and Ce (0.1mol% constant), the intensity is maximum for 0.5mol%

of Eu which decreases sharply when Eu concentration is increased to 1,0 mol% (Fig 4.13b). This decrease with the increase in Eu concentration could be due to "concentration quenching" and/ or due to increased distortion induced by Eu as discussed while analyzing the XRD data.

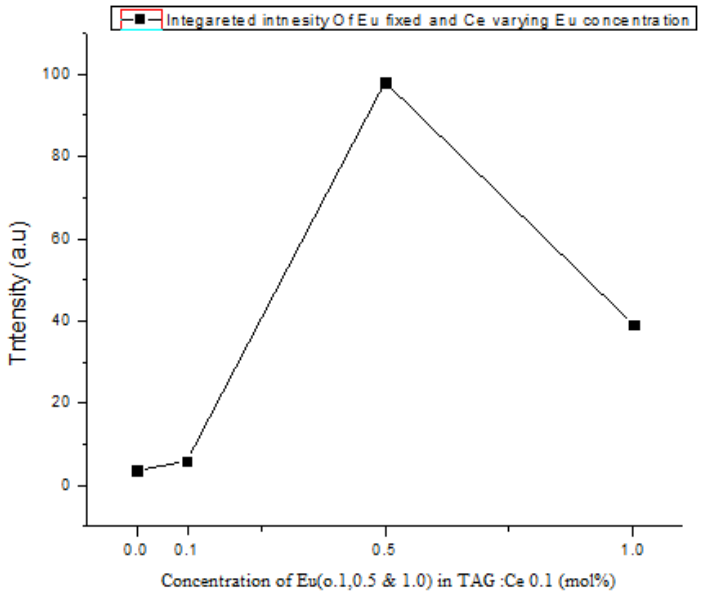

Fig 4.13b: Integrated area (arbitrary units, au) of the emission spectrum of the TAG co-doped with Eu (0.1, 0.5 and 1.0 mol%, variable) and Ce (0.1mol%, constant)

The suitability of any phosphorescent material, as discussed in Chapter 1, is assessed by calculating the chromaticity color coordinates of its emission in visible region. Table 4.4 summarizes these coordinates calculated for the visible emission (Fig 4.12) observed from TAG co-doped with Ce and Eu.

TAG co-doped with 0.5mol% of both Ce and Eu, as seen in Table 4.4, emits in visible region which has characteristics of "day light" indicating its utility in the realization of white light sources, its chromaticity color coordinates x=0.35 and y=0.35 along with CCT= 4812K are very close to that of an ideal white light source which should have x=0.33 and y= 0.33 with CCT= ~5000K. On the other hand, the other materials listed in this table do emit blue-purple or blue-green shades and can be used for the fabrication of colored light sources. However, its color rendering index (Chapter1) need to be investigated to realize its full potential.

Table 4.4: Summary of CIE and CCT parmeters for TAG and TAG co-doped with Ce and Eu

Sample	CIE co-ordinate (x,y)	CCT (K)	Characteristic color
TAG: Ce0.1 Eu 0.1	0.29,0.30	8346	Summer shade
TAG: Ce0.5 Eu 0.1	0.27,0.28	12849	Blue Purple
TAG: Ce 1.0 Eu 0.1	0.28,0.29	9869	Blue green
TAG: Ce0.1 Eu 0.5	0.27,0.27	12793	Blue Purple
TAG :Ce0.5 Eu 0.5	0.35,0.35	4812	Day light

The CIE diagram for TAG: Ce 0.5Eu 0.5 is shown in Fig 4.14.

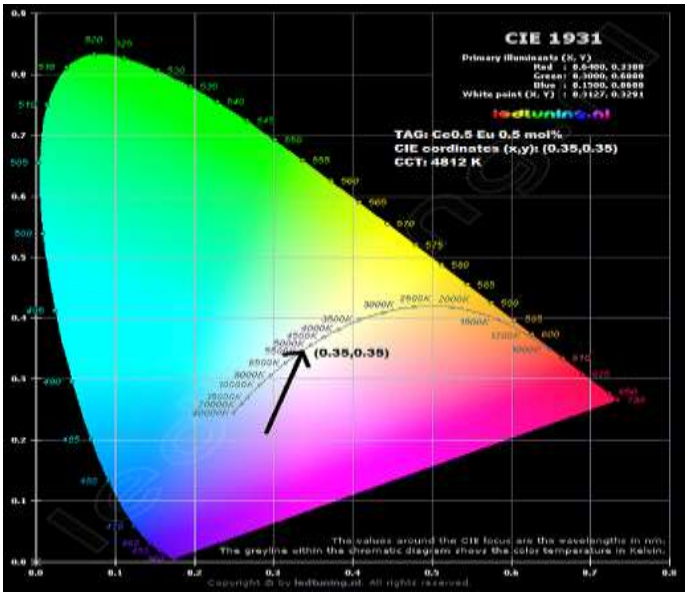

Fig 4.14: CIE diagram of TAG co-doped with 0.5mol% of Ce and Eu

As seen in Fig 4.14 the emission falls very well in the white light region of the CIE diagram.

REFERENCES

[1] Ganschow et al.(1999) *Crystal Research and Technology* 34 :615-619.

[2] Saxena S, A Asokkumar K and Lal B (2007) *J Sol-Gel Sci Techn* 41: 245-248

[3] Shabir H, Lal B and Rafat M (2010) *Ceram. Int.* 36:365-369

[4] Shabir H, Lal B and Rafat M(2010) *J Sol-Gel Sci Techn* 53:399–404

[5] Chang C C, Tsai M S and Hen M H (2007) *J Alloys Compd.* 431:298-302

[6] Dotsenko et al (2013) *J Alloys Compd.* 550:150-163

[7] Batentschuk et al (2004) *Radiat. Meas* 38: 539-543

CHAPTER 5

SINGLE DOPED Ce, Eu, Gd AND Tb IN ZnO NANO PHOSPHOR

5.1 Introduction

Investigation on the rare-earth doped ZnO has attracted lot of attention mainly because of the tailoring of the visible emission from ZnO by doping. The visible emission being from the defect states, the extent of the lattice distortion induced by the dopant results in the tailoring of the emission. Ce, for example, reduced the length of the lattice constants along with decrease in the emission intensity [1-5] while the decrease in the emission intensity on Eu doping was due to well-known concentration quenching [6-13]. An increase in emission intensity was observed on Gd doping [14] while hydrostatic like pressure was observed with Tb doping [15-17].However; there is detailed investigation on the properties of the visible emission when excited by various excitation radiations. In the present study, nano powders singly doped with Gd, Tb, Ce and Eu were prepared by precipitation method, discussed in detail in Chapter 3. The doping concentrations investigated were 0.1, 0.5 and 1.0mol%. All the powder samples were characterized by EDX, XRD, SEM, FTIR and optical spectroscopy techniques. Chromaticity color coordinates of the emission in the visible range were calculated to assess the potential of these materials for the realization of white light sources.

5.2 Results and Discussion

5.2.1 EDX

EDX technique was employed to confirm the doping of the rare-earths in ZnO. Typical EDX spectra of ZnO: Gd and ZnO: Tb are shown in Fig 5.1. As seen in Fig 5.1 (a) and (b) Gd and Tb peaks are prominently seen along with those of Zn and O confirming the incorporation of these elements in ZnO lattice. Au impurity can be seen in both the spectra as gold sample holder was used for recording the EDX spectra. Similar results were observed in case of ZnO: Ce and ZnO: Eu.

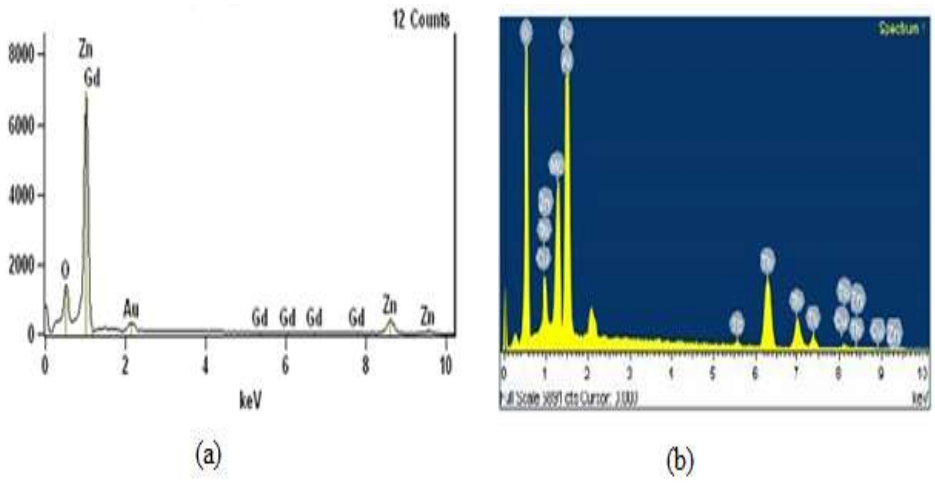

Fig 5.1: EDX spectra of (a) ZnO: Gd and (b) ZnO: Tb

5.2.2 SEM images

SEM images of the powder samples were recorded to investigate the morphology of the prepared samples. Typical SEM images of ZnO: Gd and ZnO: Tb are shown in Fig 5.2. The powder samples of ZnO doped Gd and Tb, as seen in Fig5.2, were composed of spherically shaped particles along with some non-spherical large sized grains which could be due to agglomeration and/or strain induced by Gd/Tb doping as discussed in following sections. Similar images were recorded with ZnO powder samples singly doped with Ce and Eu.

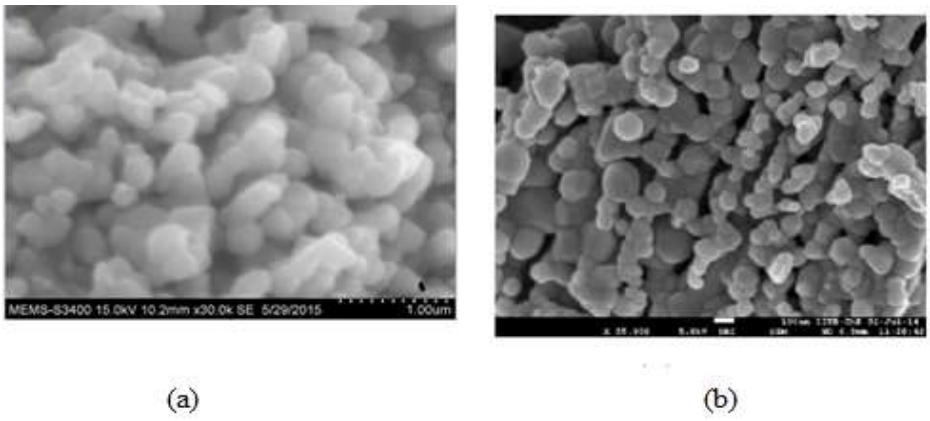

Fig 5.2: SEM images of ZnO: Gd (0.5mol %) and ZnO: Tb (0.5mol %) powder samples sintered at 700^{o}C

5.2.3 FTIR

FTIR spectroscopy was used to investigate the change, if any, in the structure of ZnO on doping with rare-earths; typical FTIR spectra of ZnO: Ce and ZnO: Eu in 400-4000cm^{-1} range recorded in air using KBr pallet are shown in Fig 5.3.

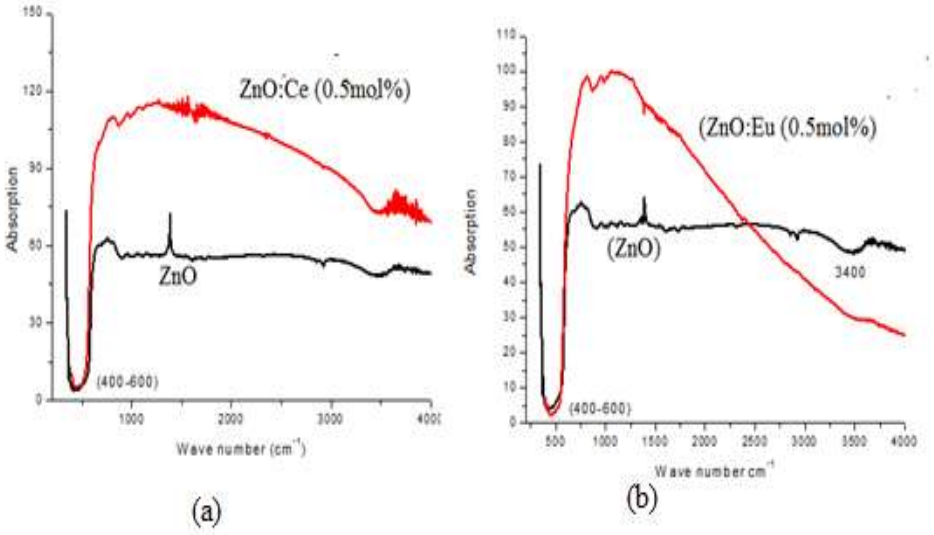

Fig 5.3: Typical FTIR spectra of powder samples of ZnO, ZnO: Ce and ZnO: Eu. All the samples were sintered at 700^{o}C

All the main spectral features, as seen in Fig 5.3, of the FTIR spectra of ZnO, ZnO: Ce and ZnO: Eu are similar implying that the basic structure of ZnO did not change on doping.The absorption peak in 400-600cm^{-1}region are due to metal oxygen bonds (Zn-O, Ce-O/Eu-O) vibrations while relatively weak absorption at 3500 cm^{-1} is due to water present in atmosphere. Similar results were seen in the FTIR spectra of 0.1 and 1.0 mol% doped samples for all the dopants.

5.2.4 XRD analysis

Powder XRD data analysis was carried out in detail to investigate the effect of doping on the XRD spectra, bond lengths, crystallite sizes and unit cell volume. Typical XRD spectra are shown in Fig. 5.4.

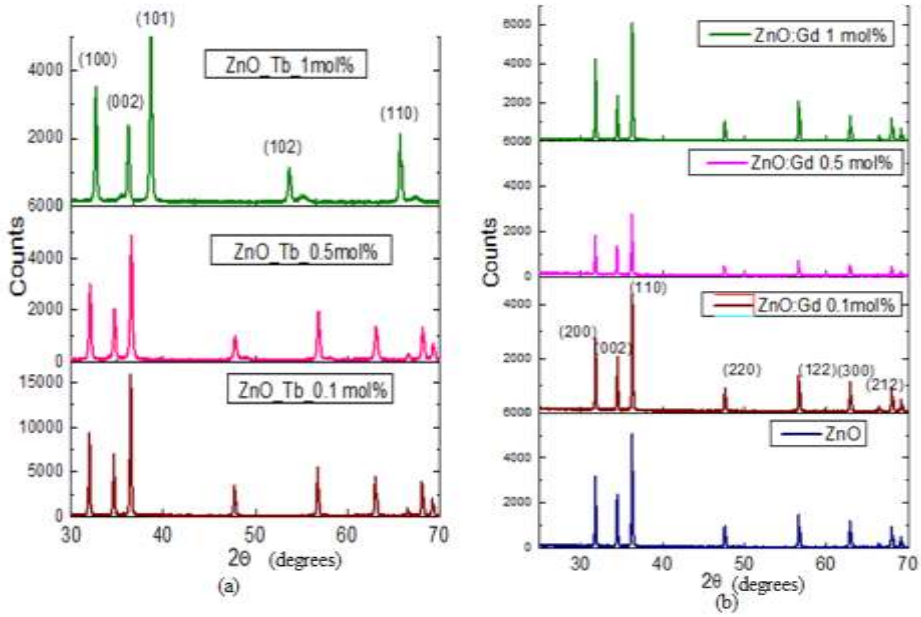

Fig 5.4: Typical room temperature powder XRD of ZnO, ZnO: Tb and ZnO: Gd

Typical room temperature powder XRD patterns of ZnO doped with 0.1, 0.5 and 1.0 mol% of Tb and Gd are shown in Fig 5.4. All the XRD patterns could be indexed using JCPDC file No. 36-1451 (primary XRD file of ZnO) confirming the wurtzite structure and implying that the doping levels investigated in the present study did not change the basic crystal structure of ZnO. Absence of any independent phase of Gd/Tb confirmed its incorporation in ZnO. Similar observations were made with Zn doped with Ce and Eu.

Fig 5.5 shows an example of the improvement in the degree of crystallinate with the increase in the sintering temperature; in this figure the XRD patterns of ZnO:Gd sintered at 150 , 300 and 700 ^{o}C are compared.

The results of this Fig 5.5 are summarized in Table 5.1 where integrated intensity in arbitary units and full width at half maximum (FWHM) of the diffraction peaks with (hkl) values (100), (002) and (101) of ZnO: Gd sintered at 150^{o}C has been compared with that of 700^{o}C sintered sample.

The integrated area of three diffraction peaks (Table I) with (hkl) values (100), (002) and (101) observed for the sample sintered at 150^{o}C almost doubles on increasing the

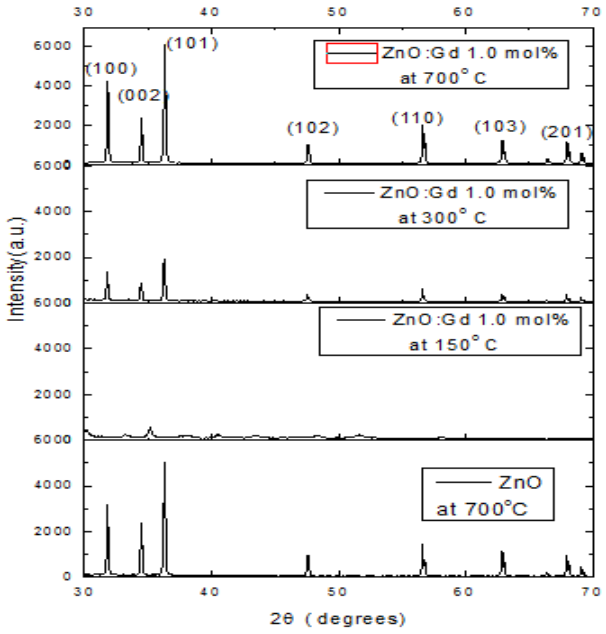

Fig 5.5: Powder XRD patterns of ZnO: Gd sintered at 150, 300 and 700°C.

Table 5.1: Comparison of the integrated area and the full-width at half maximum (FWHM) of the diffraction peaks

Diffraction Peak	Integrated Area(AU)		FWHM (deg)	
(hkl)	150°	700°	150°	700°
(100)	870	1607	0.23	0.16
(002)	665	1303	0.23	0.17
(101)	1601	3059	0.25	0.18

sintering temperature to 700°C which is attributed to improved crystallinity with the increase in sintering temperature. This improvement in degree of crystallinity with increase in sintering temperature is further confirmed from the decrease (~30%) in the FWHM of the diffraction peaks with increase in the sintering temperature. Similar results were obtained in case of ZnO doped with Tb, Ce and Eu.

5.2.4.1 Shifting of the XRD diffraction peaks

The wurtzite structure, as discussed earlier did not change on doping yet it resulted in the shifting of the peak positions of the XRD diffraction peaks as shown in Fig 5.6a where shift in the three diffraction peaks with (hkl) values (100), (002) and (101) of ZnO on doping with 0.5mol% Tb is shown; the peak positions of all the three peaks is shifted (towards the higher angle) by ~0.09 degree. This shift in peak position of the diffraction peaks was found to vary with the doping concentration of Tb as seen in Fig 5.6b. As seen in this figure, almost no shift is observable between the peak positions of the diffraction peaks of ZnO and ZnO; Tb (0.1mol%), it is maximum (~0.09 degree) when doped with 0.5 mol% Tb which is almost halved (~0.04 degree) when Tb doping concentration is doubled to 1.0mol%.

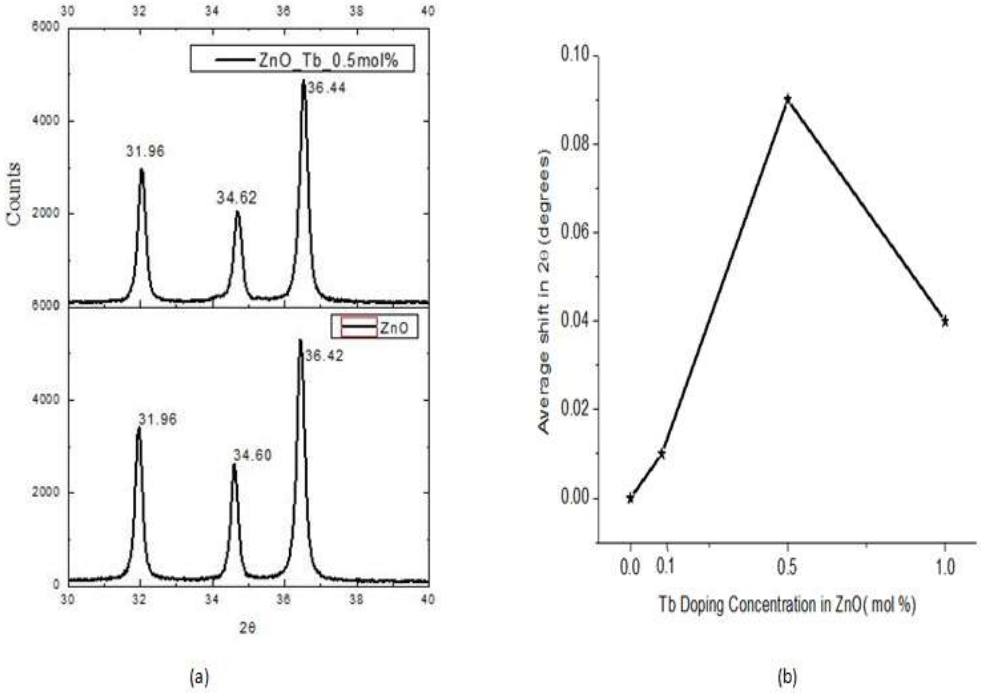

Fig 5.6: (a) Shift in the diffraction peaks of ZnO: Tb (0.5mol %) (b) Tb concentrate on dependence of the XRD peak shift for ZnO: Tb

On the hand, when ZnO was doped with 0.5mol% Ce and Eu the observed shift was about 0.14^{o} towards the lower angle implying the induction of lattice distortions of almost

equal magnitude on doping; however, the stress developed by the doping of Tb is in opposite direction to that of the stress developed on doping by Ce or Eu.

No significant shifiting of the peak positions of the diffraction peaks was observed when Gd was doped in ZnO.

5.2.4.2 Change in lattice constants and unit cell volume

Dopants in general induce lattice distortions in the host resulting in increase/decrease in lattice constants; consequently the volume of the unit cell also changes. Changes in the lattice constant "a" and "c" in ZnO: Tb are shown in Fig 5.7a while the Fig 5.7b shows the variation in unit cell volume as a function of Tb concentration.

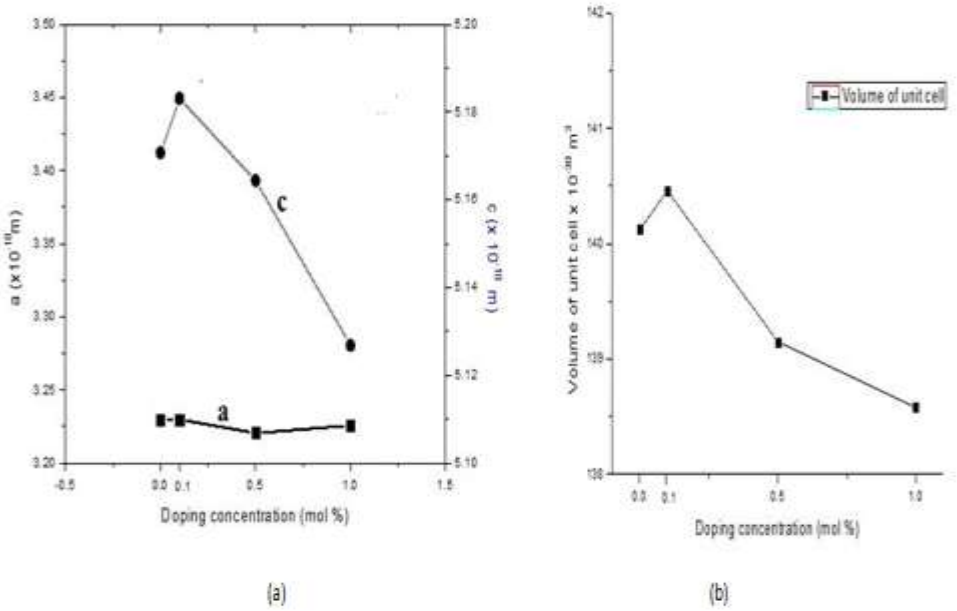

Fig 5.7: Variation of the (a) lattice constants "a" and "c" and (b) unit cell volume as function of Tb concentration in ZnO

The calculated values of "a & c" of ZnO were found to be: a=0.3230nm, c=0.5171Å (c/a=1.60) which are in reasonably good agreement with the values reported for wurtzite ZnO structure in the literature. As seen in Fig 5.7a the lattice constant "a" varies marginally with doping concentration. It is almost the same (0.3230nm) for ZnO: Tb (0.1mol %) while decreases marginally for other two (~0.3% for 0.5 and~0.1% for 1.0

mol %) doping concentrations. On the other hand, the other lattice constant "c" initially increases to 0.5183nm at 0.1mol% of Tb concentration; it decreases marginally to 0.5164nm for ZnO: Tb (0.5mole%) and by ~8% to 0.5127nm for ZnO: Tb (1.0mol%). However, the "c/a' ratio is found to be about 1.60 at all the three doping concentrations implying that the basic wurtzite structure of ZnO is not altered at these doping levels.

The variation of the unit cell volume with the Tb doping concentration also calculated from XRD data is shown in Fig 5.7B. The unit cell volume varies with Tb concentration almost similar to that of lattice constant "c"; Compared to ZnO, the volume is higher for ZnO: Tb (0.1 mol%) but decreases with further increase in Tb concentration.

The above mentioned observations regarding the variation of lattice constants and unit cell volume with the doping concentration of Tb implies that Tb doping in the concentration range 0.1-1.0 mol% did not change, as mentioned earlier, the basic wurtzite structure of the ZnO. However, the variation of the unit cell volume and the shifting of the peak positions of the diffraction peaks could be due to the development of strain in the unit cell of ZnO on Tb doping. The ionic radius of Tb^{3+}(92*pm*) being more than of Zn^{2+}(88*pm*), the increase in the unit cell volume and crystallite size when ZnO was doped with 0.1mol% Tb could be attributed to the incorporation of Tb interstitial or substitutional in ZnO unit cell. On the other hand, at 0.5 and 1.0 doping concentrations the unit cell volume decreased mainly because of the decrease in lattice constants "a &c" as if some sort of "pressure" was applied to ZnO unit cell. This could be due to the migration of Tb to the surface; similar conclusions have been reported in the literature. The observed shift in the peak positions of the diffraction peaks, as mentioned earlier, almost halved when doping concentration was increased from 0.5 to 1.0 mol% implying that the strain in the ZnO unit cell was more with 0.5 mol% concentration. This could be due to increase in the accumulation of Tb at surface with increase in doping concentration.

On the other hand no significant change in the lattice constants and unit cell volume was observed when ZnO was single doped with Ce, Eu and Gd.

5.2.4.3 Crystallite sizes

The average size of the crystallites was calculated by the well-known Scherrer formula (Eq. 5.1):

$$D = k\lambda/B \cos\theta \qquad (5.1)$$

Where D is mean crystalline size in nm, k is a dimensionless constant usually taken as 0.9, λ is the wavelength (nm) of the X-ray radiation used to record the diffraction pattern, B is full width at half maximum (rad) of any peak in XRD pattern and θ is the angle (in degrees) between the incident and diffracted beams. Fig 5.8 shows the dependence of crystallite size on the doping concentration of Tb in ZnO. The calculated crystallite size of ZnO powder, as seen in this figure, was ~35nm which increased to ~48nm when it was doped with 0.1 mol% Tb. On further increase in doping concentration to 0.5 mol% calculated crystallite size was found to be ~34nm (almost same as that of ZnO) which increased to ~45nm with 1.0 mol% doping level. On the other hand no such concentration dependent variation was observed in case of Gd, Ce and Eu. The calculated average crystallite size was ~45nm for ZnO: Gd powders while its value was ~57nm for both ZnO: Ce and ZnO: Eu.

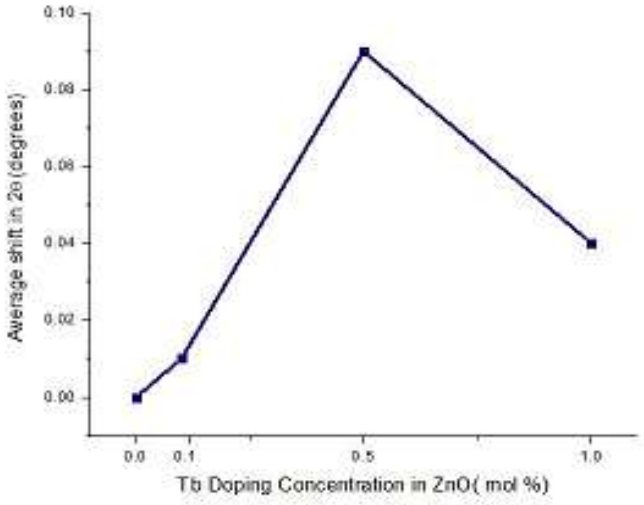

Fig 5.8: Variation of the crystallite size as a function of Tb doping concentration

5.2.5 UV-VIS absorption

UV-VIS spectroscopy, as discussed in Chapter 1, is used to investigate the optical band gap and the absorption edge of a semi-conductor. This optical band gap energy E_g of a

direct- band gap semiconductor is related to the absorption coefficient "α" and to the absorption frequency ν by the following relation:

$(\alpha h\nu) = K (h\nu - E_g)^{1/2}$, K being the constant of proportionality. (5.2)

Room temperature UV-VIS absorption spectra of ZnO and ZnO: Tb sintered at 700^{o}C is shown in Fig 5.9a. As seen in this figure, the observed absorption of ZnO was >80% in 200-370nm range (absorption edge at 370nm) while in case of ZnO: Tb (0.1mol %), the absorption decreased to ~30% with absorption edge at 380nm. On further increase in doping concentration, the absorption showed increase; ~65% for ZnO: Tb (0.5mol %) and >80% for ZnO: Tb (1.0mol %)0 which is marginally greater than the ZnO. This variation of absorption with Tb doping concentration could be attributed to the changing nature of defect centers with Tb doping.

Fig 5.9b shows the plot of $(\alpha h\nu)^2$ as a function of hν; the functional dependence of α and ν was computed from the UV-VIS spectra shown in Fig 5.9a. The intercepts of these graphs (Fig5.9b) on X-axis which are the measures of the optical band gaps of ZnO and ZnO: Tb (0.1, 0.5 and 1.0 mol %), are listed in Table 5.2.

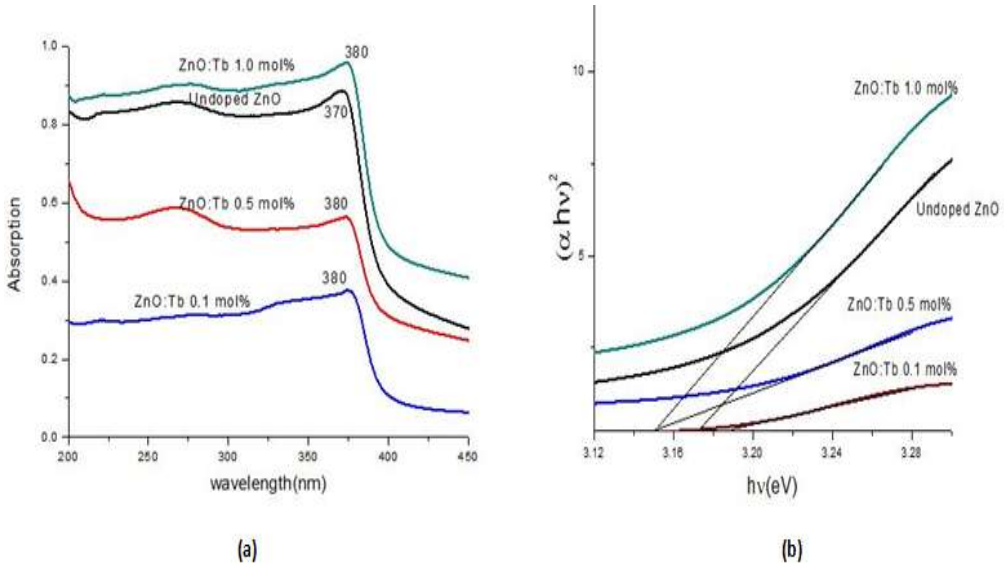

Fig 5.9: (a) Room temperature UV-VIS absorption spectra of ZnO and ZnO:Tb, (b) Plot of "hν" with $(\alpha h\nu)^2$, α being absorption intensity computed from UV-VIS spectra (Fig 5.9 a)

Table 5.2 : Band gaps computed from UV-VIS absorption data (Figs 5.9a and 5.9b)

Sample	Observed absorption edge (nm)	Estimated band gap (ev)
ZnO	370	3.17
ZnO:Tb (0.1mol %)	380	3.18
ZnO: Tb (0.5mol%)	380	3.15
ZnO: Tb (1.0mol %)	380	3.15

The optical band gap values of ZnO shown in Table 5.2 match reasonably well with the values reported in the literature (Chapter 2)

Similar results were observed when ZnO was doped with Gd, Eu and Ce dopants implying that no significant change in observed optical band gap resulted with the change in the nature of the dopants.

5.2.6 Raman spectra

Raman spectroscopy being sensitive to lattice distortions was used to reconfirm this conclusion arrived at from the XRD analysis. The unit cell of wurtzite type ZnO has 4 atoms (2Zn, 2O) with 12 (4x3) phonon modes; 3 being the acoustic phonons and 9 (3LO & 6TO) the optical phonons. The space group associated with unit cell being C^4_{6v} the optical phonons belong to the irreducible representation as:$A_1+2E_1+2E_2+ 2B_1$; $2B_1$ modes are IR as well as Raman inactive, $2E_2$ are only Raman active while rest are both IR as well as Raman active. A_1 and $2E_2$ being polar further split in LO and TO with different frequencies. Raman scattering involving one, two and more than two (multi) phonon processes have been observed in ZnO. The expected shifts in one phonon Raman scattering is < 600cm^{-1} with a gap between the acoustic and optical branches from 270 to 370 cm^{-1}. Raman shifts based on two phonon differences also are expected to be <600 cm^{-1} while higher than 600 cm^{-1} shifts are attributed to the “two phonon sums” and/or multi phonon processes.

Typical room temperature Raman spectra of ZnO and ZnO:Tb excited by 514.5nm radiation from an Ar-ion laser is shown in Fig 5.10a. As seen in this figure, the Raman shifts at 330,439,583 and 1145cm^{-1} were observed in ZnO powder samples at room temperature. Table 5.3 summarizes the associated phonon modes assigned with the help of the literature (Chapter 2)

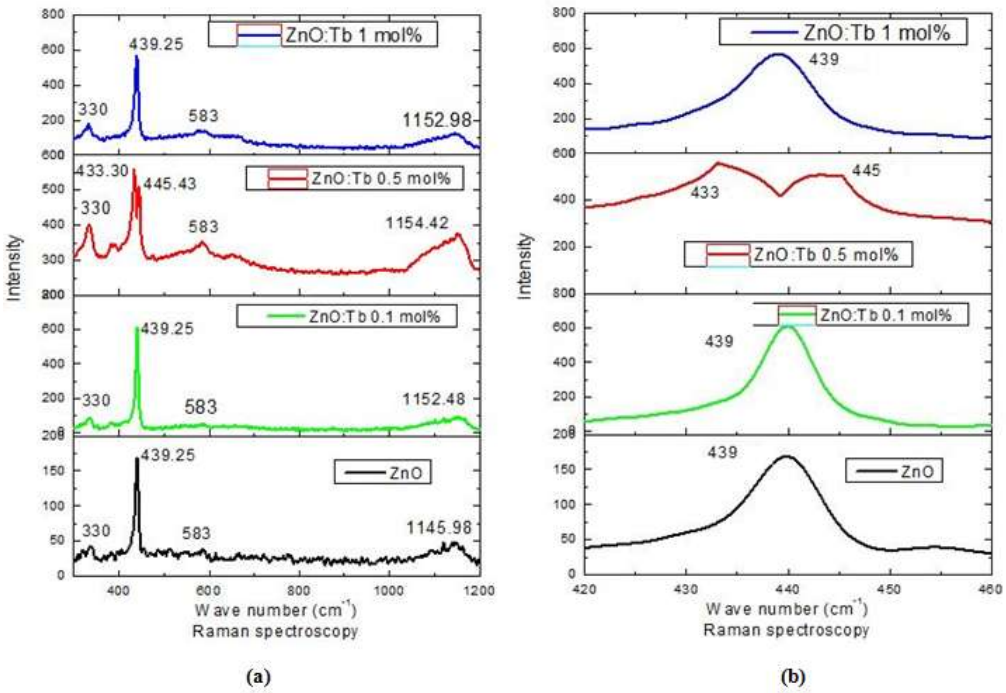

Fig 5.10 : (a) Room temperature Raman spectra of ZnO and ZnO: Tb (0.1, 0.5 and 1.0 mol%); all the samples were sintered at 700^{o}C.(B) Splitting of 439 cm^{-1} Raman line in ZnO: Tb (0.5mol%).

The observed Raman shifts (Fig 5.10a) at 439 and 583 cm^{-1} are due to one phonon processes while multi-phonon processes could be responsible for the relatively broader shift peaking ~1145cm^{-1} . On the other hand 330cm^{-1} shift could be the result of "two phonon difference" (Table 5.3). The main changes observed in the Raman Spectra (Fig 5.10) on doping with Tb are:

1. An increase in the intensity of Raman scattering.
2. The peak positions of the Raman shifts at 330 and 583 cm^{-1} did not change.
3. In case of 439 cm^{-1} Raman line the peak position did not change at 0.1 and 1.0 mol% while it split into two lines (433 and 445cm^{-1}) for 0.5mol% doped samples.

4. Raman shift observed at 1145 cm^{-1} in ZnO was red shifted by ~8cm^{-1} on doping; this shift was same for all the doping concentrations.
5. The integrated area (arb. units)) under 439cm^{-1} are as follows:
   ZnO = 1531; ZnO: Tb ((0.1mol %) = 5596; ZnO: Tb ((0.5mol %) Peak 1=3681; ZnO: Tb ((0.5mol %) Peak 2= 1606; ZnO: Tb ((1.0mol %) = 6027

On the other hand the integrated area (AU) under 1145 cm^{-1} (1153 cm^{-1} in doped ZnO) is as follows:

ZnO=1686; ZnO: Tb ((0.1mol%)=4819; ZnO: Tb (0.5mol%)=8630; ZnO: Tb (1.0mol%)=5062

Table 5.3: Phonon modes associated with the observed Raman shifts

Observed Raman shift cm^{-1}	Associated phonon mode
330	E_2 (high)-E_1 (low)
439	E_2 (high)
583	E_1
1145	2xA_1 (low)

The observed increase in the intensity of Raman scattering on Tb doping can be attributed to the increase in defects and strain in ZnO lattice. The splitting of 439cm^{-1} Raman mode in 0.5mol% doped ZnO implies that the maximum strain developed at this concentration level. This is further supported by the observation of maximum intensity change (~5times) in 1145cm^{-1} (1153cm^{-1} in ZnO: Tb 0.5mol %) Raman mode as this mode involves multi-phonon processes, is expected to be very sensitive to lattice strain.

Similar Raman spectra were observed in case of Ce, Eu and Gd doped ZnO; the intensity of this spectra increased significantly on doping. However, no splitting and/or shifting of Raman lines on doping of these elements were observed.

5.2.7 Photoluminescence (PL)

The aim of this study, as mentioned earlier, was to investigate the suitability of the rare-earth doped ZnO nano phosphors for the development of white light sources. The detailed study of the visible emission from ZnO doped with Gd, Tb, Ce and Eu is described in the following sections.

5.2.7.1 ZnO: Gd

Photoluminescence in the visible region (400-700nm) was observed when Gd: ZnO nano phosphor at room temperature was excited with 280,300,345, 395 and 460nm radiation from a Xe lamp. Fig 5.11a shows the typical emission spectra when excited with 280,300 and345nm radiation.

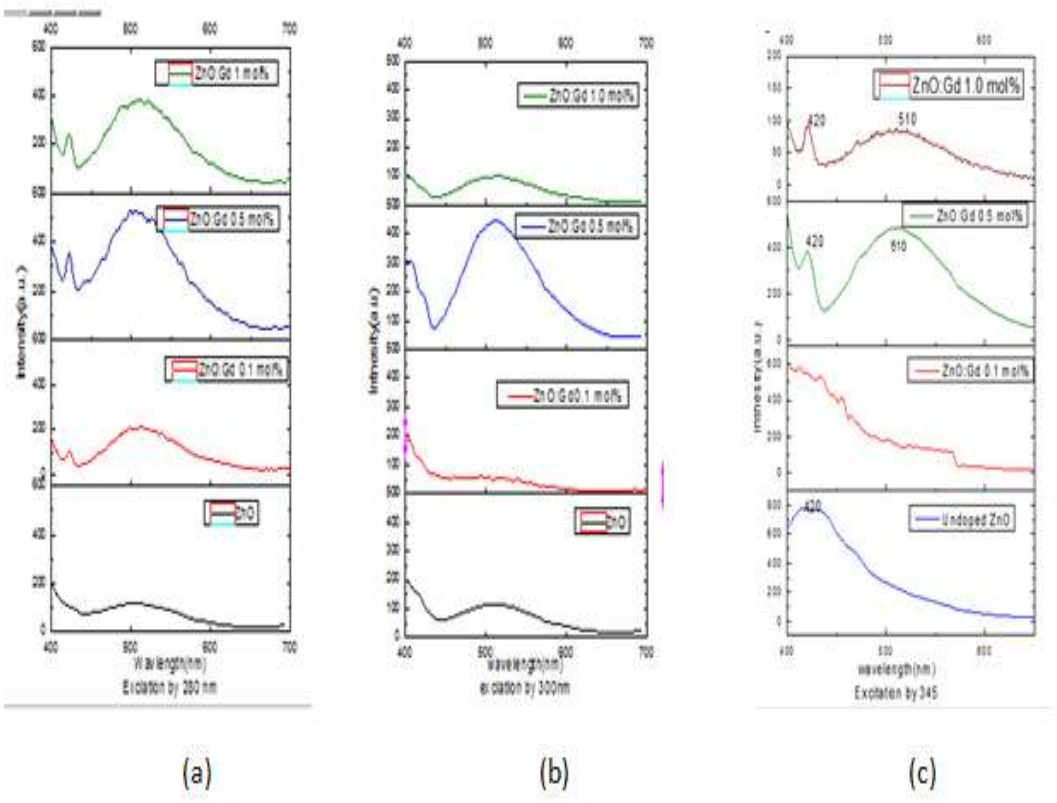

Fig5.11: Photoluminescence spectra of Gd: ZnO Nano phosphor at room temperature excited by 280, 300 and 345nm radiation. The emission spectrum of undoped ZnO are shown for comparison.

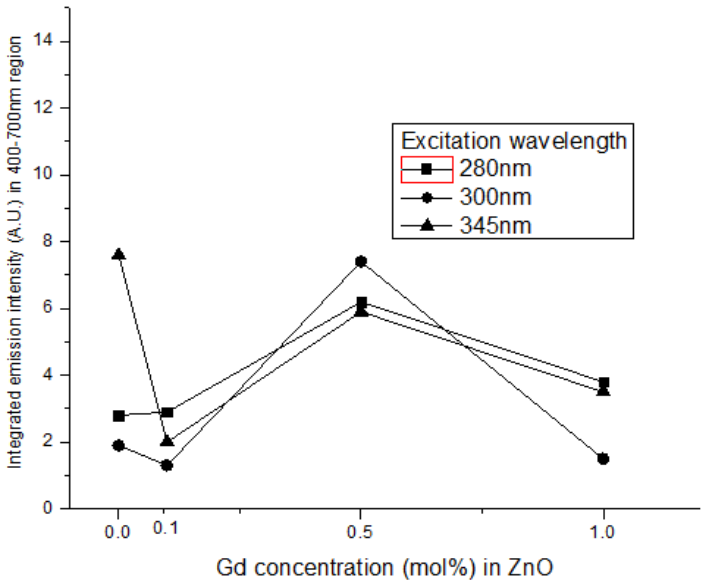

Fig.5.12: Integrated photoluminescence intensity in 400-700nm region for various excitations as a function of Gd concentration in ZnO

As seen in Fig 5.11, the spectral positions of the emission spectra when excited with 280, 300 and 345nm radiation are almost the same while there is, significant change in intensity pattern as shown in Fig.5.12 where integrated photoluminescence intensities observed in 400-700nm region are plotted as a function of Gd doping concentration. As seen in this figure, the integrated emission intensity of 0.5mol% doped Gd in ZnO in 400-700nm region is maximum compared to that of 0.1 and 1.0 mol% Gd doping concentration as well as that of undoped ZnO for all the three excitations. 300nm excited photoluminescence intensity excited increases by a factor of 3 when Gd doping concentration is increased from 0.1mol% to 0.5mol% which is expected as number of emitting centers increases with the increase in doping concentration. However, the decrease in the intensity almost by the same factor is observed when Gd concentration is increased to 1.0 mol% implying the well-known 'concentration quenching" which is due to the transfer of energy between the close neighbors. This transfer could be between two Gd ions and/or between a Gd ion and ZnO lattice. Almost similar behavior is observed with 280 and 345nm excitations.

280 and 300 nm excited PL intensity (Fig 5.12) of undoped ZnO decreases marginally compared to 0.1 mol% Gd: ZnO; however, with 345nm excitation, the photoluminescence intensity of undoped ZnO is maximum which decreases by almost by a factor of 4 compared to that of 0.1mol% Gd doped ZnO.

The main observations of Fig. 5 can be summarized as:

1. Undoped ZnO has maximum PL intensity with 345nm excitation.
2. The PL intensity of 0.1mol% doped ZnO is less than that of undoped ZnO; marginal in case of 280 and 300nm excitation while 4 fold decrease in case of 345nm excitation.
3. PL intensity increase almost by a factor of 4 when Gd concentration is increased from 0.1 to 0.5mol%; this intensity decreases significantly when doping concentration is increased to 1.0 mol % showing 'concentration quenching".

Nano-structured undoped ZnO, as mentioned earlier, is known to absorb UV and blue radiation and emit around 382 and 500nm regions, the former being the band –edge emission while later is the defect emission. Both the maxima of the emission as well as absorbance are particle size dependent; there is a red shift in case of the both maxima with the increase in particle size. The observed increased PL intensity in undoped ZnO with 345nm excitation compared to that of 280 and 300nm could be due to particle size of ZnO powder synthesized, as mentioned earlier, by wet chemical technique in the present study.

PL of Gd doped ZnO excited by 280, 300 and 345nm radiation can be due to 4f-4f transitions in Gd^{3+}. Its ground state, as shown in Fig 5.13, is $^{8}S_j$ while the first excited state manifold $^{6}P_j$ cover the energy range from 32100 to 33200 cm^{-1}.The next excited state manifold $^{6}I_j$ spans the energy range 35800 to 36600 cm^{-1} followed by $^{6}D_j$ at 39500 to 40600 cm^{-1} and $^{6}G_j$ at 50000 cm^{-1}. This type of energy levels structure makes Gd unique among rare–earths as there is no possibility of IR emission or absorption. The transitions responsible for the observed absorption and emission are summarized in Table 5.4. The observed concentration quenching unequivocally shows that the observed emission is due to Gd^{3+} emitters.

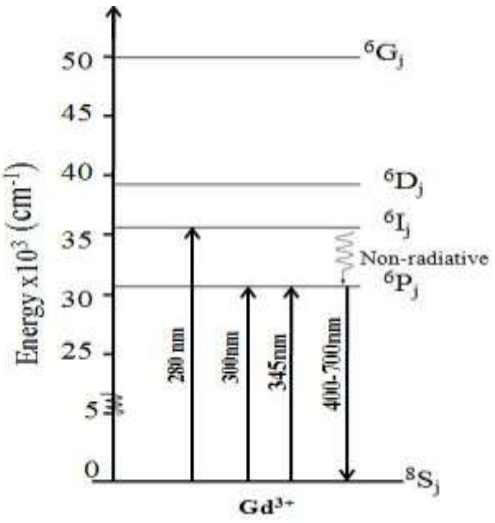

Fig 5.13: Energy level diagram of Gd^{3+} showing the transitions responsible for absorption and emission.

Table 5.4: Absorption & emission transition assignment

Type	wavelength	Transition
Absorption	280nm	^8S_j to ^6I_j
Absorption	300nm	^8S_j to ^6P_j
Absorption	345nm	^8S_j to ^6P_j
Emission	400-700nm	^6P_j to ^8S_j

On the other hand, Fig 5.14 shows relatively sharp emission peaks at 485 and 538nm when excited with 395nm (25316cm^{-1}) radiation while 460nm (21739cm^{-1}) excitation results in single emission peak at 628nm; marginal increase in the emission intensity with the increase in Gd concentration is observed in both the emission spectra. This is well known emission pattern of undoped ZnO attributed to oxygen vacancies. However, the observed marginal increase in the peak intensities of the PL lines with the increase in Gd concentration could be attributed to the creation of more defects (oxygen vacancies) by Gd doping as both these excitations cannot be absorbed by Gd^{3+} (Fig 5.13).

The CIE 1931 color space diagram showing the chromaticity coordinates x and y for the 300nm excited emission from 0.5mol% doped Gd: ZnO is shown in Fig 5.15.

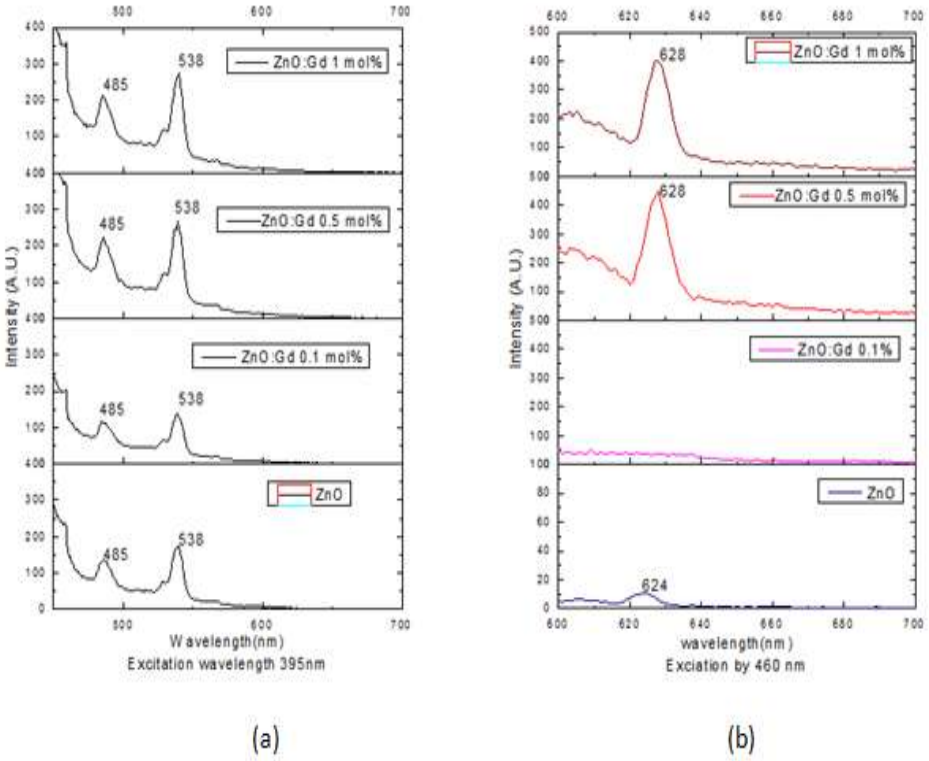

Fig 5.14: Photoluminescence spectra of Gd: ZnO nano phosphor at room temperature excited by 395 and 460nm radiation. The emission spectrum of undoped ZnO is shown for comparison.

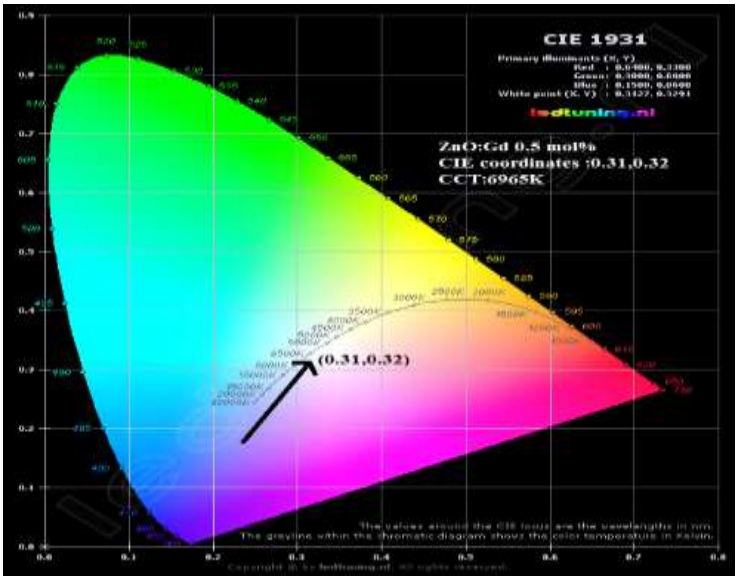

Fig5.15: Chromaticity coordinates x & y for 300nm excited emission from 0.5mol% Gd: ZnO

The calculated chromaticity coordinates x and y, as seen in Fig 5.14, are x=0.31 and y=0.32 indicating the potential of this material in realization of optical sources/displays

5.2.7.2 ZnO:Tb

Room temperature PL of the powder samples of ZnO: Tb (sintered at 700^{o}C) was excited with 280, 300, 380 and 460nm radiation from a Xe lamp. Several sharp emission peaks in blue-green region were observed when excited with 380nm radiation while excitation with 460nm radiation resulted in the emission of a sharp peak at 626 nm. On the other hand, broad emission (122nm FWHM) peaking around 510 nm was observed when excited with 280 and 300nm radiation. This excitation wavelength dependence of PL is discussed in the following sections.

The room temperature PL spectra of ZnO and ZnO: Tb (0.1, 0.5 and 1.0 mol %) excited with 380nm radiation from a Xe lamp is shown in Fig 5.16a.

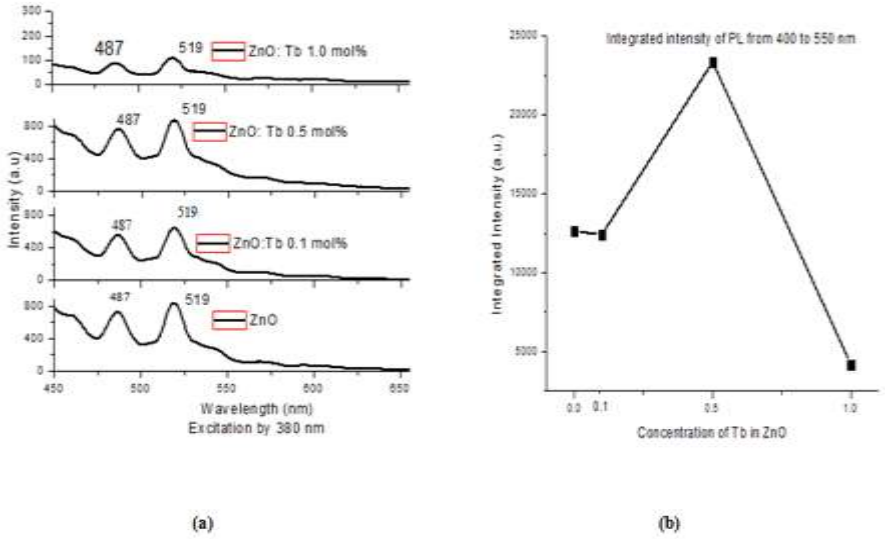

Fig 5.16: (a) Room temperature PL spectra of ZnO and ZnO :Tb (0.1, 0.5 and 1.0 mol %) excited with 380nm radiation from a Xe lamp ;(b) Integrated intensity of PL (IPLI) in 400-550nm range as a function of Tb doping concentration.

Two PL peaks around 487nm (2.54eV) and 519nm (2.3eV) were observed (Fig 5.16a) when excited with 380nm (3.26eV) radiation from a Xe lamp. This "yellow-green" emission attributed to defect states has been widely reported in the literature (Chapter 2).

On doping with, Tb the peak positions of the observed PL did not change while doping concentration dependent variations were observed in its (PL) intensity as shown in Fig 15.5b where integrated PL intensity (IPLI) in 400-550nm region is plotted as a function of Tb concentration. As seen in this figure, IPLI for 0.1mole % doped samples is almost same as that of ZnO while its value is doubled for the 0.5mol% doped ZnO. However, a sharp (by about 30% compared to ZnO) decrease is observed in 1.0mol% doped ZnO powder sample. The energy level diagrams of ZnO and Tb $^{3+}$(Tb normally enters a lattice as Tb^{3+}) are shown in Fig.5.17. The conduction band (CB) of ZnO, as seen in this figure, is around 27000cm^{-1}(~3.37eV) while Tb^{3+} has energy levels up to 35000cm^{-1}(4.34eV) with the energy of ^5D_j levels almost coinciding with CB of ZnO.

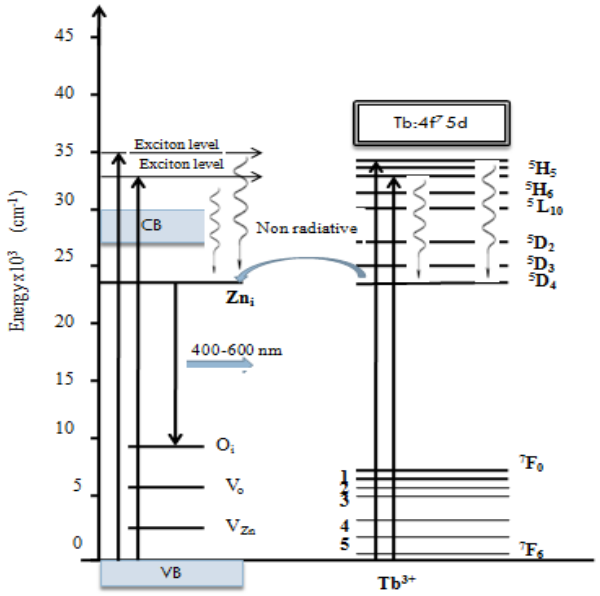

Fig 5.17 : Energy diagram of ZnO and Tb^{3+}

It is well known, as mentioned earlier, that ZnO absorbs in UV region and has emission in blue and green regions of the electromagnetic spectrum. This emission is attributed to the transitions between the CB and defect levels and/or between defect levels as shown in Fig 5.17. On the other hand, 380nm radiation can populate ^5D_j levels of Tb^{3+}. The population of this level may decay through non-radiative processes to $^5D_4$ (Fig 5.17) which on decaying to ^5F_j levels is responsible for emission in 500-600nm region. However, this emission consists of two sharp peaks at 540 and 587nm while in ZnO: Tb,

the observed emission has almost all the spectroscopic features except intensity similar to that of ZnO. This increase in PL intensity on doping could have implied energy transfer from Tb to ZnO which looks unlikely because of the nature of the doping concentration dependence on the PL intensity as shown in Fig 5.16b. Almost same IPLI for ZnO and ZnO: Tb (0.1mol%) indicates that at this doping concentration Tb, could be incorporated in ZnO unit cell interstitially or substitutionally while at 0.5 and 1.0 mol% doping concentrations, accumulation of Tb at surface could be the dominating process. The maximum IPLI observed at 0.5mol% could be due to the highest defect density induced in ZnO at this concentration level; this conclusion is consistent with the analysis of XRD and Raman data discussed in earlier sections.

The excitation with 460nm radiation results in emission around 628nm both in ZnO as well as in ZnO: Tb. This "red emission" in ZnO attributed to the transitions involving defect states, also had maximum intensity with 0.5mol% Tb doping

Relatively broad (~122nm FWHM) emission, as mentioned earlier, peaking ~510nm was observed both in ZnO as well as ZnO: Tb when excited with 280 and 300nm radiation; in this case also the emission intensity was maximum when ZnO was doped with 0.5mol% Tb. Typical PL spectra of 0.5mol% ZnO: Tb powder sintered at 700^{o}C is shown in Fig 5.18 where that of ZnO also (sintered at 700^{o}C) has been shown for comparison.

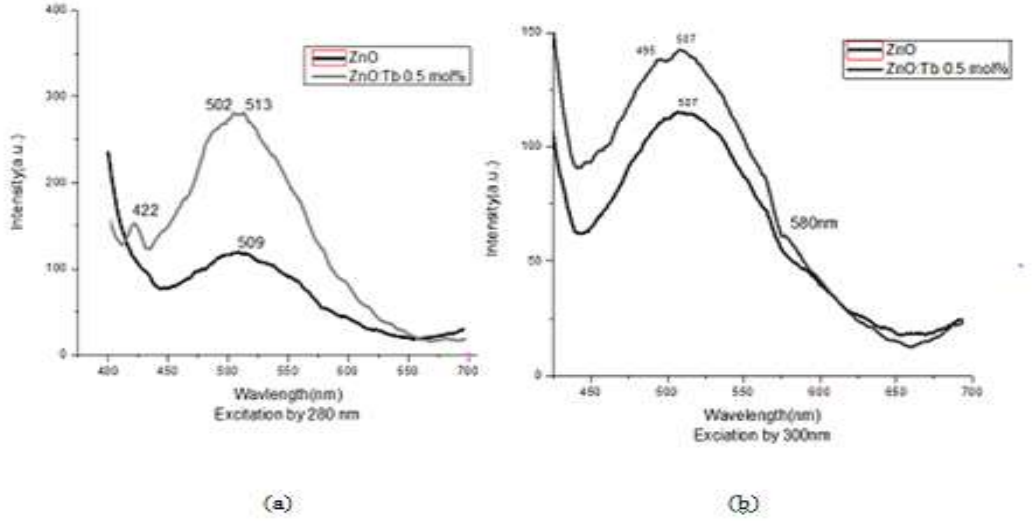

Fig 5.18: Room temperature PL spectra excited by (a) 280nm radiation and (b) 300nm radiation. All the samples ere sintered at 700^{o}C

The main observations from Figure 5.18 are summarized in Table IV.

Table 5.5: Main observations regarding PL excited by 280nm and 300nm radiation

	280nm excitation		300nm excitation	
Powder Sample (mol%)	PL integrated Intensity (arb, units)	PL FWHM (nm)	PL integrated Intensity (arb, units)	PL FWHM (nm)
ZnO	2.12	122	1.86	122
ZnO: Tb 0.5	2.55	122	2.31	120

As seen in Fig 5.18 and summarized in Table 5.5, it is observed that:

i. The excitation of ZnO with 280 and 300nm radiation results in emission peaking around 510nm; the intensity of this emission excited with 280nm radiation is ~12% more compared to that of the emission excited with 300nm radiation.

ii. Both peak position and FWHM of the emission spectra did not change on Tb doping irrespective of the wavelength of excitation radiation.

iii. The intensity of this emission increases on doping; this increase is ~20% in case of 280nm excited PL compared to 24% observed in case of the emission excited with 300nm radiation. However maximum emission intensity is observed in case of ZnO:Tb (0.5mol %) when excited with 280nm radiation.

As discussed earlier in this section, the increase in PL intensity on Tb doping could be mainly due to increase in defect density in ZnO on Tb doping.

The summary of the CIE 1931 color space analysis carried out for all the emission spectra shown in Fig 10 are summarized in Table V. As seen in this table, the only emission with characteristics similar to that of "day light" is the emission from ZnO: Tb excited by 280nm radiation. Its calculated chromaticity coordinates (Fig 5.18) are: x=0.29 and y=0.31, indicating its potential for the realization of the white light sources.

Table 5.6: Calculated chromaticity coordinates for 280 and 300nm excited PL in ZnO and ZnO:Tb

Sample (mol%)	Coordinates for 280 nm excited PL	Coordinates for 300nm excited PL
ZnO	X= 0.25, Y= 0.33 blue purple hue CCT= 10526K	X= 0.28, Y= 0.29 blue green hue CCT= 9763K
ZnO: Tb 0.5	X= 0.29, Y= 0.31 day light hue CCT= 8170K	X= 0.27, Y= 0.27 blue purple hue CCT= 13237K

Also, other special "light sources" like "blue-purple" and "blue-green" can be realized simply by changing radiation used for PL excitation (Table 5.6).

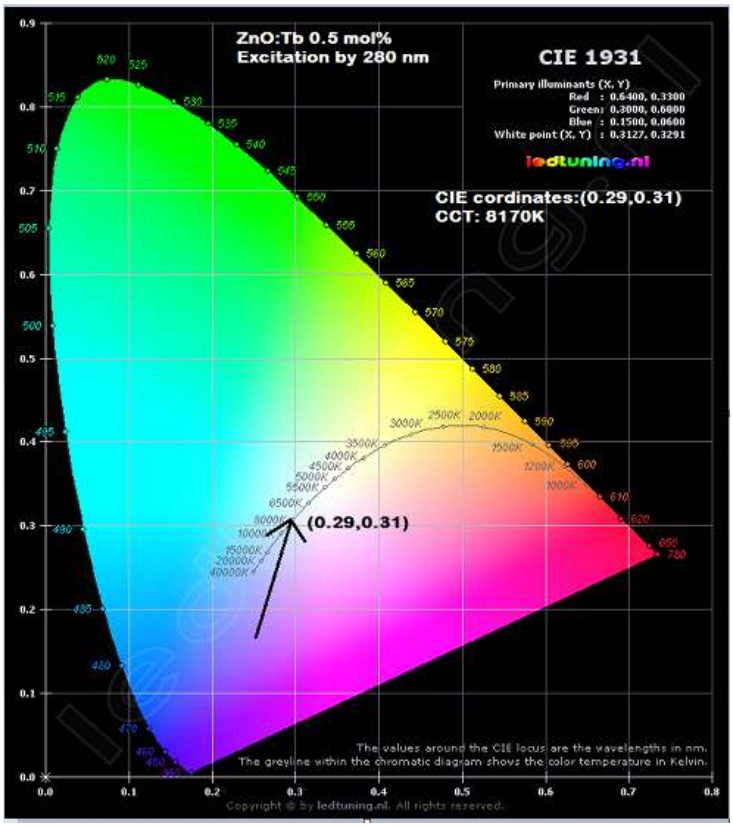

Fig 5.19: Calculated chromaticity coordinates for 280 excited PL in ZnO:Tb (0.5mol%)

5.2.7.3 ZnO: Ce and ZnO: Eu

Typical PL spectra of ZnO:Ce (0.5mol%) and ZnO:Eu (0.5mol%) excited by 280 and 380nm radiation are shown in Fig 5.20 and 5.21.

Similar to single doped ZnO: Gd and ZnO: Tb, discussed in earlier sections, broad band emission peaking ~510nm (Fig 5.20a) was observed when excited with 280nm radiation while emission consisting of sharp peaks (425, 487 and 519nm) was recorded when excited with 380bm radiation from both ZnO: Ce and ZnO: Eu. The CIE diagrams for the broad emission excited by 280nm radiation are shown in Fig 5.22 and Fig 5.23.

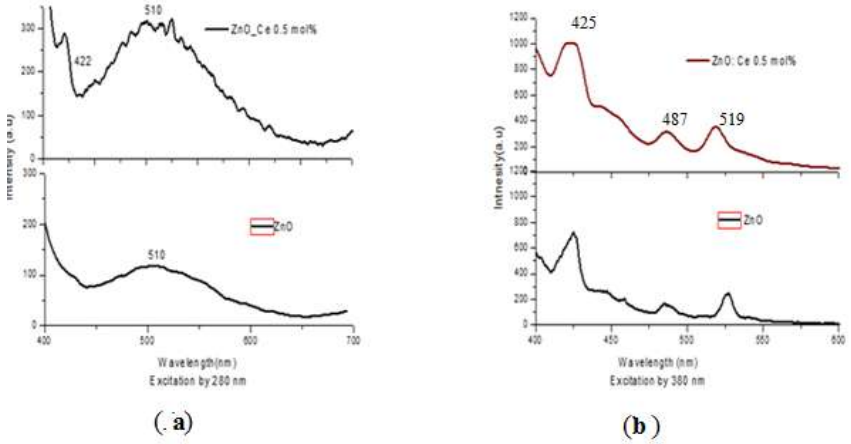

Fig 5.20: Typical room temperature PL of ZnO: Ce 0.5mol% (a) excited by 280nm (b) 380nm radiation.

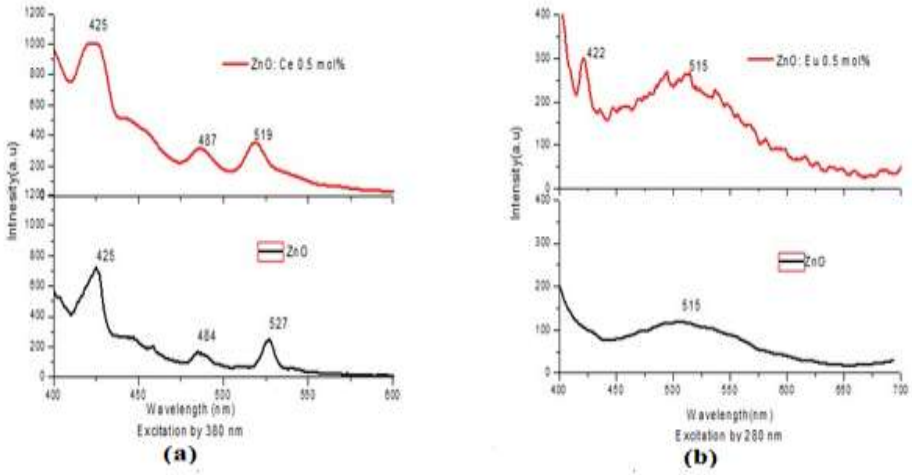

Fig 5.21: Typical room temperature PL of ZnO: Eu 0.5mol% (a) excited by 280nm (b) 380nm radiation

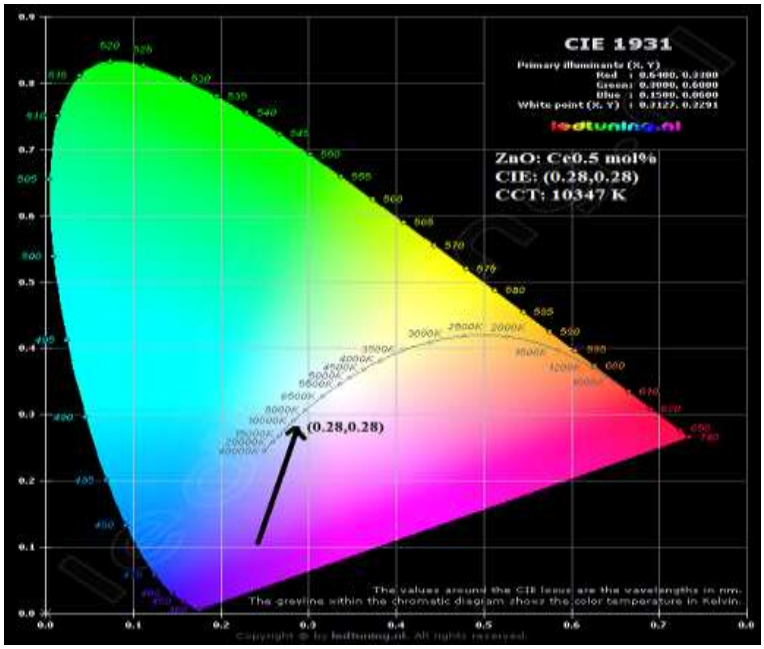

Fig 5.22: CIE diagram of ZnO: Ce 0.5 mol%

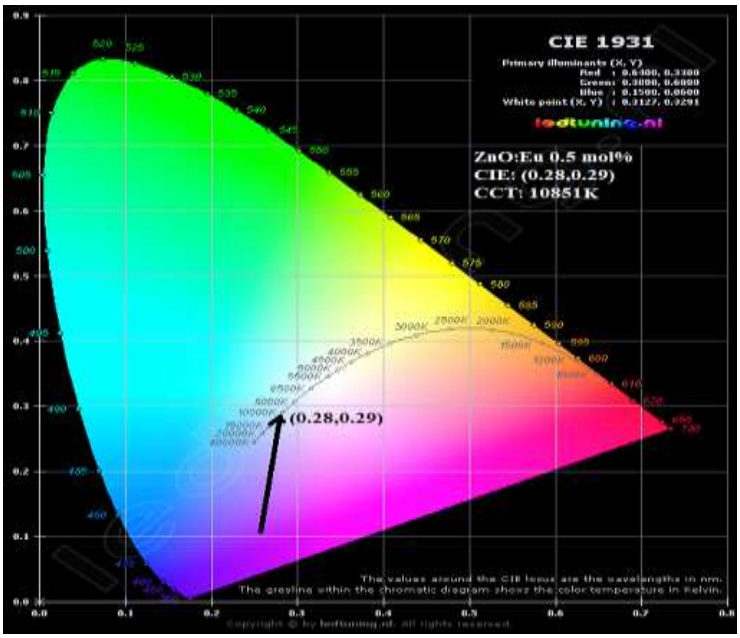

Fig 5.23: CIE diagram of ZnO: Eu 0.5 mol%

As seen in Fig 5.22 the chromaticity color coordinates for ZnO:Ce are x=0.25; y=0.28 while for ZnO:Eu (0.5mol%) x= 0.28; y=0.29 (Fig.5.23)indicating the suitability of these materials for the development of multi-colored light sources.

REFERENCES

[1] Koao L F (2016) *Physica B* 480:53-57

[2] Heng et al (2016) *Mater. Lett.* 162: 53-55

[3] Li et al (2015) *Mater. Lett.* 138: 188-191

[4] Pandey et al (2015) *Optik* 126 : 3310-3315

[5] Chelouche et al(2014) *Optik* 125 : 5626-529

[6] Oudhia et al (2016) *Nano-Structures & Nano-Objects* 7: 69-74

[7] Pessoni H V S, Maia L J Q and Franco A (2015) *Jr; Mater. Sci. Semicond. Process* 30: 135-141.

[8] Najafi M and Haratizadeh H (2015) *Solid State Sci.* 41: 48-51

[9] Zong et al (2014) *Ceram. Int* 40: 10375-10382

[10] Shahroosvand H, Ghorbani-asl M (2013) *J. Lumin.* 144:223-229

[11] Tsuji T et al (2012) *J. Lumin.* 132: 3125-3128

[12] Du et al(2008) *J.Phys.Chem C* 112:12234-12241

[13] Ishizumi A and Kanemitsu Y (2005) *Appl. Phys. Lett.* 86: 253106

[14] Rani et al(2017) *J Sol-Gel Sci Technology* 82: 586-592

[15] Koao et al (2016) *Adv. Mater. Lett.* 7:529-535

[16] Hastir A, Kohali Y and Singh R C (2016) *Sens. Actuators B* 231:110-119

[17] Kabongo et al (2014) *J. Alloys Compd.* 591: 156-163

CHAPTER 6

ZnO NANO PHOSPHOR CO-DOPED WITH Ce AND Eu

6.1 Introduction

Un-doped and co doped (with Ce and Eu) ZnO (Zinc Oxide) powders were prepared by co- precipitation method, as discussed in Chapter 3, followed by sintering in air at temperatures 700^{o}C using a home-made muffle furnace (Chapter 3).The doping concentrations investigated were 0.1,0.5 and 1.0 mol%.; six powder samples were prepared by permuting of theses concentrations. The samples thus prepared were characterized using X ray diffraction (XRD) canning/transmission electron microscope (SEM/TEM),EDX, Fourier transform infrared spectroscopy(FTIR) , Raman spectroscopy and photoluminescence(PL) techniques.

Earlier, Murugadoss et al [1] studied the powder samples of ZnO co-doped with Ce and Eu where they observed the shifting of the XRD diffraction peaks on co-doping. This shift was interpreted in terms of the lattice distortions induced by co-doping. However, they did not investigate, in detail, the properties of the visible emission from the co-doped samples.

6.2 Results and discussion

6.2.1 EDX

Typical EDX spectrum of ZnO co-doped with Ce (1.0mol %) and Eu (0.5mol %) is shown in Fig.5.1.

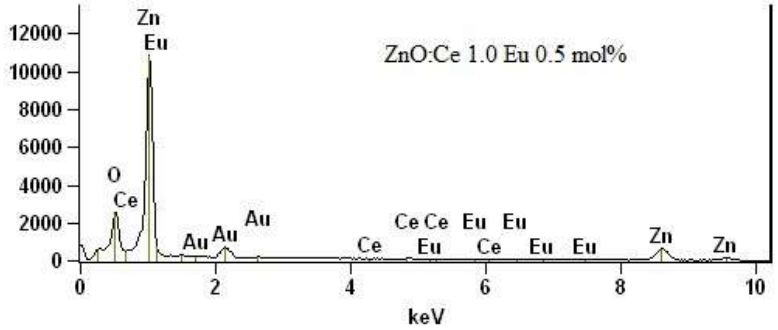

Fig 6.1: EDX spectra of ZnO co-doped with 1.0mol% Ce and 0.5mol% Eu

Ce and Eu peaks along with those of Zn and O are seen in Fig 6.1 confirming the doping of the both the rare-earths in ZnO. Similar results were observed in ZnO samples doped with other concentration combinations of Ce and Eu. The peak due to Au was because of the gold sample holder used to record the spectrum.

6.2.2 SEM/TEM image

Typical SEM/TEM image of the powder sample (sintered in air at 700^{o}C) of ZnO co-doped with 0.5 mol% of Ce and 1.0 mol% of Eu is shown in Fig 6.2. As seen in this figure, the sample was composed of spherically-shaped particles along with some non-spherical large sized grains which could be due to agglomeration and/or strain induced by Ce and Eu doping as discussed in following sections. Similar images were recorded for other co-doping concentration combinations.

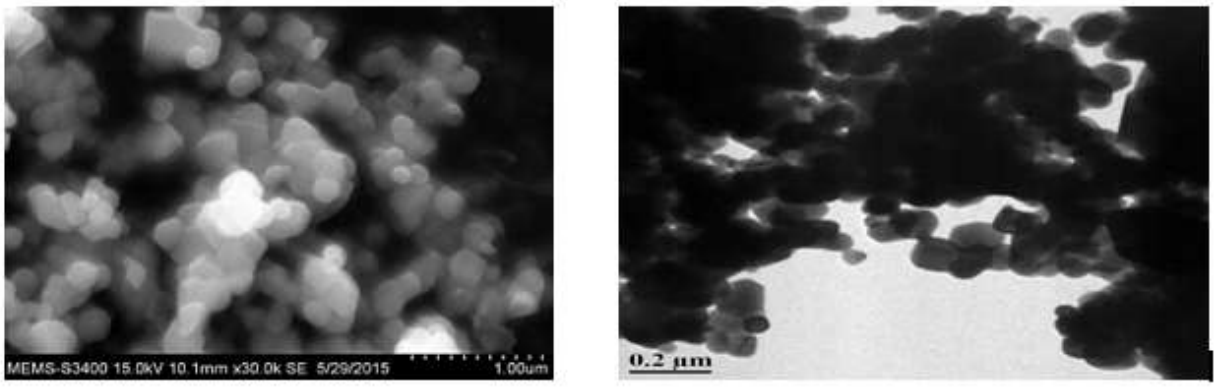

Fig 6.2: (a) Typical SEM image (b) typical TEM image of ZnO powder sample co-doped with 0.5mol% Ce and 1.0 mol% Eu sintered at 700^{o}C

6.2.3 FTIR

Fig 6.3 shows the typical FTIR spectrum of the powder samples of ZnO co-doped with 0.5mol% of both Ce and Eu; FTIR spectra of ZnO, ZnO: Ce0.5mol% and ZnO: Eu (0.5mol%) were included for comparison. All the samples were sintered in air at 700^{o}C. All the main spectral features of the FTIR spectra shown in Fig 6.3 are similar implying that the basic structure of ZnO did not change on doping. The absorption peak in 400-

600cm^{-1}region is due to metal oxygen bond (Zn-O, Eu-O, Ce-O) vibrations while relatively weak absorption at 3500 cm^{-1} is due to water present in the atmosphere. Similar features were seen in the FTIR spectra of ZnO co-doped with other concentration combinations of Ce and Eu.

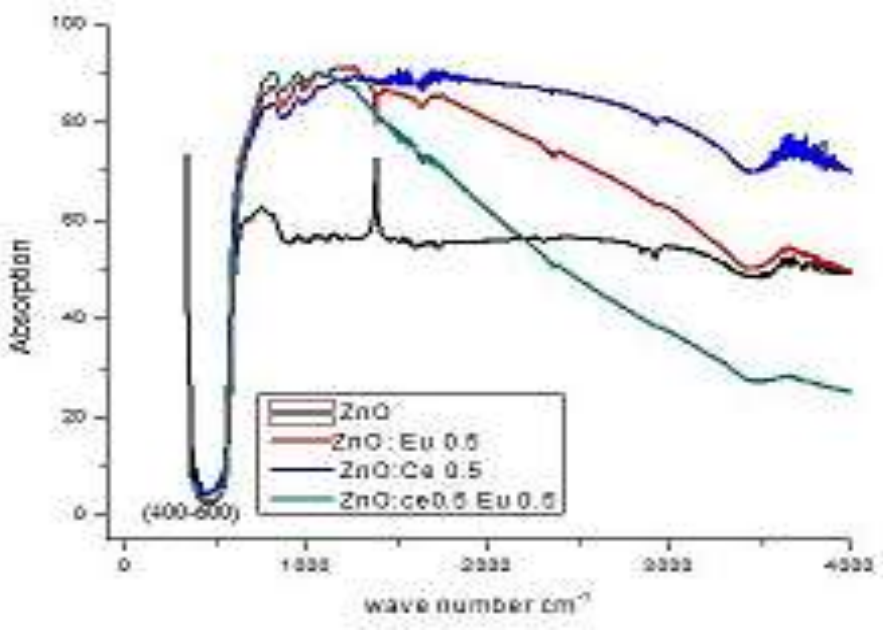

Fig 6.3: FTIR spectrum of ZnO co-doped with 0.5mol% of both Ce and Eu; spectra of ZnO, ZnO: Ce 0.5 mol% and ZnO: Eu 0.5 mol% are shown for comparison.

6.2.4 XRD

Powder XRD spectra of ZnO and ZnO co-doped with Ce (0.1, 0.5 and 1.0mol%, variable) and Eu (0.1mol%, constant) are shown in Fig 6.4; all the powder samples were sintered at 700^{o}C. These XRD patterns could be indexed using JCPDC file No. 36-1451. Similar results were observed with (i) ZnO:Ce, (ii) ZnO:Eu and ZnO co-doped with Ce (0.1mol%, fixed) and Eu 0.1 0.5 and 1.0mol%, variable). These observations imply that the doping levels investigated in the present study did not change the basic wurtzite crystal structure of ZnO. Also, the absence of any independent phase of Ce and/or Eu confirmed their incorporation in ZnO. However, shifting of the peak positions of the XRD diffraction peaks was observed on doping/co-doping ZnO with Ce and Eu. Fig 6.5 shows a typical shifting pattern of (101) diffraction peak.

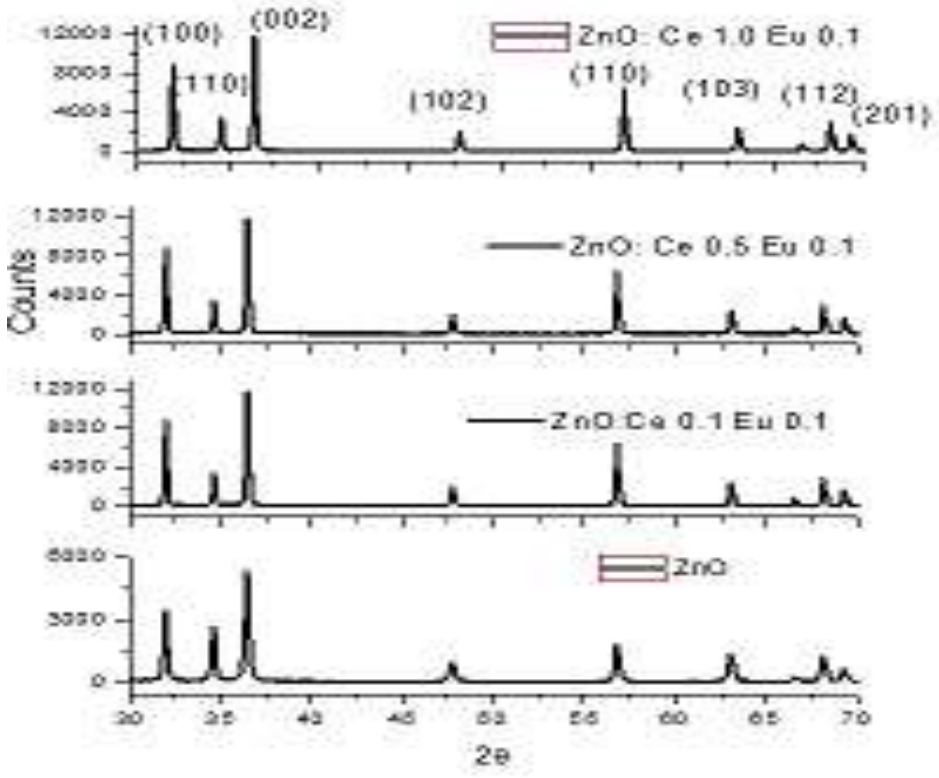

Fig 6.4: Powder XRD spectra of ZnO co doped with Ce (0.1, 0.5, 1.0 mol %, variable) and Eu (0.1 mol, constant).

As seen in this figure (6.5a and 6.5 b), in ZnO (101) peak was observed at $2\Theta = 36.43^{o}$ which shifted to ~36.29^{o} both in ZnO: Ce (0.5mol%) and ZnO: Eu (0.5mol%) implying the induction of lattice distortions of almost equal magnitude on doping. This shift pattern, however, changed when ZnO was co-doped with Ce and Eu; ~0.06^{o} (towards the higher angle) was observed for ZnO co-doped with 0.1mol% Ce and Eu while it marginally decreased with the increase in Ce concentration while keeping Eu concentration constant at 0.1mol% indicating that (i) the lattice stress developed by co-doping was in opposite direction to that of single-doped Ce/ Eu and (ii) the lattice distortion induced by Ce is insignificant compared to that of 0.1mol% Eu.On the hand, the observed peak position for (101) diffraction peak is at $2\Theta = 36.43^{o}$(same as ZnO) for ZnO co-doped with 0.1mole% of Ce and 0.5mol% of Eu; this position shifted to 36.37^{o} (towards lower angle) on changing Eu concentration to 1.0mol% further supporting the

conclusion that Eu compared to Ce is more dominating in lattice distortion inducing process. Similar shift patterns were observed for (002) and (100) diffraction peaks.

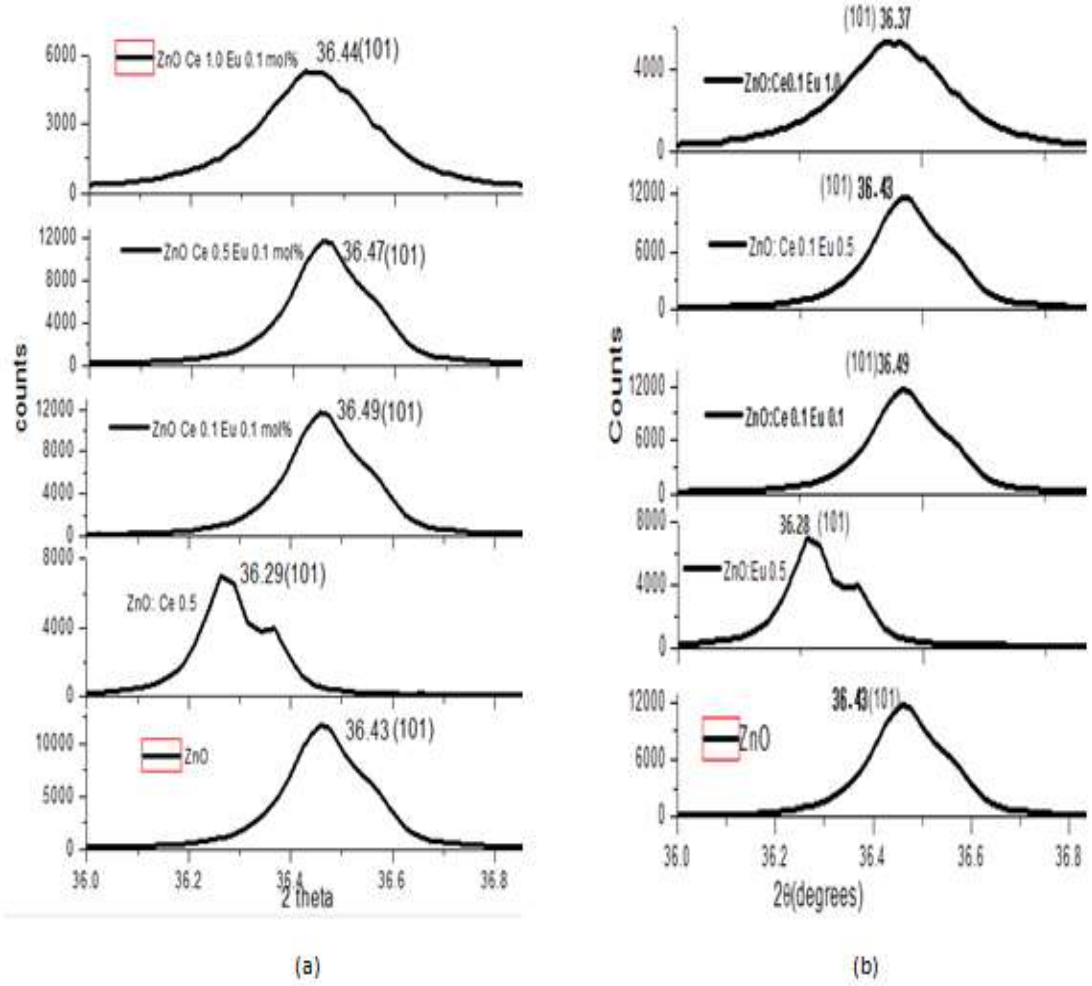

Fig 6.5: Shift in the peak position of (101) (a)ZnO co-doped with Ce(0.1,0.5,1.0 mol%) and Eu(0.1mol%) (b) ZnO co-doped with Ce(0.1 mol%) and Eu(0.1,0.5, 1.0 mol%);peak positions of the same line in ZnO:Ce(0.5mol%) and ZnO:Eu (0.5mol%) are shown for comparison

The calculated (from XRD data) lattice parameters "a" & "c", the ratio "c/a", unit cell volume and crystallite size (calculated using Scherrer formula) of ZnO co-doped with Ce and Euare summarized in Table 6.1.

Table 6.1: Lattice parameters "c" & "a", ratio c/a, unit cell volume and crystallite size calculated from XRD data

Sample with doping concentration (mol%)	Remarks	a (nm)	c (nm)	c/a	Unit cell Volume $(nm)^3$	Crystallite Size (nm)
ZnO	Un-doped	0.3230	0.5171	1.60	0.140	49
ZnO: Ce 0.5	Single doped	03597	05760	1.60	0.193	57
ZnO: Ce 0.1 Eu 0.1	Co-doped	0.3229	0.5169	1.60	0.140	55
ZnO: Ce 0.5 Eu 0.1	Co-doped	0.3229	0.5169	1.60	0.140	54
ZnO: Ce1.0 Eu 0.1	Co-doped	0.3230	0.5170	1.60	0.140	38
ZnO: Eu 0.5	Single doped	0.3597	0.5760	1.60	0.193	57
ZnO: Ce 0.1 Eu 0.5	Co-doped	0.3228	0.5183	1.60	0.141	49
ZnO: Ce 0.1 Eu 1.0	Co-doped	0.3246	0.5191	1.60	0.142	52

The calculated values of "a, c and c/a' (Table 6.2) of ZnO are in reasonably good agreement with the values reported for wurtzite ZnO structure in the literature. On doping, with 0.5mol% Ce or Eu, the values of the both the lattice parameters increased by ~11% while maintaining the 1.60 as ratio indicating that the wurtzite structure of ZnO did not change by the single-doping of Ce and Eu. The ionic radius of Ce(101*pm*) / Eu (95 *pm*) being more than that of Zn (88 *pm*), the increase in the lattice parameters could be due to the incorporation of Ce or Eu at an interstitially or substitutional site in ZnO unit cell. This is further substantiated by the ~35%increase in the unit cell volume of ZnO when doped with Ce or Eu (Table 6.1). On the other hand, lattice parameters, as well as unit cell volume, did not change significantly when ZnO was co-doped with 0.1, 0.5 and 1.0 mol% Ce keeping 0.1 mol% Eu concentration constant; similar observation was noticed in the case of ZnO co-doped with 0.1 mol% Ce and 0.5 mol% Eu. However, in ZnO co-doped with 0.1 mol% Ce and 1.0mol%Eu both "a" and "c" increased marginally (~0.5%) resulting in ~1.5% increase in unit cell volume compared to that of ZnO. Single doping of Ce or Eu in ZnO induced the significant amount of lattice distortion as is

reflected in the significant increase in lattice parameters and unit cell volume. On the other hand, co-doping resulted in almost no significant change both in lattice parameters as well as in unit cell volume implying the surface migration of both Ce and Eu instead of entering the ZnO lattice at interstitial or substitutional site as is the case with single doping.

The crystallite size calculated, as mentioned earlier, from XRD data using Scherrer formula, show interesting variation with dopant concentration; the values in Table 6.1 are the average of the values calculated using three diffraction peaks with (hkl) values (100), (002) and (101). As seen in Table 6.1, the crystallite size of ZnO increased to ~57nm when 0.5mol% of Ce /Eu was single doped in it. This crystallite size almost did not change for ZnO co-doped with 0.1 and 0.5 mol% Ce keeping the Eu doping concentration constant at 0.1mol%. However, the crystallite size of ZnO co-doped with 1.0mol% Ce and 0.1 mol% Eu was found to be ~38nm; lower crystallite size (from Scherrer formula) implies broader diffraction peak which could be attributed to the marginal decrease in the crystallinity with increase in Ce concentration as absence of any significant change in the lattice constants rule out the increase in the induced lattice distortion. On the other hand, the observed crystallite size in ZnO co-doped with 0.1Ce and 0.5mol% of Eu was almost the same as that of ZnO while it increased marginally when Eu concentration was increased to 1.0mol% keeping Ce concentration constant at 0.1 mol% implying that the increase in Eu concentration results in more lattice distortion; further supports the conclusion arrived at while discussing the shifting of the peak positions of the XRD diffraction peaks.

6.2.5 UV-VIS

Room temperature UV-VIS absorption spectra of ZnO and ZnO co-doped with 0.1,0.5 and 1.0 mol% of Ce keeping the concentration of Eu constant at 0.1mol%. As seen in this figure ZnO showed >80% absorption (absorption edge at ~371nm) which changed to ~28% with absorption edge at ~374nm when ZnO was co-doped with 0.1mol % of Ce and Eu; the absorption edge did not change with further increase in Ce concentration while there was decrease in absorption as seen in Fig 6.6. This doping concentration-

dependent decrease in the absorption along with the shifting of absorption edge can be attributed to the creation of non-absorbing impurity states on co-doping of Ce and Eu.

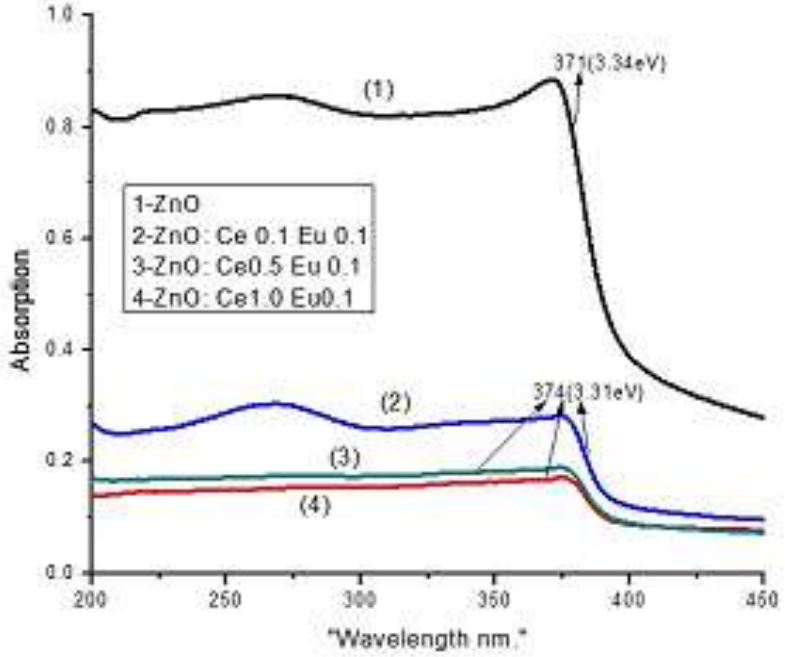

Fig 6.6: Room temperature UV-VIS absorption spectra of ZnO and ZnO co-doped with 0.1,0.5 and 1.0mol% Ce keeping 0.1mol% Eu concentration constant

Almost similar UV-VIS absorption spectral features along with the absorption edges were observed for ZnO co-doped with 0.1, 0.5 and 1.0 mol% Eu keeping Ce concentration constant at 0.1mol%.

6.2.6 Raman Scattering

Room temperature Raman spectrum of ZnO co-doped with 0.1, 0.5 and 1.0 mol% Ce keeping the concentration of Eu constant at 0.1mol% is shown in Fig 7; these spectra were excited with 514.5nm radiation of an Ar-ion laser. As seen in Fig 6.7, the Raman shifts at 332, 381,439,583 and 1145cm^{-1} were observed in ZnO powder samples at room temperature. Co-doping with Ce and Eu increased the over-all intensity of the Raman emission by ~ 20 without changing the spectral position of all the observed.

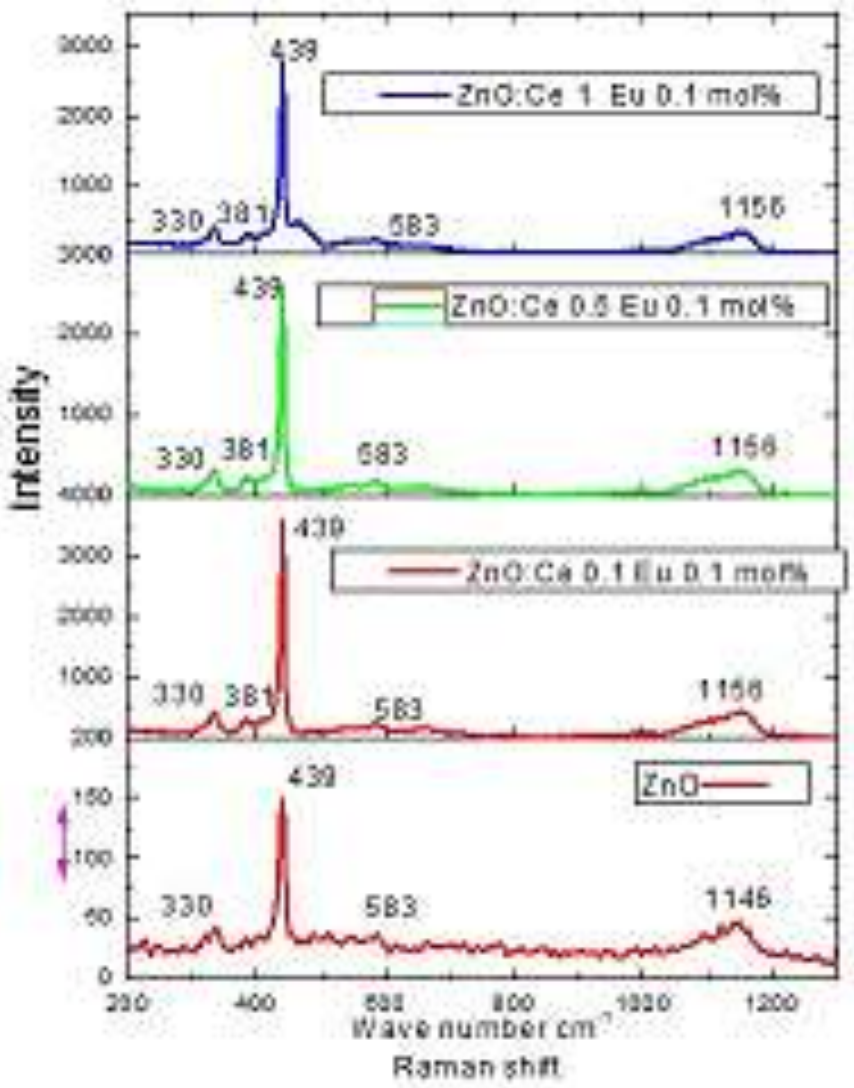

Fig .6.7 : 514.5nm (Ar-ion laser) excited room temperature Raman spectrum of ZnO co-doped with 0.1, 0.5 and 1.0 mol% of Ce keeping Eu concentration constant at 0.1mol%.

Raman shifts except that of 1145 cm^{-1} Raman line which shifted to 1156 cm^{-1}; this observed shift of ~11cm^{-1} did not show any dependence on the dopant concentration. On the other hand, the intensity variation of the Raman emission showed dopant concentration dependence as shown in Fig 6.8 where strongest peak intensity of observed Raman shift (439cm^{-1}) has been plotted as a function of various co-dopant concentrations. The peak intensity of 439cm^{-1} Raman shift in ZnO, as seen in Fig 6.8, changed from ~172 (arb.units-AU)) to~3676AU when it was co-doped with 0.1mol% of

Ce and Eu. However, it decreased to about ~2600AU when Ce concentration was increased to 0.5/1.0 mol% keeping Eu concentration constant at 0.1mol% (Fig 6.8 (a)). On the other hand, in a case of ZnO co-doped with 0.1 mol% of Ce and 0.5 mol% of Eu,

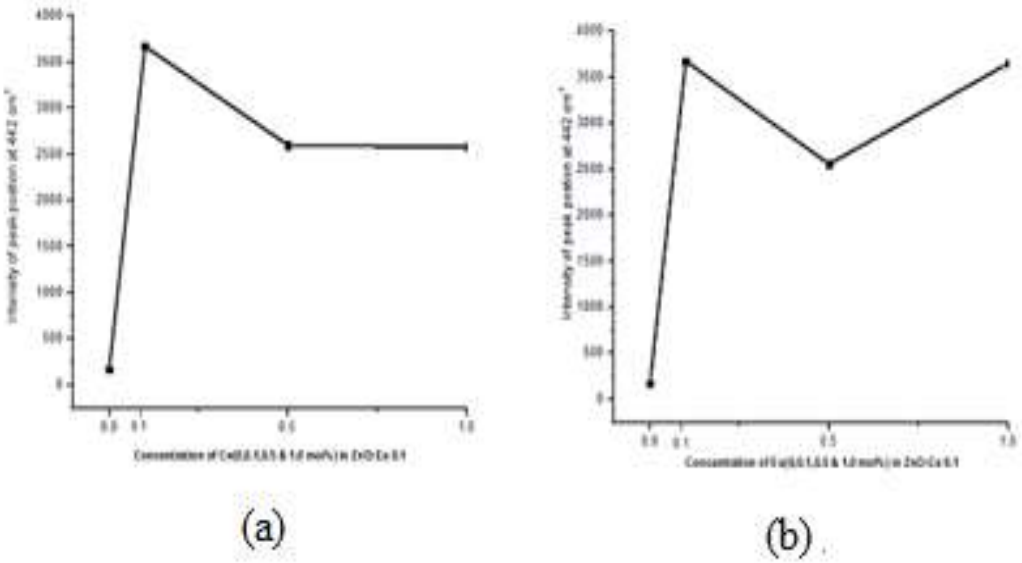

Fig.6.8: Concentration dependence of the peak intensity of 439 cm^{-1} Raman shift in ZnO co-doped with Ce and Eu.

the peak intensity was almost same as that of ZnO co-doped with 0.5 mol% of Ce and 0.1mol% of Eu while it increased significantly when Eu concentration was increased to 1.0mol%. Table 6.2 summarizes the associated phonon modes assigned with the help of the literature.

Raman scattering involving one, two and more than two (multi) phonon processes have been observed in ZnO. The expected shifts in one phonon Raman scattering are < 600cm^{-1} with a gap between the acoustic and optical branches from 270 to 370 cm^{-1}. Raman shifts based on two-phonon differences also are expected to be <600 cm^{-1} while higher than 600 cm^{-1} shifts are attributed to the "two-phonon sums" and/or multi phonon processes. The observed Raman shifts (Fig 6.7) at 381,439 and 583 cm^{-1} are due to one phonon processes while multi-phonon processes could be responsible for the relatively broader shift peaking ~1145cm^{-1}. On the other hand, the 330cm^{-1} shift could be the result of "two-phonon difference" (Table 6.2).

Table 6.2: Phonon modes associated with the observed Raman shifts

Observed Raman shift cm^{-1}	Associated phonon mode
330	E_2 (high)-E_1 (low)
381	A_1
349	E_2 (high)
583	E_1
1145	2xA_1 (low)

The observed increase in the intensity of Raman scattering on co-doping with Ce and Eu can be attributed to the increase in defects and strain in ZnO lattice. Maximum change in intensity was observed with 0.1mol% Ce and Eu implying that maximum lattice distortion produced by this co-doping combination. Further increase in Ce concentration keeping Eu concentration at 0.1mol% resulted in decrease in Raman intensity. This could be attributed to the reduction in the induced lattice distortion due to the migration of Ce to the surface. Similarly, the observed reduction in intensity with Ce 0.1mol% and Eu 0.5mol% could be attributed to the surface migration of Eu. However, the significant increase in the Raman intensity with 1.0mol % of Eu keeping Ce at 0.1mol% implies the increase in lattice distortion with further increase in Eu concentration further supporting the conclusion arrived at from XRD data analysis.

The multi phonon nature of the Raman shift of ZnO at 1145 cm^{-1} makes it very sensitive to the lattice train; this mode shifted by ~11cm^{-1} when ZnO was co-doped with 0.1mol% Ce and Eu. However, an absence of any significant dopant concentration dependence of the observed shift implies that further increase in dopant concentration resulted in the marginal increase in lattice distortion was concluded from XRD data as well.

6.2.7 Photoluminescence (PL)

Room temperature photoluminescence (PL) of the powder samples was excited with 280 and 380nm radiation from a Xe lamp. Several sharp emission peaks in a blue-green region were observed when excited with 380nm radiation while broad emission peak

around 510 nm was observed when excited with 280 nm radiation. The analysis of this PL data is presented in the following sections.

6.2.7.1 PL excited by 380nm radiation

Typical PL spectra (excited with 380nm radiation) of ZnO co-doped with 0.1, 0.5 and 1.0mol% of Eu keeping the Ce concentration constant at 0.1mol%, are shown in Fig 6.9. Three well-known PL peaks at 422, 484 and 518nm were observed in ZnO when excited with 380nm radiation; these peaks, as mentioned earlier, are attributed to defect states.On co-doping, with Ce and Eu the spectral positions of these PL peaks remained unchanged while intensity showed concentration-dependent variation as summarized in Table6.3.

The main observations regarding the concentration dependence of intensity (Table 5.3) are as follows:

i. In ZnO the peak intensity of 422nm PL peak was maximum while it is minimum for 484nm peak
ii. On co-doping ZnO with 0.1mol% Ce and Eu, there was significant change in the peak intensity of all the three PL peaks; it was (~39%) for 518nm peak, 35% for 484nm peak and 14% for 422nm PL peak implying that 0.1mol% co-doping of Ce and Eu induced lattice distortions favoring the visible emission in general and the "blue-green" in particular.
iii. A significant decrease in the peak intensity was observed in ZnO co-doped with 0.5 and 1.0mol% Ce while keeping the Eu concentration constant at 0.1mol% level. This quenching of visible emission was due to increase in Ce concentration; it was reported earlier also.
iv. The observed peak intensity of ZnO co-doped with 0.1 mol% Ce and 0.5 mol% Eu was smaller compared to that of ZnO; it was ~19% less for 422nm peak, ~16% less for 484nm peak and 21% less for 518nm PL peak showing that the 0.5 mol % Eu co-doped with 0.1 mol% Ce enhances the overall intensity of the visible emission.

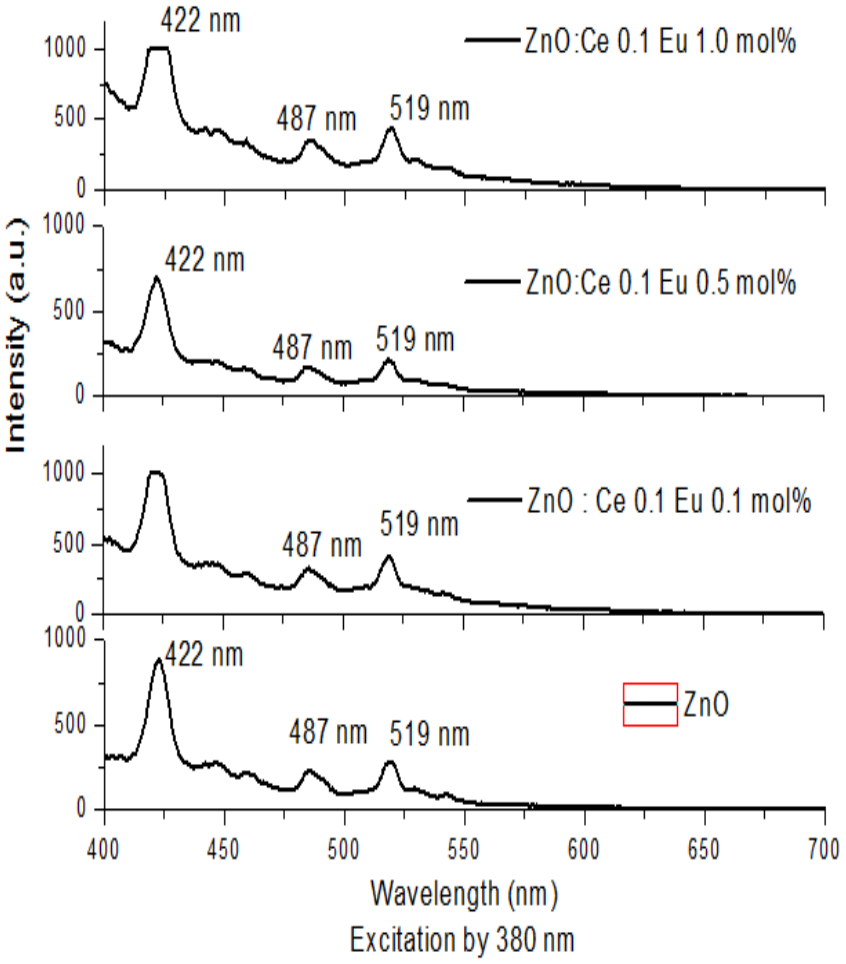

Fig 6.9: Typical room temperature 380nm excited PL of ZnO co-doped with 0.1, 0.5 and 1.0 mol% of Eu keeping the Ce concentration constant at 0.1mol%.

Table 6.3: Dopant concentration dependence of 380nm excited PL intensity (arbitrary units, AU)

Sample (mol %)	Peak intensity 422nm	Peak intensity 484nm	Peak intensity 518nm
ZnO	899	232	310
ZnO:Ce 0.1 Eu 0.1	1027 (+14%)	360 (+35%)	432 (+39%)
ZnO: Ce 0.5 Eu 0.1	266 (-70%)	88 (-62%)	104 (-66%)
ZnO: Ce 1.0 Eu 0.1	232 (-74%)	80 (-65%)	96 (-69%)
ZnO: Ce 0.1 Eu 0.5	725 (-19%)	195 (-16%)	242 (-21%)
ZnO: Ce 0.1 Eu (.0	757 (-16%)	366 (+58%)	457 (+47%)

v. In case of ZnO co-doped with 0.1 mol% Ce and 1.0 mol% Eu the peak intensity of 422nm continued to be less (~16%) compared to ZnO while it was more for other two PL peaks; the peak intensity is ~58% more for 484nm peak while for the other peak (518nm) the observed increased was ~47% implying that 1.0 mol% Eu co-doped with 0.1 mol% Ce almost doubled the intensity of "blue-green" emission of ZnO.

6.2.7.2 PL excited by 280 radiations

Typical 280nm excited room temperature spectra of ZnO co-doped with Ce and Eu are shown in Fig 6.10. As seen in this figure, broad emission peaking around 510nm was observed; its intensity showed dopant concentration dependence which, along with the full width at half maximum (FWHM), chromaticity colour coordinates (CIE) and cumulative colour temperature (CCT), is summarized in Table 6.4.

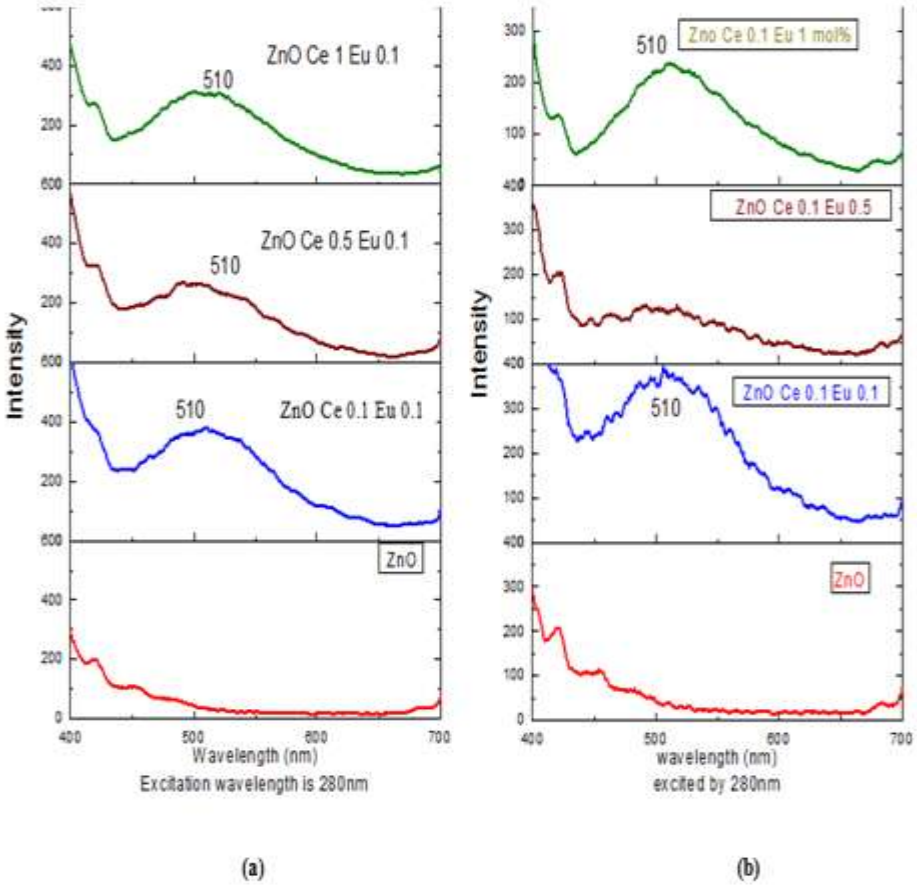

Fig 6.10: Typical 280nm excited PL spectra of ZnO co-doped with(a) 0.1, 0.5 and 1.0mol% Ce keeping concentration of Eu constant at 0.1mol%, (b) 0.1, 0.5 and 1.0mol% Eu keeping concentration of Ce constant at 0.1mol%.

The observed PL emission from ZnO co-doped with 0.1 mol% of Ce and Eu was about ~124nm which decreased to ~110nm for all other samples (Table 6.4) except ZnO co-doped with 0.1mol% of Ce and 0.5mol% of Eu. On the other hand, the integrated intensity of the PL (Fig. 6.10) is maximum for ZnO co-doped with 1.0mol% of Ce and 0.1mol% Eu. Interestingly next most intense PL emission was observed in ZnO co-doped

Table 6.4: Dopant concentration dependence of the intensity, full width at half maximum (FWHM), chromaticity colour coordinates x,y (CIE) and correlated colour temperature (CCT) of the room temperature PL emission excited by 280nm radiation

Co-doping concentration (mol%) of Ce and Eu in ZnO	FWHM (nm)	Integrated intensity ($x10^3$) arbitrary units)	CIE (x,y)	CCT (K)
Ce 0.1,Eu 0.1	124	15.55	0.28,0.29	10213
Ce 0.5, Eu 0.1	110	4.87	0.27,0.27	12940
Ce 1.0, Eu 0.1	110	37.49	0.28,0.29	9559
Ce 0.1, Eu 0.5	104	6.14	0.28,0.28	11690.
Ce 0.1, Eu 1.0	111	33.91	0.29,0.30	8842

with 0.1mol% Ce and 1.0mol%Eu. The weakest emission was from ZnO co-doped with 0.5mol% of Ce and 0.1mol % of Eu which increased marginally on interchanging the doping concentrations of Ce and Eu. The calculated chromaticity colour coordinates of the PL emission from ZnO co-doped with 0.1mol% of Ce and 1.0mol% of Eu are 0.29 and 0.30 as shown in Fig.6.11, which are very close to those of an ideal white light source (0,33 and 0.33) indicating the usefulness of this material for the realization of a white light source.

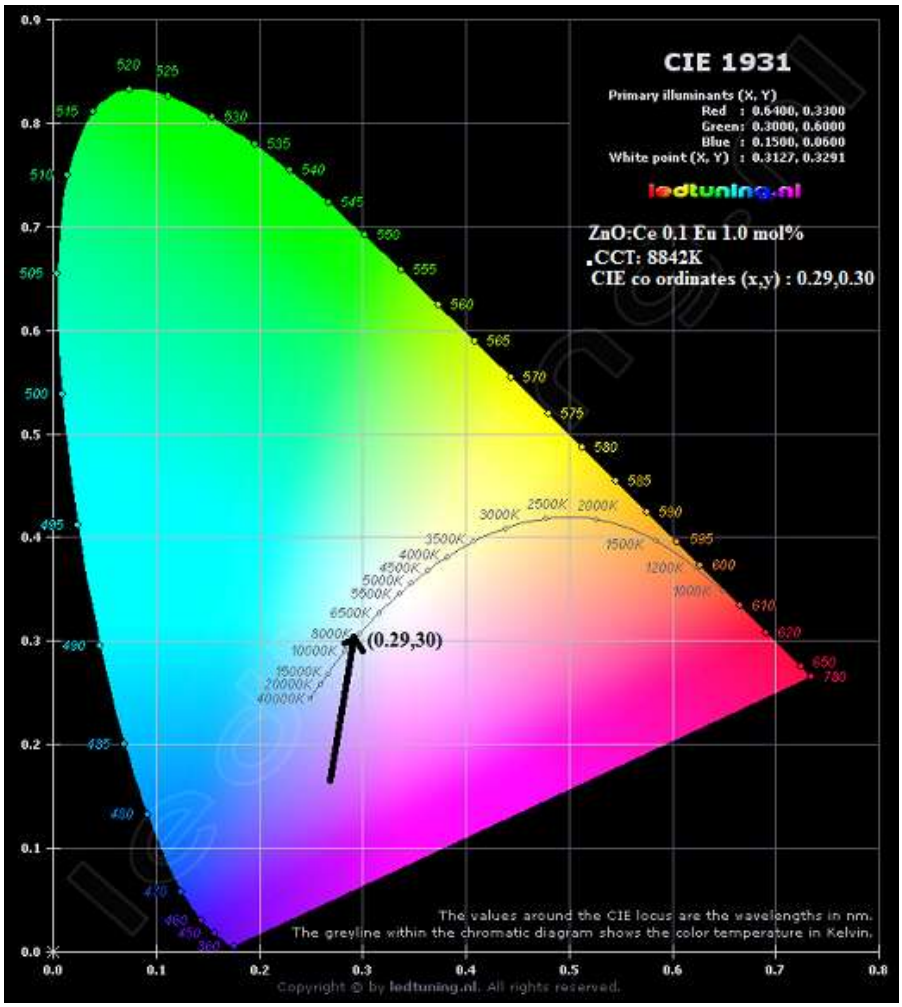

Fig 6.11: Chromaticity coordinates x & y for 280 nm excited emission from ZnO:Ce 0.1Eu 1.0 mol% The calculated chromaticity coordinates x and y, as seen in Fig 6.10 are x=0.29 and y=0.30 indicating the potential of this material in realization of optical sources/displays

Reference

[1] Murugadoss,Jayavel R and Kumar M R (2015) *Super lattice Microst* 82: 538-550

Chapter 7

ZnO nano phosphor co-doped with Ce, Eu and Tb

7.1 Introduction

Co-precipitation method, as described in Chapter 3, was used to prepare the ZnO nano phosphor co-doped with Ce, Eu and Tb. The samples ,thus, prepared were sintered in air (max temperature 700^{o}C) using a home- made (Chapter 3) muffle furnace fitted with a temperature controller which could control the temperature within ±1^{o}C. The dopant concentrations used were 0.1, 0.5 and 1.0 mol %; eighteen samples were prepared by permutations of these concentration levels. The powder samples, thus, prepared were characterized with EDX, FTIR, XRD, SEM/TEM and optical spectroscopy techniques. Photoluminescence investigation showed a broad emission band in the visible region whose intensity and full width at half maximum showed dopant concentration dependence. Chromaticity color analysis of this visible emission was carried out to assess the potential of these materials in the realization of the white light sources. This investigation, to the best of our knowledge, is the first attempt where ZnO was doped with three rare-earth elements.

7.2 Results and discussion

7.2.1EDX

Typical EDX spectrum of ZnO co-doped with Ce (0.5mol %), Eu (0.5mol %) and Tb (1.0mol %) sintered at 700^{o}c, is shown in Fig 7.1

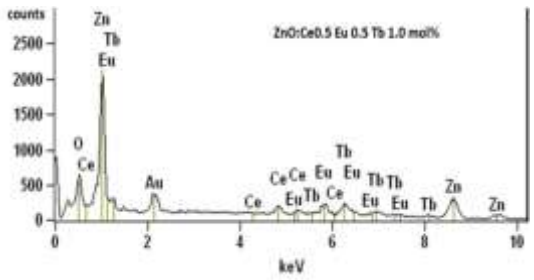

Fig 7.1: Typical EDX spectrum of ZnO co-doped with Ce, Eu and Tb

Prominent peaks due to Ce, Eu and Tb along with those of Zn and O can be clearly seen in Fig 7.1 confirming the doping of these dopants in ZnO. The peak assigned to Au is due to gold sample holder used for recording the EDX spectrum.

Similar spectra were observed with the ZnO powder samples co-doped with other permutations of the dopants.

7.2.2 SEM/TEM

SEM/TEM images were recorded to investigate the nanostructure nature of the synthesized samples. Fig 7.2 shows a typical SEM image of the ZnO co-doped with Ce, Eu and Tb. The sample, as seen in Fig 7.2 was composed of spherically-shaped particles along with some non-spherical large size grains which could be due to agglomeration and/or strain induced by Ce, Eu and Tb doping as discussed in following sections. Similar images were recorded for other co-doping concentration combinations. The nanostructure and spherical nature of the powders of ZnO co-doped with Ce, Eu and Tb was further supported by TEM images shown in Fig 7.3.

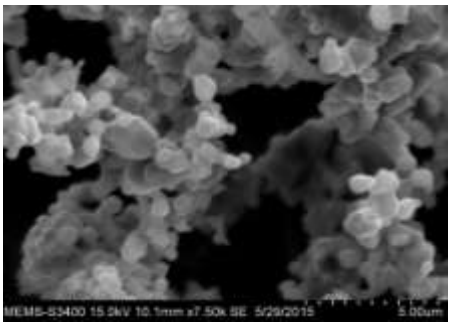

Fig.7.2: Typical SEM image of the 0.5 mol% of Ce, Tb and 1.0 mol% of Eu co-doped in ZnO.

Fig 7.3: Typical TEM image of the 0.5 mol% of Ce, Tb and 1.0 mol% of Eu codoped in ZnO.

7.2.3 FTIR

Change, if any, in the molecular structure of the ZnO on co-doping with Ce, Eu and Tb was investigated by FTIR spectroscopy. Typical spectra (0-4000cm^{-1} region) of ZnO co-doped with 0.5mol% of Ce, Eu and Tb recorded in air using a KBr pallet (Chapter 3) is shown in Fig 7.4; both un-doped as well as doped ZnO were sintered at 700^{o}C.

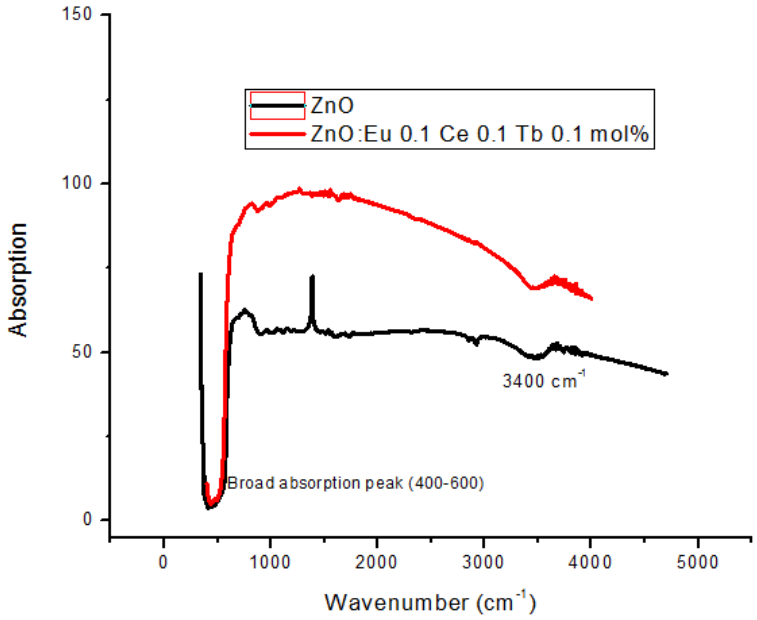

Fig 7.4: FTIR spectra of ZnO and ZnO co-doped with 0.5mol% of Ce, Eu and Tb

All the main spectral features, as seen in Fig 7.4, of ZnO and doped ZnO were similar implying that the dopants did not change the basic structure of ZnO. The absorption peak in 400-600cm^{-1}region was due to metal oxygen bond (Zn-O, Eu-O, Ce-O, and Tb-O) vibrations while relatively weak absorption at 3500 cm^{-1} was due to water present in the atmosphere. Similar features were seen in the FTIR spectra of ZnO co-doped with other concentration combinations of Ce, Eu and Tb.

7.2.4 XRD

XRD spectra of ZnO co-doped with 0.5mol % Ce, 0.5mol% Eu and 1.0mol% Tb along with that of ZnO are shown in Fig. 7.5; both the powder samples were sintered in air at 700^{o}C. All the spectral features, as seen in this figure, of the XRD spectrum of doped ZnO were identical to that of ZnO; the XRD pattern of doped ZnO could be indexed using JCPDC File No. 36-1451 implying that the doping levels investigated in the present study did not change the basic wurtzite crystal structure of ZnO. Also, the absence of any independent phase of Ce, Eu or Tb confirmed their incorporation in ZnO. Similar observations resulted from the XRD analysis of other doping concentration combinations.

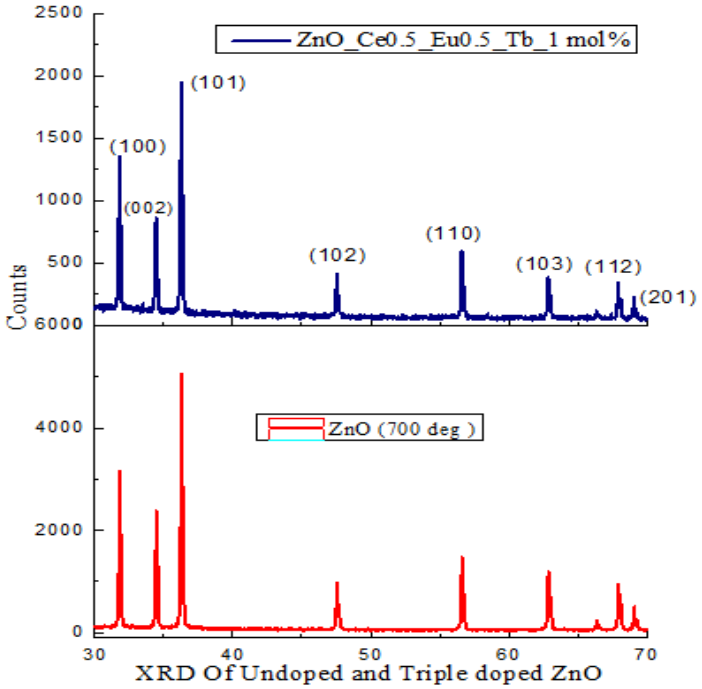

Fig7.5: Powder XRD spectra of ZnO and ZnO co-doped with 0.5mol % Ce, 0.5mol% Eu and 1.0mol% Tb; both the samples were sintered at 700^{o}C

However, the peak positions of the XRD diffraction peaks did shift on doping as seen in Fig 7.6 where the peak position of the diffraction peak with (hkl) (101) of ZnO is compared with that of ZnO doped (single) with 0.5mol% of Ce, Eu and Tb along with that of ZnO co-doped with 0.5mol% of Ce and Eu and 1.0mol% of Tb,

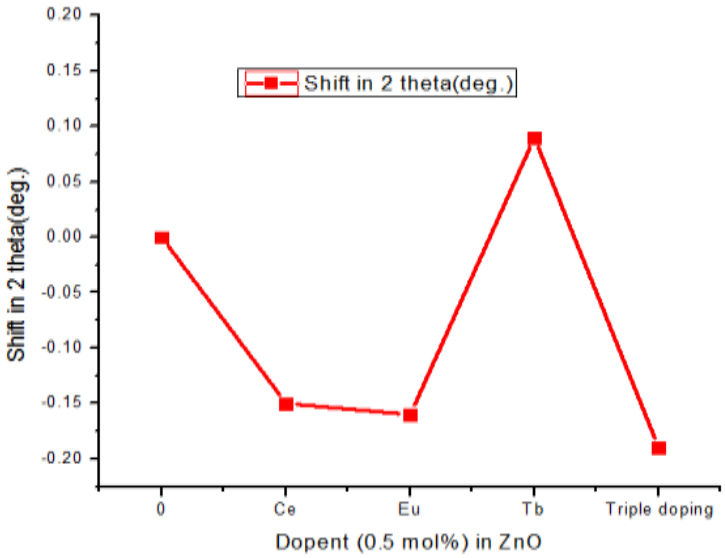

Fig 7.6: Comparison of the shift in the peak position of (101) diffraction peak of ZnO with that single and co-doped ZnO

As seen in Fig 7.7, the peak position of (101) diffraction peak shifted by 0.15^{o} (towards the lower angle) when doped with 0.5mol% Ce. This peak increased marginally towards lower angle in ZnO doped with 0.5mol% Eu. However, when doped with 0.5mol% Tb, the shift was ~0.10^{o} but towards higher angle showing that the strain induced by doping of Ce and Eu is in the opposite direction to that of Tb. On the other hand, ZnO when co-doped with Ce, Eu and Tb (Fig 7.7), the peak shifts by ~0.20^{o} towards the lower angle implying that co-doping induced lattice distortion which produced maximum strain as compared to that of Ce, Eu and Tb doping; the direction of this strain being in the same direction as that of Ce and Eu while in a direction opposite that of Tb.

The variation of the crystallite size (calculated from XRD data using Scherrer equation) as a function of the nature of dopant is shown in Fig 7.7 The crystallite size, as seen in

Fig 7.7 for ZnO was about 34nm which changed to about 56nm when 0.5 mol % Ce (single) was doped in it. A marginal increase was observed when Ce doping was replaced by 0.5mol% of Eu implying that Ce or Eu when doped in ZnO were incorporated in substitutional or interstitial sites in its lattice; the increase in the crystallite size could be due to higher ionic radii of Ce (115pm) and Eu (131pm) as compared to Zn(88pm).

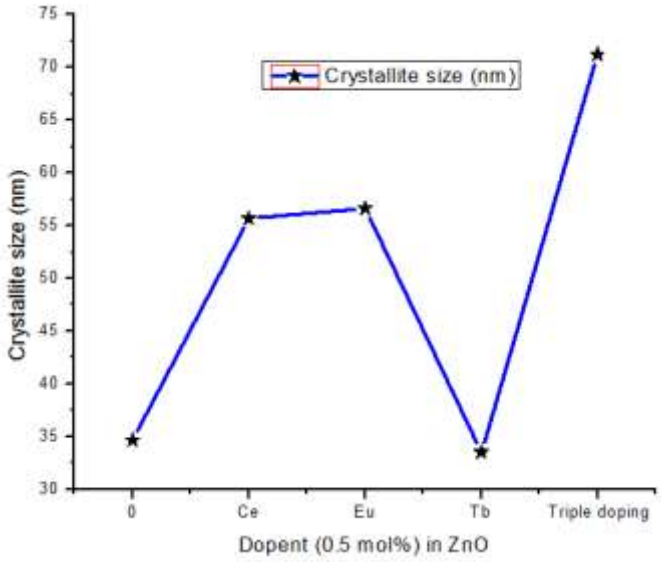

Fig 7.7: Variation of the crystallite size as a function of single doped and co-doped Ce, Eu and Tb

On the other hand, on doping with 0.5mol% of Tb (106pm) in ZnO the crystallite size was almost equal to ZnO which could be due to surface migration of Tb at concentration >0.1mol% widely reported in literature. Tb when migrated to surface induced "hydrostatic like pressure" on ZnO unit cell resulting in its shrinking. However, the observed crystallite size of the ZnO co-doped with Ce, Eu and Tb, as seen in Fig 7.8, increased to about 73 nm. This increase could be due to substitutional or interstitial incorporation of the three dopants in the ZnO lattice. This is further supported by the increase in lattice constants as seen in Table 7.1.

Table 7.1: Comparison of lattice constants, ration of lattice constants and unit cell volume of ZnO, ZnO: Ce 0.5mol %, ZnO: Eu 0.5mol %, ZnO: Tb 0.5 mol % and ZnO co-doped with 0.5 mol% of Ce, Eu and 1.0 mol% Tb.

Samples (mol %)	a (nm)	c(nm)	c/a	Volume (nm^3)
ZnO	0.32296	0.51708	1.60	0.140
ZnO: Ce 0.5	0.35973 (11%)	0.57599 (11%	1.60	0.194
ZnO: Eu 0.5	0.35974 (11%)	0.57602 (11%)	1.60	0.194
ZnO: Tb 0.5	0.32204 - (0.2%)	0.51644 - (0.1%)	1.60	0.139.
ZnO: Ce 0.5 Eu 0.5Tb 1.0	0.36020 (11.5%)	0.62388 (20.5%)	1.73	0.210

The lattice constants, as seen in Table 7.1, "a" and "c" increased by ~11% when ZnO was single doped with 0.5mol% of Ce or Eu as well as when co-doped with Ce, Eu and Tb while no change was observed on doping with 0.5mol% Tb. However, the "c/a" ratio which should be 1.60 for a hexagonal crystal structure was observed for ZnO single doped with Ce, Eu and Tb while on co-doping with Ce, Eu and Tb, the value of this ratio (Table 7.1) changed to 1.73 indicating a significant deviation from the hexagonal structure. This was further confirmed by the change in unit cell volume on cooping which increased by 50% (Table 7.1) when ZnO was co-doped with Ce, Eu and Tb.

7.2.5 Photoluminescence (PL)

PL emission at room temperature of ZnO co-doped with Ce, Eu and Tb was investigated by 380, 300 and 280nm radiation from a Xe lamp. On excitation with 380nm radiation, relatively two sharp peaks in the blue-green region were observed while broad emission in 400-700 nm regions was observed when excited with 300 and 280nm radiation. The spectral features of all the observed emissions showed almost no concentration dependence while intensity of the emission showed a significant concentration dependence which was discussed in the following sections. Also, chromaticity colors coordinated of the broad emission were calculated to assess the suitability of the various doped ZnO for the realization of the light sources.

7.2.5.1 PL excited with 380nm radiation

Typical spectra excited with 380nm radiation are shown in Fig7.8.

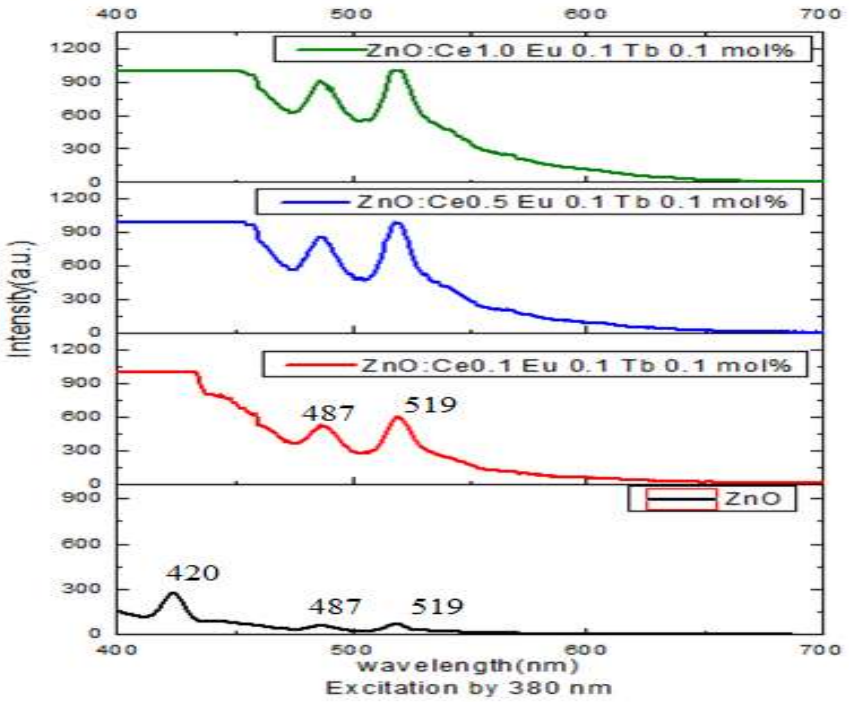

Fig 7.8: 380nm excited typical PL spectra of ZnO co-doped with Ce (0.1, 0.5, 1.0mol%, variable), Eu (0.1mol%, constant) and Tb (0.1mol%, constant).

As seen in Fig 7.8, ZnO emits at 420, 487 and 519nm when excited with 380nm radiation; this was well known emission pattern of ZnO attributed to oxygen vacancies. On co-doping with 0.1mol% of Ce, Eu and Tb, though the spectral features did not change yet there was a significant increase in the emission intensity; huge change in case of the emission centered at 420nm while the intensity of the other two emission peaks (487 and 519nm) increased 3-4times when compared with that of ZnO. This observed increase in emission intensity could be attributed to the creation of more defects (oxygen vacancies) by dopants. This increase in emission intensity continued with the increase in Ce concentration while keeping the concentration of Eu and Tb constant at 0.1mol% which also could be due to increase in defects with the increase in Ce concentration. Almost similar results were observed with other co-dopant concentrations.

7.2.5.2 PL excited with 300 and 280nm radiation

Broad emission, as mentioned earlier, was observed when ZnO co-doped with Ce, Eu and Tb was excited with 300 and 280nm radiation. Typical emission spectra of ZnO co-doped with 0.5mol% of Ce, Eu and Tb is shown in Fig 7.9 where spectra of ZnO as well as ZnO single doped with 0.5mol% of Ce/Eu/Tb are shown for comparison.

Broad emission centered around ~510nm, as seen in Fig 7.9, is observed in ZnO, ZnO; Ce (0.5 mol%), ZnO; Eu (0.5mol%), ZnO ; Tb (0.5mol%) and ZnO co-doped with 0.5mol% of Ce, Eu and Tb. Almost similar spectra was seen when excited with 280nm radiation. However, the intensity and the full width at half maximum (FWHM) of the observed emission depended on the nature of the dopants as seen in Fig 7.9 where integrated area under the emission spectrum in the visible region had been plotted as a function of the chemical nature of the single dopant as well as co-dopants; Fig 7.10a shows the variation in the emission spectra excited by 280nm radiation while the variation in 300nm excited emission is shown in Fig 7.10b.

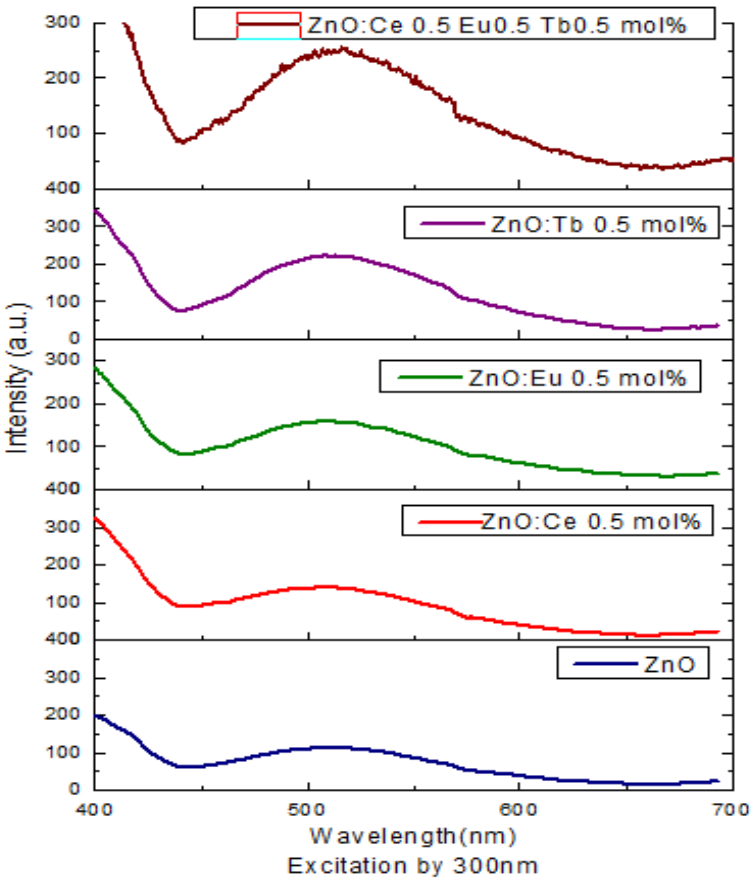

Fig 7.9: Room temperature photoluminescence excited by 300nm radiation ZnO, 0.5mol % Ce: ZnO, 0.5 mol % Eu: ZnO, 0.5mol % Tb: ZnO, (e) ZnO co-doped with 0.5mol% of Ce, Eu and Tb

As seen in Fig 7.10, the nature of variation of the intensity (integrated area under the emission profile in the visible region) as well as that of FWHM was qualitatively similar for both 280 and 300nm excited emission; the intensity was maximum for 280nm excited emission while FWHM was the widest for Eu doped ZnO; FWHM of the emission from ZnO co-doped with Ce, Eu and Tb excited by 300nm was marginally better than that of the emission excited by 280nm radiation.

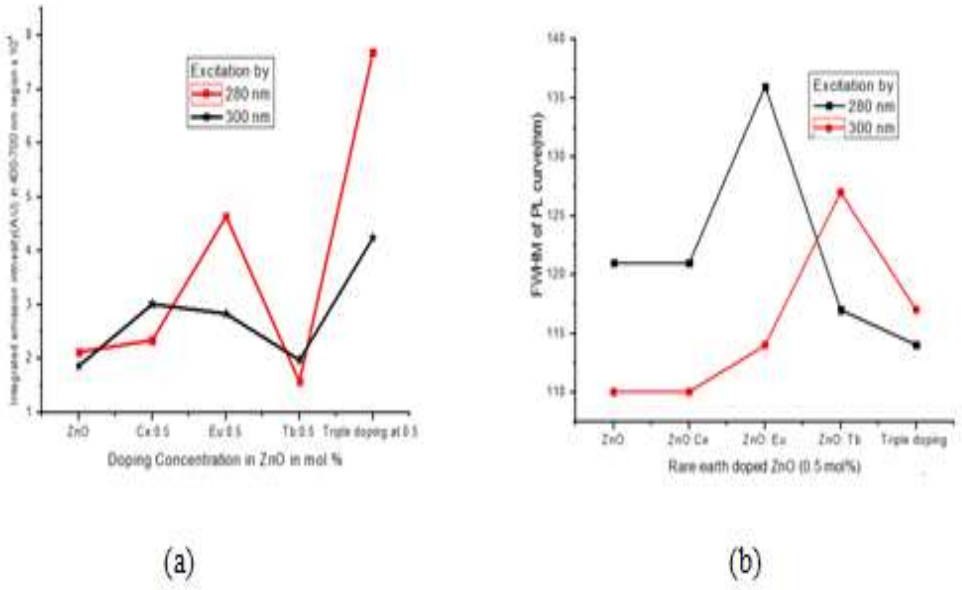

Fig 7.10 : (a) Integrated emission intensity and (b) FWHM of the emission: as a function of dopants in ZnO for 280 and 300nm excitations

Typical emission spectra excited by 280 and 300nm is shown in Fig 7.11(a,b) where Tb concentration varied (0.1, 0.5 and 1.0mol%) keeping that of Ce and Eu constant at 0.1mol%. As seen in this figure, broad emission peaking was observed in both ZnO as well in ZnO co-doped with Ce, Eu and Tb. When excited with 280nm, radiation emission at 420nm was observed in addition to the relatively broad emission in the visible region while no emission at 420nm was observed when excited with 300nm radiation; only broad emission in visible range was observed. The intensity of the observed emission (Fig 7.11) varied with the dopant concentration. The maximum emission intensity was observed in ZnO co-doped with 0.1mol% Ce, 0.1mol% of Eu and 0.5mol% Tb when excited with 300nm radiation while minimum emission intensity (less than ZnO) was observed in 0.1mol% Ce, 0.1mol% of Eu and 1.0mol% Tb doped ZnO when excited with same ((300nm) radiation. All these observations are displayed in Fig 7.12 where integrated area under the emission curve in visible region has been plotted as a function of Tb concentration keeping the concentrations of Ce and Eu fixed at 0.1mol%.

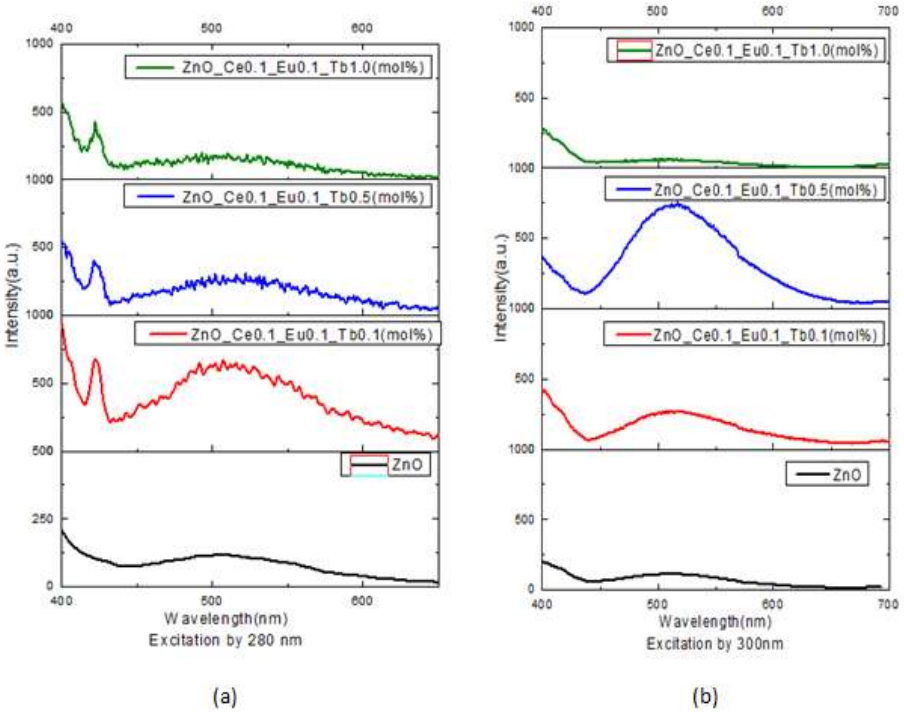

Fig 7.11 : (a) 280nm radiation and (b) 300nm radiation excited PL in ZnO co-doped with Ce (0.1mol% constant), Eu (0.1mol% constant and Tb (0.1, 0.5 and 1.0mol% variable)

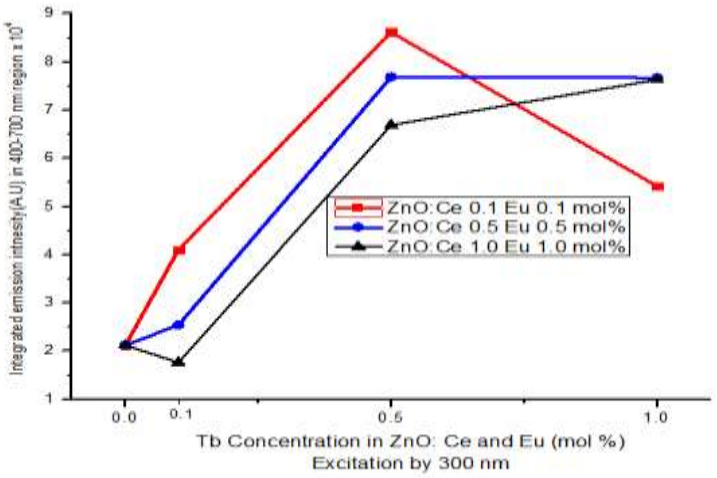

Fig 7.12: Variation of the intensity of 300nm excited PL as a function of Tb concentration

The intensity of the visible emission (Fig 7.12), as concluded earlier, was maximum for ZnO co-doped with 0.1mol % Ce, 0.1mol% Eu and 0.5mol% of Tb when excited with 300nm radiation. Fig 7.13 shows the intensity variation with the Eu concentration while keeping the concentrations of Tb and Ce as parameters; this figure also shows the PL intensity (integrated area under the emission cure in the visible region) for nine samples.

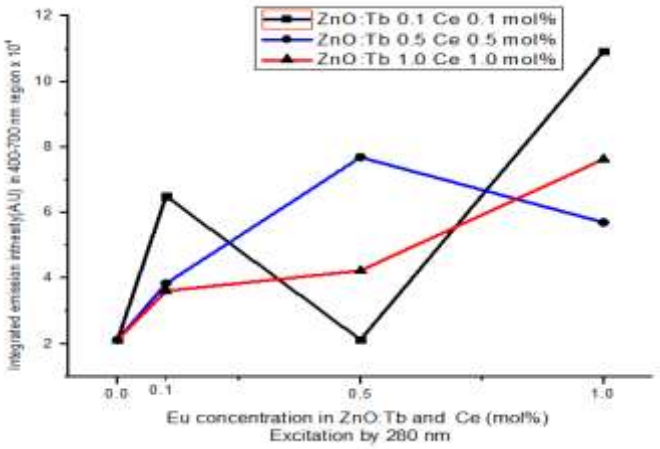

Fig 7.13: Variation in the intensity (integrated area under emission curve in the visible region) for various dopant concentration combinations.

The conclusions drawn from Fig 7.13 are

i. The intensity of the PL for all the co-doped samples was more than that of ZnO.
ii. The minimum intensity was observed for ZnO co-doped with 0.1 mol% Ce, 0.5 mol% Eu and 0.1 mol% Tb.
iii. The maximum intensity was observed for ZnO co-doped with 0.1 mol% Ce, 1.0 mol% Eu and 0.1 mol% Tb.
iv. The intensity of ZnO co-doped with 1.0 mol% of both (Ce) and Tb increased with the increase in(Eu) concentration.
v. The intensity of the ZnO co-doped with 0.5mol% of both (Ce) and Tb showed a decrease when (Eu) concentration was increase from 0.5 mol% to 1.0 mol%

All these variations were due to different amount and/or nature of the distortion induced in the ZnO lattice by the dopants.

7.2.5.3 Chromaticity color coordinates

A light source, as discussed in Chapter 1, was characterized chromaticity color coordinates (x and y) which indicated the expected color (as perceived by a normal human eye) of its emission. To calculate these coordinates, a "color space diagram" (Chapter 1) was constructed from the emission spectrum. This 'appearance of the color' of any emission was also expressed in terms of "correlated color temperature (CCT)" which was expressed in terms of Kelvin (K). In the present study, visible emission from 19 samples of ZnO co-doped with various concentration combinations of Ce, Eu and Tb (0.1, 0.5 and 1.0 mol%) was used to calculate both "x and y" as well as CCT and the results are summarized in Table 7.2

The values of the chromaticity color coordinates "x and y" for the white light (Chapter 1) are: x= 0.33 and y=0.33; the materials with the values reasonably close to these values for white light had been indicated as bold digits in Table 7.2 . The calculated values of the 280nm excited emission from ZnO co-doped with 0.5mol% of Ce, Eu and Tb are: x=0.32, y= 0.32, CCT= 6468K which is the best among all the materials listed in Table 7.2. When same material was excited with 300nm radiation the emission which was observed to have almost identical spectral features of the visible emission as that of 280nm excited one both the color coordinates as well as CCT changed (Table 7.2) implying that excitation radiation plays an important role in the realization of the light sources. The color space diagram of ZnO co-doped with 0.5mol% of Ce, Eu and Tb excited with 280nm is shown in Fig. 7.14

Table7.2: Chromaticity color coordinates (x and y) and correlated color temperature (CCT) of ZnO co-doped with various concentration combinations of Ce, Eu and Tb.

Ce mol%	Eu mol%	Tb mol%	280nm excitation		300nm excitation	
			CCT(K)	CIE	CCT(K)	CIE
0.0	0.0	0.0	10526	0.25,0.33	9763	0.28,0.29
0.1	0.1	0.1	8346	0.29,0.30	7717	0.30,0.31
0.1	0.1	0.5	8172	0.29,0.31	7988	0.29,0.30
0.1	0.1	1.0	11849	0.27,0.28	12793	0.27,0.27
0.5	0.5	0.1	8079	0.29,0.30	7628	0.30,0.31
0.5	0.5	1.0	8455	0.29,0.31	9869	0.28,0.29
1.0	1.0	0.1	8079	0.29,0.30	7969	0.29,0.30
1.0	1.0	0.5	7896	0.29,0.31	7968	0.29,0.30
1.0	1.0	1.0	7632	0.29,0.30	7977	0.29,0.30
0.1	0.1	0.1	8346	0.29,0.30	7717	0.30,0.31
0.5	0.1	0.1	5520	0.33,0.34	9869	0.28,0.29
1.0	0.1	0.1	7547	0.29,0.31	7717	0.30,0.31
0.1	0.5	0.5	8266	0.29,0.30	7897	0.29,0.31
0.5	**0.5**	**0.5**	**6468**	**0.32,0.32**	**7988**	**0.29,0.30**
1.0	0.5	0.5	7623	0.29,0.30	9869	0.28,0.29
0.1	1.0	1.0	8266	0.29,0.30	7896	0.29,0.31
0.5	1.0	1.0	7603	0.29,0.30	6947	0.31,0.32
1.0	1.0	1.0	7632	0.29,0.30	7978	0.29,0.30
0.1	0.1	0.1	8346	0.29,0.30	7717	0.30,0.31
0.1	0.5	0.1	7896	0.29,0.31	7717	0.30,0.31
0.1	1.0	0.1	8072	0.29,0.31	7623	0.30,0.31
0.5	0.1	0.5	7719	0.29,0.31	7897	0.29,0.31
0.5	1.0	0.5	10084	0.28,0.28	9869	0.28,0.29
1.0	0.1	1.0	7719	0.29,0.31	7896	0.29,0.31
1.0	**0.5**	**1.0**	**6969**	**0.31,0.32**	**7410**	**0.30,0.31**
1.0	1.0	1.0	7632	0.29,0.30	7977	0.29,0.31

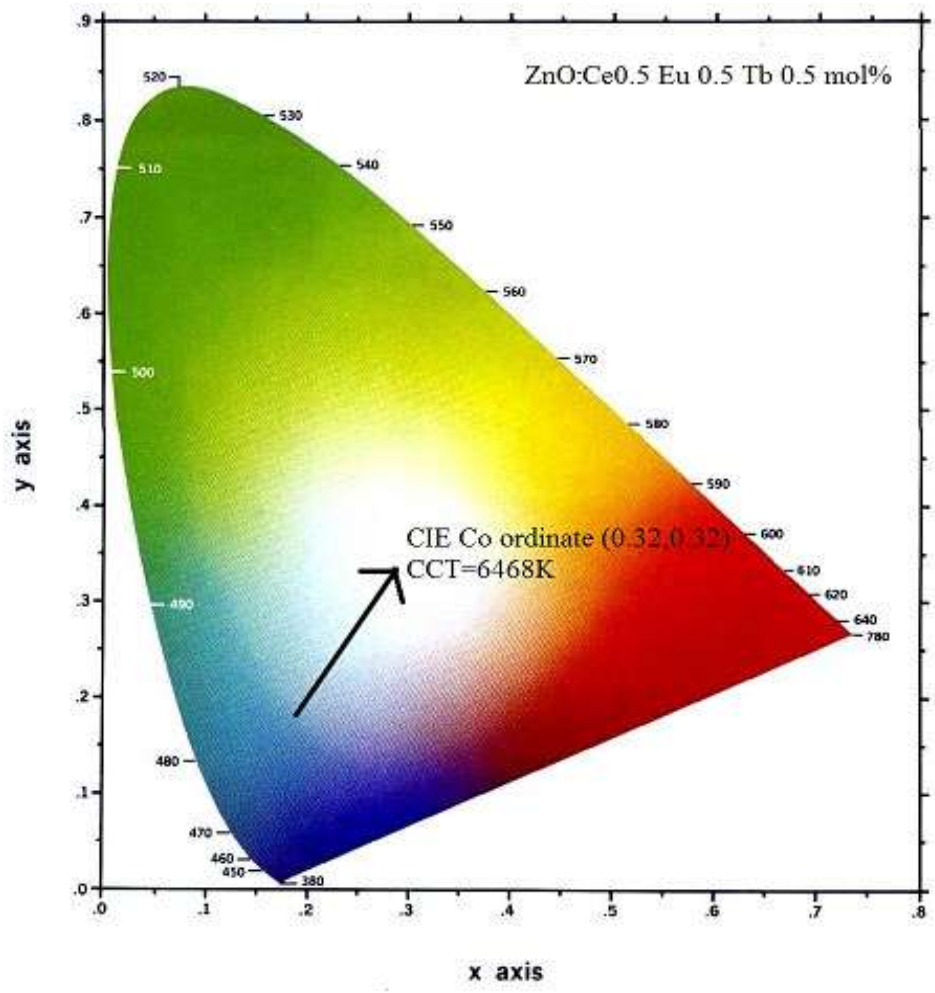

Fig 7.14: CIE color space diagram of ZnO co-doped with 0.5mol% Ce, Eu and Tb; the emission was excited with 280nm radiation

As seen in this picture (Fig. 7.14), the color coordinates lie well within the white portion of the diagram indicating the usefulness of this material in the realization of a white light source.

The next best material for the realization of the white light source is ZnO co-doped with 1.0mol% of both Ce and Tb and 0.5mol% of Eu. The chromaticity color coordinates for this emission are: x=0.31 and y=0.32 with CCT= 6969K. The corresponding CIE color space diagram is shown in Fig 7.15

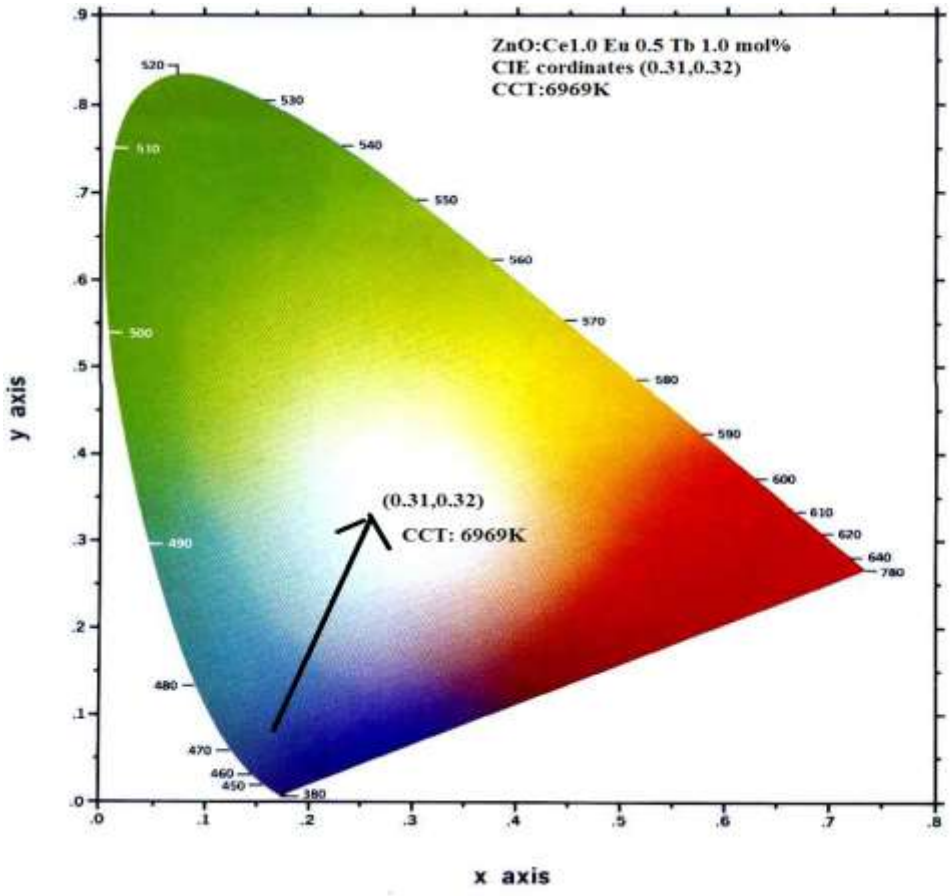

Fig 7.15: CIE color space diagram of ZnO co-doped with 1.0 mol% both Ce, Tb and 0.5mol% Eu ; the emission was excited with 280nm radiation

Chapter 8

Summary and Conclusions

8.1 Summary

The motivation for the study reported in this thesis, as stated in earlier chapters, was to investigate the potential of the nano powders of ZnO and TAG doped with rare earths for the development of efficient white light sources. ZnO was chosen because of its characteristic emission in visible emission which can be tailored by doping while TAG which, when doped with Ce, is a work-horse of present day LED industry. On the other hand, rare-earths were chosen for doping because of their unique emission properties in visible region. The materials investigated in detail were:

1. Singly doped Ce, Eu, Gd and Tb ZnO nano powders
2. Ce and Eu co-doped in TAG and ZnO
3. Ce, Eu and Tb co-doped in ZnO

The doping concentrations used in all the above material were 0.1, 0.5 and 1.0 mol%. Permutations of these doping concentrations were used for materials doped with more than one elements; nine nano powder samples were prepared for Ce and Eu co-doped in ZnO and TAG while eighteen samples were prepared for Ce, Eu and Tb doped ZnO.

ZnO based nano powders were prepared by co- precipitation method while TAG based samples were synthesized by sol gel technique.

The doping was confirmed with EDX while XRD was employed to investigate the crystal structure of all the prepared samples. The structural properties were further confirmed with FTIR and Raman spectroscopy. Nano structure of the powders was confirmed with SEM/TEM techniques. Band gap in ZnO was investigated with UV-VIS absorption spectroscopy while characteristic absorption in TAG was investigated by the same technique. Photoluminescence spectroscopy was used to investigate the emission from the samples while CIE 1931 color space diagrams were prepared to calculate the chromaticity coordinates of the emission in visible region to assess the suitability of the prepared samples for the realization of the white light sources.

8.2Conclusions

8.2.1 ZnO based systems

1. EDX spectra confirmed the incorporation of Ce, Eu, Gd and Tb in ZnO lattice
2. XRD spectra showed that doping levels in the concentration range of 0.1 to 1.0 mol% did not change the basic crystal structure of ZnO
3. XRD spectra did not show any independent phase of any doping element further confirming the incorporation of rare-earths in ZnO.
4. Splitting and shifting of XRD peaks on Tb doping showed the stress induced in ZnO lattice on doping.
5. The analysis of XRD data showed that the powders were composed of nano crystallites; the size of the crystallites was found to be dependent on nature of the doping element as well as its concentration.
6. SEM and TEM images showed that the particles in the prepared material were nano sized with spherical morphology.
7. From the PL spectra of rare earth doped, it was concluded that there was broadening of emission peak in visible region and intensity of peak enhanced on doping. The broadening of peak was due to the defects in crystal lattice which was responsible for the visible emission from rare earth doped ZnO. Concentration quenching was also observed at higher doping concentration in rare earth doped ZnO. In case of Gd : ZnO at 0.5 mol% of doping, CIE co-ordinates obtained were x=0.31 and y =0.32 and CCT is 6965 K. In case of Ce, Eu, Tb :ZnO at 0.5 mol% of each ,CIE coordinates obtained were x=0.32,y=0.32 having CCT equal to 6468 K .

8.2.2 TAG based systems

From the characterization of rare earth doped TAG material, the following conclusions have been drawn:

1. EDX spectra of singly and doubly rare earth (Ce, Eu) doped confirmed that Ce and Eu enter the TAG lattice.
2. SEM and TEM image confirmed that rare earth doped TAG had spherical morphology and some bigger particles were due to the agglomeration of particle at high temperature (1100^{o}C)

3. The study of rare earth doped TAG concluded that the crystal structure of TAG remained the same and similar inference was obtained from FTIR and Raman spectra.
4. PL spectra of rare earth doped TAG was the a broad peak in 400-700nm region which showed its usefulness to prepare white light sources. In case of Ce, Eu: TAG at 0.1 mol% of each , CIE coordinates obtained were x=0.28,y=0.30 having CCT equal to 8346 K .